

Department of Physics and Astronomy

University of Heidelberg

Master thesis

in Physics

submitted by

Antonia Clara Klein

born in Künzell

2018

**Versatile Platform for Cold Atom Physics with ^6Li
based on Holographic Potentials**

This Master thesis has been carried out by

Antonia Clara Klein

at the

Physikalisches Institut Heidelberg

under the supervision of

Herrn Prof. Dr. Selim Jochim

Versatile Platform for Cold Atom Physics with ${}^6\text{Li}$ based on Holographic Potentials

This thesis reports on the implementation of a major upgrade to an experiment of ultracold ${}^6\text{Li}$ atoms to create low entropy systems in tailor-made optical potentials. The core components of the add-on are a spatial light modulator (SLM), a high resolution objective and an electron-multiplying CCD camera. The former two provide the possibility to create almost arbitrary potentials projected onto a plane with submicron precision whereas the new imaging setup is intended to allow spin-resolved single-atom detection in free space in future. We present the investigation of the simplest system possible with the new setup—a single micro-trap. By recapturing the atoms in the magneto optical trap and collecting part of their fluorescence single atoms can be detected with a fidelity of more than 99%. We quantify that we can prepare a well-defined number of atoms with very high fidelity in the ground state of our tunable system. Finally, we show first results on coherent tunnelling dynamics in a double-well created by the SLM paving the way to the investigation of strongly correlated systems in lattices shaped at will such as Nagaoka ferromagnetism in a plaquette.

Vielseitige Plattform für Physik der kalten Gase mit ${}^6\text{Li}$ basierend auf holographischen Potentialen

Diese Arbeit beschreibt die Umsetzung einer weitreichenden Verbesserung eines Experiments mit ultrakalten ${}^6\text{Li}$ -Atomen, um Systeme niedriger Entropie in maßgeschneiderten optischen Potentialen zu erzeugen. Die Kernbestandteile der Erweiterung sind ein Spatial Light Modulator (SLM), ein hochauflösendes Objektiv und eine elektronenvervielfachende CCD-Kamera. Die beiden ersten ermöglichen es, beinahe beliebige Potentiale auf eine Ebene mit Submikrometer-Präzision zu projizieren, während der neue Aufbau zur Bildgebung in Zukunft dazu genutzt werden soll, einzelne Atome im freien Raum spinaufgelöst zu detektieren. Wir präsentieren die Untersuchung des einfachsten Systems, das wir mit dem neuen Aufbau realisieren können – einer einzelnen Mikrofalle. Durch das Wiedereinfangen der Atome in einer magneto-optischen Falle und die Messung eines Teils ihrer Fluoreszenz können einzelne Atome mit einer Zuverlässigkeit von über 99% detektiert werden. Wir quantifizieren, dass wir eine wohldefinierte Atomzahl mit einer hohen Zuverlässigkeit im Grundzustand unseres einstellbaren Systems präparieren können. Schließlich zeigen wir erste Ergebnisse kohärenter Tunneldynamik in einem Doppelpotf, der mit dem SLM erzeugt wurde. Damit ist der Weg geebnet, stark korrelierte Systeme in nach Belieben geformten Gittern zu untersuchen, wie etwa Nagaoka-Ferromagnetismus in einer Plakette.

Contents

1. Introduction	3
2. Conceptual Framework	5
2.1. Cooling and Trapping Atomic Gases	5
2.2. Tuning Interactions	7
2.3. Tuning the External Potential	10
2.3.1. Working Principle of an SLM	10
2.3.2. Fourier Optics	12
2.3.3. Spatial Light Modulation	16
3. Avenues and Vision	17
3.1. The Hubbard Model at Half Filling and Beyond	17
3.1.1. Introduction to the Hubbard Model	18
3.1.2. Nagaoka Magnetism	19
3.2. Majorana Bound States	20
3.2.1. Ettore Majorana's Discovery	21
3.2.2. Majorana Zero Modes in Condensed Matter Systems	22
3.2.3. Signatures of Majorana Fermions and how to Measure them	32
4. Realization of an Ultracold 2D Fermi Gas	35
4.1. Properties of ${}^6\text{Li}$	35
4.2. Experimental Sequence	36
4.3. Previous Work on 2D Fermi Gases	38
5. Experimental Extension	41
5.1. Creating Tailor-Made Potentials	41
5.2. Extensional Setup	44
5.2.1. Optical Setup of the SLM	44
5.2.2. Optical Setup of the Objective and for Imaging	48
5.3. Implementation	52
5.4. A High-Resolution Objective	55
5.5. Single Atom Detection	59

Contents

6. First Experimental Results	63
6.1. Loading the Microtrap and Preparing Single Atoms	63
6.2. Single Atom Detection with MOT Imaging	65
6.3. State Preparation	67
6.4. Testing Different Trap Geometries	71
6.5. Fermions in a Double-Well	73
7. Conclusion and Outlook	83
Appendices	87
A. Quantum Computation	89
A.1. Fusion Rules and Topological Charge Measurements	89
A.2. Unitary Operations and Qubits in the Fusion Space	90
B. Fourier Transforming with a Thin Lens	93
C. Technical Details of the LCOS Spatial Light Modulator by Hamamatsu	95
D. Alignment Protocol for the Objective	96
Bibliography	99

1. Introduction

Tunable systems can provide access to intriguing regimes that are hard to investigate with a system restricted to a set of fixed parameters. An example for the fertility of such systems was demonstrated recently in the field of novel condensed matter systems [Cao18]. The group of Pablo Jarillo-Herrero engineered a highly tunable system composed of two sheets of graphene stacked on top of each other with a variable twisting angle among the sheets. At an angle of 1.1° this graphene superlattice has a perfectly flat band and appears to be in a correlated insulating state at half filling. However, varying this angle slightly the material turned out to be superconductive in the presence of a magnetic field. This is a ground breaking discovery given the fact that monolayer graphene never exhibits superconductivity.

An important experimental question is, can we engineer versatile systems that allow to explore many-body phenomena in different scenarios? Especially the strongly correlated regime is difficult to tackle with theoretical approaches and simulations are restricted by limited computational resources. At a broad level, such systems should provide high tunability of parameters as well as the ability to measure key observables. Ultracold atoms have been found to be very promising in this regard as a multitude of parameters can be controlled and detection is steadily improving. Among those parameters are the interaction strength, the atomic species or mixture going along with fermionic or bosonic quantum statistics, the particle number, the density and the temperature.

Currently, most experiments are performed in traps of fixed geometry which are loaded from a bulk gas. In this thesis we choose another direction which is crucially different. With the implementation of a spatial light modulator (SLM) we take a step further in the control of the system. The SLM allows us to create almost arbitrary potential landscapes projected onto a two dimensional plane. For lattices single site control seems well within reach. Initializing lattices based on atom-by-atom assembly with optical tweezers has recently been demonstrated in Rydberg experiments in one, two and three dimensions [End16; Kim17; Bar18].

The approach we want to take in order to seize control over the quantum state is based on the deterministic preparation of single building blocks in the lowest energy level which can be adiabatically merged to a correlated many-body ground state. The smallest building block is the two-site Hubbard model at half filling

1. Introduction

in the ground state. Adapting the preparation schemes presented in [Ser11b] and [Mur15a] the smallest building block, the two-site Hubbard model at half filling, can be prepared with over 90% fidelity in the ground state. With this technique at hand we are in an optimal position to initialize lattices at very low entropy in future. The degree of control over the quantum state is much higher with this protocol than with the conventional scheme based on loading atoms from a cloud into a standing-wave lattice. Consequently, our quantum system is a promising candidate to study the phase diagram of the fermionic Hubbard model which is not yet well understood. In particular this brings us into a position where we can investigate phenomena that were never measured before like Nagaoka ferromagnetism. Going beyond the Hubbard model we might be in a position to come closer to the investigation of Majorana bound states in one-dimensional p -wave superconducting chains whose observation in cold atoms was so far out of reach.

For the proposed experiments the possibility to detect single atoms with spin and spatial resolution would be a valuable tool. Recent developments in the field of quantum gas microscopes show that they can be used to probe cold atom experiments on the level of a single lattice sites and that they are crucial to map out correlations of the system [Maz17; Bol16; Che16]. With the implementation of a high resolution objective and an EMCCD camera we aim to adapt a free space imaging technique introduced in [Ber18b].

This thesis is structured as follows. In chapter 2 we start with an introduction of ultracold atoms as highly tunable systems. It is followed by a discussion of the Hubbard model and an excursion about Majorana bound states, which are both interesting theoretical concepts for our experiment (chapter 3). In chapter 4 we introduce the experimental setup that served as a basis for the major extension implemented during this thesis. The upgraded experiment is then presented in chapter 5. First experimental results are shown in chapter 6.

2. Conceptual Framework

Tunability combined with the ongoing development of state preparation and detection schemes steadily opens new doors for researchers in the field of ultracold atoms. A decisive step for the field to sprout was the development of advanced cooling techniques that allow to enter the regime where quantum statistics matter. Among them is the optical dipole trap which plays a fundamental role in the course of this thesis as we use this trapping scheme to tailor potential landscapes with the newly implemented spatial light modulator (SLM).

In this chapter we want to present the cornerstones of tunability in our system. Starting with the introduction to cooling and trapping schemes applied in our experiment (tuning the temperature), we continue with a small excursion on scattering theory (tuning interactions) and finally explain how to shape a beam by phase modulation (tuning the external potential).

2.1. Cooling and Trapping Atomic Gases

The developments towards ultracold atom experiments was pushed with the invention of cooling mechanisms based on radiation force. In the 1980s the first magneto-optical trap (MOT) with which atoms can be cooled down to several hundred micro Kelvin was realized [Raa87]. In a common MOT setup pairs of counter-propagating near-resonant beams are installed along each spatial dimensions. Additionally, a magnetic quadrupole field is provided by a pair of coils in anti-Helmholtz configuration.

To understand the working principle of the MOT the optical contribution and the magnetic contribution can be considered separately. The former contribution is based on the Doppler shift. A MOT works with red-detuned beams that are close to resonance. Consequently, the probability that an atom absorbs light from a beam that is propagating in the direction opposite to its own movement is enhanced due to the Doppler effect whereas the probability to absorb a co-propagating photon is reduced. If the atom goes back to the ground state via spontaneous emission no momentum is transferred on average due to the randomness of the transmission direction. As a result the atom is effectively decelerated. To additionally confine the atoms we need the magnetic quadrupole field. In its

2. Conceptual Framework

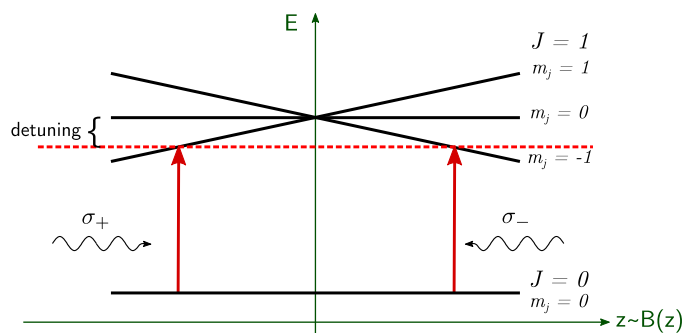


Figure 2.1.: Confining atoms with a MOT. Atoms are confined to the centre of the trap by exploiting the magnetic field dependence of the Zeeman levels. Due to a small detuning of the laser beam atoms located right (left) from the trap centre are more likely to get excited by the σ_- (σ_+) beam and therefore effectively pushed to the trap centre.

presence the degeneracy of the Zeeman levels is lifted whereby the energy splitting depends on the magnetic field and consequently on the position as depicted in figure 2.1. Choosing σ_- - (σ_+ -)polarization for the red-detuned beam coming from right (left) means that for an atom located right (left) from the centre a σ_- - (σ_+ -)transition is much closer to resonance and therefore more probable. As a result the atoms are effectively pushed to the centre of the trap. Cooling with the MOT is in general limited by the Doppler temperature which is in the regime of hundreds of micro Kelvin.

To overcome the limitation set by the natural linewidth of the atoms and thus further increase the phase-space density one can load the atoms from the MOT into an optical dipole trap (ODT). It is based on the induction of a dipole moment $\mathbf{p}(\mathbf{r}, t)$ in the neutral atom. ODTs can be discussed in terms of a dressed atom picture [Dal85; Dal89] but already a semi-classical oscillator model [Gri00], chosen here, provides insight into the trapping mechanism. Let us call the resonance frequency ω_0 and the frequency of the external field ω . The light-induced potential can be described as

$$U_{\text{dip}}(\mathbf{r}) \sim - \left(\frac{\Gamma}{\omega_0 - \omega} + \frac{\Gamma}{\omega_0 + \omega} \right) I(\mathbf{r}). \quad (2.1)$$

Here Γ is the natural linewidth of the transition. In the experiment the external field is provided by laser of wavelength $\lambda = 1064 \text{ nm}$, which is far red-detuned from the resonance at $\lambda = 671 \text{ nm}$ for ${}^6\text{Li}$. For these parameters the assumption $|\Delta| \ll \omega_0$ with $\Delta \equiv \omega - \omega_0$ is not very good but it is still educative to consider

this limiting case. The dipole potential reduces then to

$$U_{\text{dip}}(\mathbf{r}) \sim \frac{\Gamma}{\Delta} I(\mathbf{r}). \quad (2.2)$$

One can see that the interaction is attractive (repulsive) for negative (positive) detuning. For the far red-detuned light which is chosen in our experiment the atoms thus minimize their energy at intensity maxima. In the limit $|\Delta| \ll \omega_0$ the scattering rate of photon absorption and re-emission is given by

$$\Gamma_{\text{scat}} \sim \left(\frac{\Gamma}{\Delta} \right)^2 I(\mathbf{r}). \quad (2.3)$$

In an optical dipole trap dissipative processes are not desired but deep trapping potentials are favourable. Consequently, by comparing equation (2.2) and equation (2.3) one obtains that it is best to perform an ODT at high powers and large detuning.

Quantum degeneracy can finally be reached by applying a forced evaporation technique in the ODT. Reducing the trap depth allows the hottest atoms leave the trap. Working in the interactive regime the system can constantly rethermalize via scattering during the process since high scattering rates lead to fast thermalization rates.

2.2. Tuning Interactions

The tunability of ultracold systems is also reflected in the possibility to vary interaction strengths. We only want to give a very short overview of the underlying physics here. For a detailed discussion of scattering theory see for example [Wal14].

In general, scattering processes of two particles are described best in their centre-of-mass frame as the interaction potential only depends on the relative distance \mathbf{r} of the scatterers. To solve the Schrödinger equation in the far-field of an elastic scattering process the usual ansatz for the wave function is to consider a superposition of an incident plane wave $\psi_0(\mathbf{r})$ and an outgoing wave $\psi_s(\mathbf{r})$,

$$\psi(\mathbf{r}) = \psi_0(\mathbf{r}) + \psi_s(\mathbf{r}), \quad (2.4)$$

where the outgoing wave needs to describe a free process for $r \rightarrow \infty$ and is

2. Conceptual Framework

therefore given by a spherical wave

$$\psi_s(\mathbf{r}) = f(\theta) \frac{\exp ikr}{r}, \quad (2.5)$$

with amplitude $f(\theta)$, also called scattering amplitude, in this limit. The problem can be solved by an expansion into partial waves. The presence of the scattering potential manifests itself then in a phase shift δ_l compared to the free case where l is the index of the expansion. The contribution to the l th term of the expansion of the scattering amplitude is given by

$$f_l = \frac{1}{k \cot \delta_l - ik}. \quad (2.6)$$

In a gas of ultracold atoms the energies involved in the scattering process are low and only pairwise interaction needs to be taken into account. The scattering potential is of Lennard-Jones type which is strongly repulsive at short distance and has a long-range attractive Van der Waals tail. For this potential one finds for the lowest angular momenta l

$$f_0 \underset{k \rightarrow 0}{\approx} -a \quad \text{and} \quad f_1 \underset{k \rightarrow 0}{\approx} -a_1^3 \frac{1}{3} k^2, \quad (2.7)$$

where a (a_1) denotes the so called s -wave (p -wave) scattering length. In general, only the s -wave term contributes because for $l > 0$ an additional barrier, called centrifugal barrier, is present in the interaction potential. Therefore, contributions of higher angular momenta are only relevant for initial energies of the scatterers that exceed the centrifugal barrier, which is for the ultracold gas of ${}^6\text{Li}$ we use in experiments usually not given. The scattering length, introduced in equation (2.7), is a measure for the interaction strength and can be considered as an effective hard-sphere diameter of the potential. For small momenta it determines the cross section of the scattering process given by

$$\lim_{k \rightarrow 0} \sigma = 4\pi a^2, \quad (2.8)$$

which determines the ratio of the number of processes per time interval and the current density of the particles.

So far all considerations were based on a single scattering potential between the atoms. However, for real alkali atoms it is necessary to take the internal states of the scatterers into account (see e.g. [Ket08]). For fermions, the s -wave scattering channels for spin singlet and triplet configuration are different in energy

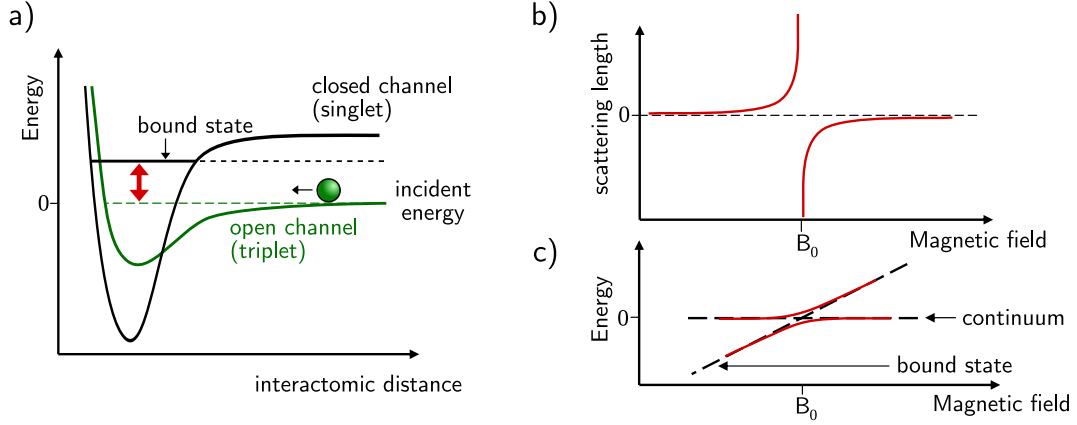


Figure 2.2.: Scattering of distinguishable fermions. a) The scattering length can be resonantly enhanced by coupling an energetically accessible scattering channel (open channel) to a bound state of an inaccessible closed channel. b) The scattering length can be controlled by tuning the magnetic offset field. c) Due to the coupling of singlet and triplet state an avoided crossing the molecular states (attractive branch) and free scattering states (repulsive branch) shows up. b) and c) adapted from [Wen08].

(figure 2.2 a)). The triplet channel is energetically accessible and therefore called “open”. In this channel the atoms can scatter in a continuum of states. In contrast scattering in the bound levels of the singlet potential is forbidden by energy conservation. However, due to the hyperfine interaction there is some coupling between triplet and singlet potential. If the energy with which the atoms enter the triplet channel is close to a bound state of the singlet the interaction is resonantly enhanced due to the coupling of open and closed channel. By this means large positive or negative scattering length can be obtained close to resonance depending on the sign of the energy difference of open and closed channel. As the two channels differ in magnetic moment by $\Delta\mu$ one can tune the energy difference by applying a magnetic offset field B according to $\Delta E = \Delta\mu B$. The dependence of the scattering length on the magnetic field is depicted in figure 2.2 b).

At negative energies and positive s -wave scattering length a two-particle bound state exists for distinguishable fermions (figure 2.2 c)) with binding energy

$$E_B = \frac{\hbar^2}{2ma^2}. \quad (2.9)$$

If the binding energy is larger than any other energy scale of the system and temperatures are low the paired fermions form a molecule that is to be described by Bose statistics.

2. Conceptual Framework

2.3. Tuning the External Potential

In a MOT atoms are always trapped in a cloud. Differently, in a dipole trap various trap geometries are possible. The simplest realization would be to use a Gaussian beam which has an intensity distribution $I(\mathbf{r}, z) \sim 1/w^2(z) \exp(-2\mathbf{r}^2/w^2(z))$ resulting in a cigar-shaped trap. Here $w(z)$ denotes the waist of the beam depending on z . Also the exploitation of interference effects can lead to useful trap geometries such as square, honeycomb or kagome lattices or traps consisting of a stack of light sheets often referred to as “pancake traps”. Trapping atoms in a single one of these light sheets or with an tightly focused Gaussian beam (optical tweezer) can lower the effective dimensionality of the system to two or one dimension respectively. Both regimes are accessible with our current setup.

In this section we want to concentrate on the possibility to create tailored dipole potentials by shaping light with spatial light modulators (SLMs). Originally used for computer-controlled projectors, today SLMs enjoy a large popularity in science. For instance, they are used for aberration correction in optical microscopy in biology or to create optical tweezers that can hold atoms or nanoparticles in cold atom physics and biophysics, respectively. SLMs are either based on amplitude modulation or phase modulation of the incident beam. The former technique is usually used for projectors whereas the latter one is favoured for applications in science [Zha14] and also used in our experiment.

This section covers how an SLM works technically, basics on Fourier optics and how to combine these concepts to shape a beam.

2.3.1. Working Principle of an SLM

The key component of spatial light modulators are liquid crystals which have already been utilized in display applications such as those of calculators and digital clocks for a few decades. Nowadays, they are dominating the industry of flat screens.

The cigar-shaped liquid crystal molecules are in a fluid state of matter but as the name already indicates they possess properties of a solid as well. Although they exhibit different phases, we will be only concerned with the nematic phase (figure 2.3 a)). In this phase the anisotropic molecules lack positional order completely, which is typical for a liquid, but at the same time they show crystal-like orientational order. An important feature of a liquid crystal molecule is its birefringent nature, meaning that its refractive indices for the long axis n_e (extraordinary axis) and for the short axis n_o (ordinary axis) differ. Usually n_e is bigger than n_o (figure 2.3 a), inset). When being subject to force, the orientation of the molecules changes. Therefore, a common method to prepare the liquid crystals is to confine them within two polymeric alignment layers and subsequently rub

2.3. Tuning the External Potential

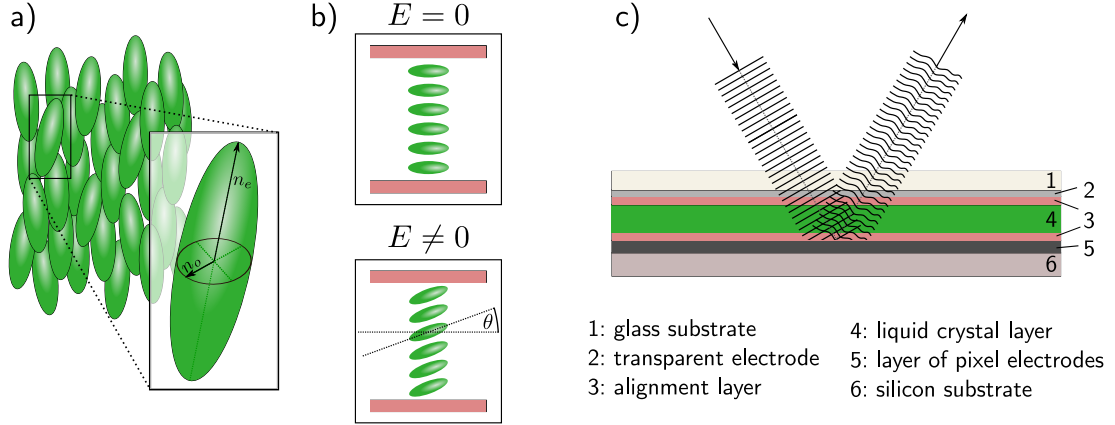


Figure 2.3.: Phase modulation with liquid crystals. a) In the nematic phase they tend to be parallel but lack positional order. LCs possess different refractive indices for the two axes (inset). b) The molecules can be rubbed into parallel orientation with two alignment layers (upper panel). In the presence of an electro-magnetic field they tilt towards its direction (lower panel). c) Spatially dependent phase modulation can be realized with an LCOS-SLM.

them mechanically into the desired direction. Parallel-aligned nematic (PAN) liquid crystals can be used for phase modulation¹ (figure 2.3 b), upper panel). Here, the molecules are originally oriented parallel to each other and the alignment layers. However, their angle can be controlled either by electro-optical means with incoherent light or by applying an electro-magnetic field perpendicular to the molecules. We are interested in the latter case. The presence of an electro-magnetic field induces a dipole moment in the molecules and thus they tend to line up with the external field (figure 2.3 b), lower panel). The angle θ of their tilt depends on the applied voltage. As a result, the refractive index $n(\theta)$ is changed for linearly polarized light with polarization direction in parallel to the molecule alignment. It is modified according to [Sal91]

$$\frac{1}{n^2(\theta)} = \frac{\cos^2 \theta}{n_e^2} + \frac{\sin^2 \theta}{n_o^2}. \quad (2.10)$$

The refractive index perpendicular to the alignment direction n_o is unaltered by the tilt². As a result for an incident beam of wavelength λ with polarization along

¹If the rubbing directions of the two alignment layers are perpendicular to each other the nematic molecules end up in a twisted configuration. Combining this configuration with polarization filters makes amplitude modulation of a beam possible.

²As a side remark, it is mentioned that for a wave with linear polarization with an angle

2. Conceptual Framework

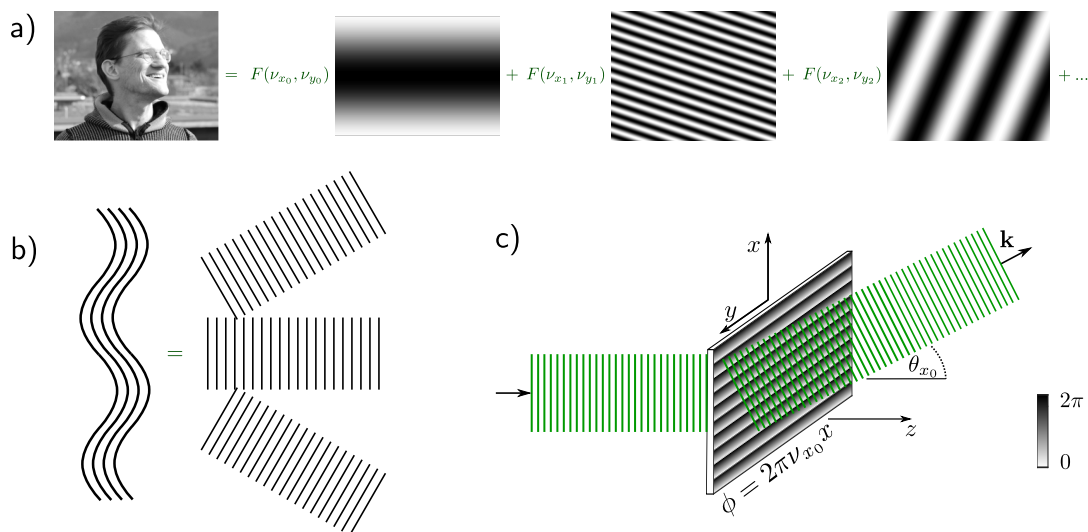


Figure 2.4.: a) A 2D picture can be decomposed into a sum of harmonic functions each weighted with a factor $F(\nu_{x_i}, \nu_{y_i})$. b) Similarly any wave function can be built out of plane waves. c) If a plane wave passes an optical element that alters its phase by $\phi = 2\pi\nu_{x_0}x$, its direction of propagation changes. This could be realized by an SLM.

the zero-field of the nematics its phase changes by $\Phi = 2\pi n(\theta)d/\lambda$ when passing a layer of liquid crystals of thickness d . If the external electro-magnetic field can be controlled position-dependently, for instance by using an array of electrodes, the phase is spatially dependent as well and thus such a device can shape the wavefront of a beam. This is the operating principle of an SLM. A discussion of the effect of phase modulation of coherent light follows in the next paragraph.

Figure 2.3 c) shows a schematic picture of a spatial light modulator based on liquid crystals on silicon (LCOS) technology. A thin layer of liquid crystals is sandwiched between two alignment layers. The adjacent layers at the front are a transparent electrode and a glass substrate. On the other side the alignment layer is next to a layer of pixel electrodes which in turn is fixed on top of a silicon substrate.

2.3.2. Fourier Optics

This section is based on the book of Saleh and Teich [Sal91]. The widely used concept to decompose a time dependent function $f(t)$ into a sum or integral

$0 < \alpha < \pi$ the described setting acts as a wave retarder, i.e. the polarization of the light is changed.

2.3. Tuning the External Potential

of harmonics with complex amplitudes $F(\nu)$ —called Fourier transform—is also applicable to functions that depend on spatial coordinates x and y . This yields the expansion

$$f(x, y) = \int_{-\infty}^{\infty} \int_{-\infty}^{\infty} d\nu_x d\nu_y F(\nu_x, \nu_y) e^{-i2\pi(\nu_x x + \nu_y y)}. \quad (2.11)$$

In analogue to the temporal frequencies, spatial frequencies are denoted by ν_x and ν_y and express cycles per unit length. As an example, one can illustrate the Fourier decomposition with a picture that is split up in a sum of harmonics (figure 2.4 a)). Each term is weighted with a factor $F(\nu_{x_i}, \nu_{y_i})$. These factors represent the Fourier transform.

One can connect this idea to wave optics. Here, we are only interested in the position-dependent part $U(\mathbf{r})$ of the wave function $\mathcal{U}(\mathbf{r}, t) = U(\mathbf{r}) \exp(i2\pi\nu t)$. For a plane wave, given by $U(\mathbf{r}) = A \exp(-i(k_x x + k_y y + k_z z))$, the wavelength λ is connected to the wave vector $\mathbf{k} = (k_x, k_y, k_z) \in \mathbb{R}^3$ via $2\pi/\lambda = \sqrt{k_x^2 + k_y^2 + k_z^2}$; A is a complex constant. Plane waves can be used as the building blocks of a wave of arbitrary complexity (figure 2.4 b)). Such a wave is, in general, a three-dimensional object and would thus require a summation or integration over all dimensions to Fourier transform it. However, monochromatic waves are constituted out of a single frequency, which means $|\mathbf{k}|$ is constant. With this at hand and using $\nu_x = k_x/2\pi$ and $\nu_y = k_y/2\pi$, the z -component of the wave vector depends only on the transverse spatial frequencies as $k_z(\nu_x, \nu_y) = \pm\sqrt{\mathbf{k}^2 - (2\pi\nu_x)^2 - (2\pi\nu_y)^2}$. Therefore, a monochromatic wave can be expressed in terms of a two-dimensional Fourier series

$$U(x, y, z) = \int_{-\infty}^{\infty} \int_{-\infty}^{\infty} d\nu_x d\nu_y F(\nu_x, \nu_y) e^{-i2\pi(\nu_x x + \nu_y y)} e^{-ik_z(\nu_x, \nu_y)z}. \quad (2.12)$$

Let us now use this framework to investigate how a spatially dependent phase shift can effect a plane wave. For this purpose we consider a scenario where a plane wave travels along the z -direction and passes through a special thin optical element at $z = 0$. This alters its wave function by a linear position-dependent phase factor $\exp(-i2\pi\nu_{x_0}x)$ (figure 2.4 c)). Behind the element for $z > 0$ the wave function therefore reads $U(x, y, z) = F(0, 0) \exp(-i2\pi\nu_{x_0}x) \exp(-ik_z z)$ with $F(0, 0)$ being a complex constant³. The angle enclosed by the \mathbf{k} -vector of the wave and the

³It should be noted that an approximation is used here. In an exact consideration it is not possible to express the effect of the optical element as a phase factor only depending on x and y because $|\mathbf{k}|$ must be conserved.

2. Conceptual Framework

z -axis is then given by $\theta_{x_0} = \arcsin(k_{x_0}/\mathbf{k}) = \arcsin(\lambda\nu_{x_0})$. In a more general setting with an initial plane wave

$$U(x, y, z) = F(\nu_{x_1}, \nu_{y_1}) \exp(-i2\pi(\nu_{x_1}x + \nu_{y_1}y)) \exp(-ik_z z) \quad (2.13)$$

the thin optical element shifts the frequencies for $z > 0$ as

$$U(x, y, z) = F(\nu_{x_1}, \nu_{y_1}) e^{-i2\pi((\nu_{x_1}+\nu_{x_0})x+(\nu_{y_1}+\nu_{y_0})y)} e^{-ik_z z} \quad (2.14)$$

$$= F(\nu_{x_1}, \nu_{y_1}) e^{-i2\pi(\tilde{\nu}_x x + \tilde{\nu}_y y)} e^{-ik_z z} \quad (2.15)$$

with $\nu_{x_1} + \nu_{x_0} \equiv \tilde{\nu}_x$ and $\nu_{y_1} + \nu_{y_0} \equiv \tilde{\nu}_y$. Thus $F(\nu_{x_1}, \nu_{y_1})$ is now the complex amplitude of a different harmonic function than before. An SLM can provide the features of the optical element considered above if one applies a linear phase pattern to it. Such a phase pattern modulo 2π is depicted in figure 2.4 c. This simple example already demonstrates the working principle of the SLM. However, the SLM can modulate the phase of the incoming wave in a far more general way giving rise to an arbitrary phase shift that also depends on the spatial coordinates as will be discussed in 2.3.3.

Going back to equation (2.12), one sees that a wave gathers a phase factor $\exp(-ik_z(\nu_x, \nu_y)z)$ for each ν_x, ν_y when it propagates through free space along z . This frequency dependent phase factor is called the transfer function of free space $H_d(\nu_x, \nu_y)$; the index d refers to the distance over which the wave evolves. If one considers a wave described by $U(x, y, z_1) \equiv f(x, y)$ at a plane at $z = z_1$ that travels over a distance d to a plane at $z = z_2$ then the wave function at the latter plane reads

$$U(x, y, z_2) \equiv g(x, y) = \int_{-\infty}^{\infty} \int_{-\infty}^{\infty} d\nu_x d\nu_y H_d(\nu_x, \nu_y) F(\nu_x, \nu_y) e^{-i2\pi(\nu_x x + \nu_y y)}. \quad (2.16)$$

Mathematically, this is a convolution given by a point-wise multiplication $G(\nu_x, \nu_y) = H_d(\nu_x, \nu_y) F(\nu_x, \nu_y)$ in Fourier space. However, in real space it is expressed as

$$g(x, y) = \int_{-\infty}^{\infty} \int_{-\infty}^{\infty} dx' dy' f(x', y') h_d(x - x', y - y'). \quad (2.17)$$

Here $h_d(x, y)$ is the Fourier transform of the transfer function called impulse-response function. The concept of convolution is also useful to describe other scenarios, for example if a wave passes an aperture.

Looking at an imaging setup, the question might arise how a lens modifies a wave. On a qualitative level, one can understand that a spherical thin lens maps an ingoing wave described as $U(x, y, z_1) \equiv f(x, y)$ at a plane $z = z_1$ to its Fourier transform $F(\nu_x, \nu_y)$ in the focal plane. To this end, consider a single plane wave whose wave vector encloses a small angle $\theta_{x_0} = \lambda\nu_{x_0}$, $\theta_{y_0} = \lambda\nu_{y_0}$ with the z -axis. The lens converts the plane wave into a paraboloidal wave which is focused down into a point of coordinates $(\theta_{x_0}f, \theta_{y_0}f)$ in the focal plane at distance f from the lens (figure 2.5 a)). The position of the focus can thus be connected to its complex amplitude $F(\nu_{x_0}, \nu_{y_0})$. According to equation (2.12) an arbitrary wave $f(x, y)$ can always be decomposed into a set of plane waves. Each of them is focused down into a distinct point and thus the amplitude in the focal plane represents the Fourier transform of $f(x, y)$. A more rigorous explanation of the transformation properties of a lens can be found in appendix C. One finds that a wave described by $f(x, y)$ in the plane at distance $-f$ relative to the lens is related to the wave $g(x, y)$ at the focal plane by

$$g(x, y) = \frac{i}{\lambda f} F\left(\frac{x}{\lambda f}, \frac{y}{\lambda f}\right) e^{-i4\pi f/\lambda} \quad (2.18)$$

where the spatial frequencies are identified as $\nu_x = x/(\lambda f)$ and $\nu_y = y/(\lambda f)$. Consequently, the intensity distribution at the output plane is given by $I(x, y) = |g(x, y)|^2 = 1/(\lambda f)^2 |F(x/\lambda f, y/\lambda f)|^2$.

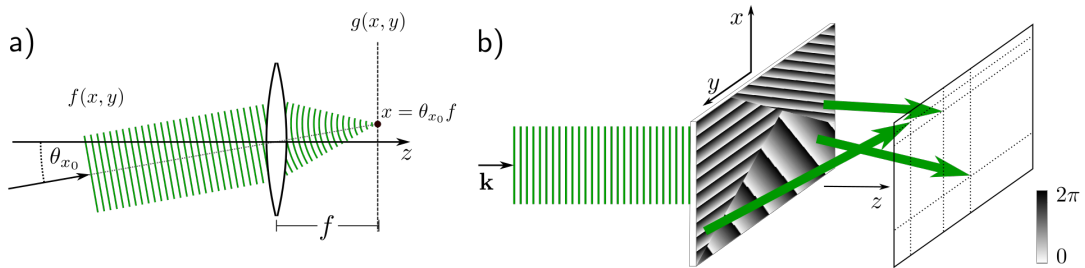


Figure 2.5.: Influence of optical elements on a plane wave. a) A lens focuses a plane wave down to a point $(\theta_{x_0}f, \theta_{y_0}f)$ in the focal plane. Figure b) visualizes how a phase pattern $\phi_{SLM}(x, y)$ applied to the SLM can be decomposed into regions of linear phase gradients by Taylor expanding $\phi_{SLM}(x, y)$ around different x_0, y_0 .

2. Conceptual Framework

2.3.3. Spatial Light Modulation

In section 2.3.2 we discussed a linear gradient, i.e. $\phi_{\text{SLM}}(x, y) = -2\pi(\nu_{x_0}x + \nu_{y_0}y)$ as a simple phase pattern that could be applied to the SLM. It changes the angle enclosed by the z -axis and the \mathbf{k} -vector of an incoming plane wave by shifting its Fourier transform according to equation (2.14). One can imagine that it is also possible to apply more complex, non-linear patterns to the SLM. The wave front is in this case not bent homogeneously but it is altered depending on the position (x_0, y_0) on the SLM. The linear terms of a Taylor expansion of such a phase pattern

$$\phi_{\text{SLM}}(x, y) = \phi(x_0, y_0) + (x - x_0)\partial\phi/\partial x|_{x_0, y_0} + (y - y_0)\partial\phi/\partial y|_{x_0, y_0} + \mathcal{O}(x^2, y^2) \quad (2.19)$$

can be identified with the spatial frequencies $\nu_{i_0} = \partial\phi/\partial i|_{i_0}$ for $i = x, y$ that determine the angle of diffraction. Figure 2.5 b) conveys how the spacial dependence of the SLM phase works conceptually.

For an incoming wave $U(x, y, z)$ any phase pattern $\phi_{\text{SLM}}(x, y)$ applied to the SLM changes the wave function. Denoting the position directly before the SLM with z_{in} and directly after the SLM with z_{out} one obtains

$$U(x, y, z_{\text{out}}) = U(x, y, z_{\text{in}}) e^{-i\phi_{\text{SLM}}(x, y)}. \quad (2.20)$$

Besides the SLM itself the subsequent lens-setup is crucial. In our experiment it projects the wave function at the SLM-plane onto its Fourier plane, where the atoms are prepared. The wave function in the atoms' plane z_{target} reads then

$$U(x, y, z_{\text{target}}) = \frac{i}{\lambda f} \mathcal{F} [U(\cdot, \cdot, z_{\text{out}})] \left(\frac{x}{\lambda f}, \frac{y}{\lambda f} \right) e^{-i4\pi f/\lambda} \quad (2.21)$$

$$= \frac{i}{\lambda f} \mathcal{F} [U(\cdot, \cdot, z_{\text{in}}) e^{-i\phi_{\text{SLM}}}] \left(\frac{x}{\lambda f}, \frac{y}{\lambda f} \right) e^{-i4\pi f/\lambda}. \quad (2.22)$$

As a result, the intensity distribution in the atoms' plane is given by

$$I_{\text{target}}(x, y) = 1/(\lambda f)^2 |\mathcal{F} [U(\cdot, \cdot, z_{\text{in}}) e^{-i\phi_{\text{SLM}}}] \left(\frac{x}{\lambda f}, \frac{y}{\lambda f} \right)|^2. \quad (2.23)$$

We can conclude that an SLM is a valuable tool to engineer dipole potential landscapes. Assuming the required phase pattern is known it is possible to create almost arbitrary intensity distributions with the SLM for a given incoming wave.

3. Avenues and Vision

In this chapter we want to present two possible roads that are interesting for our experiment. We start with an introduction to the Hubbard model. The Hubbard model describes all kinds of lattice geometries that we can engineer with the SLM. So far, we already realized the two-site Hubbard model with the upgraded experiment. In the near future we want to extend the experiments to four wells and investigate Nagaoka ferromagnetism. In the second part of this chapter we give an introduction to Majorana bound states. They are a promising candidate for an implementation of quantum computation. However, to engineer these systems is highly non-trivial due to the required p -wave superconductivity.

3.1. The Hubbard Model at Half Filling and Beyond

Originally proposed in the 1960s as a simplified model to describe motion of conduction electrons interacting via Coulomb repulsion in a lattice of ions—or in other words a metal—the Hubbard model has enjoyed a great popularity ever since [Hub63; Kan63; Gut63]. Its simple Hamiltonian that consists of term describing nearest-neighbour hopping and an on-site interaction gives rise to a very rich phase diagram and is a promising candidate to provide insight into high temperature superconductivity. With increasing experimental possibilities the interest in realizing the Hubbard model was growing over the last decade in the field of cold atoms. Although the Hubbard Hamiltonian has a simple form it is a mathematically hard problem to solve it for non-trivial parameters. As a consequence the approach to simulate the Hubbard model with cold atoms attracts a lot of attention. Realizations with both, fermions and bosons, are possible where their description in terms of the Hubbard model is governed by their different quantum statistics. In 2002 a milestone in the investigation of the Bose Hubbard model was marked when the transition from superfluid to Mott insulator was observed [Gre02] which was recently followed by ground breaking results of a fermionic antiferromagnet [Maz17].

3.1.1. Introduction to the Hubbard Model

There exist many versions of the Hubbard model. In the following we want to focus on the most popular one which is describing particles in the lowest band of a lattice. Only nearest-neighbour tunnelling of amplitude t is taken into account which is a good approximation if the on-site wave functions are localized to a large extent. Additionally an on-site interaction U is considered (figure 3.1). Although the Coulomb interaction is long-range neglecting interactions among electrons from different sites is a valid approximation for some metals due to screening effects. The Hamiltonian of the Fermi Hubbard model therefore reads

$$\hat{H} = -t \sum_{\langle i,j \rangle} \sum_{\sigma} \hat{c}_{i,\sigma}^{\dagger} \hat{c}_{j,\sigma} + U \sum_i \hat{c}_{i,\downarrow}^{\dagger} \hat{c}_{i,\downarrow} \hat{c}_{i,\uparrow}^{\dagger} \hat{c}_{i,\uparrow} \quad (3.1)$$

where the notation $\langle i,j \rangle$ indicates that only hopping to adjacent sites is allowed, \hat{c} is the electron annihilation operator and σ denotes the spin orientation. In ultracold quantum gases a pseudo-spin system can be realized by working with two different hyperfine states of the atom.

Although the Fermi-Hubbard model gives rise to several distinct phases, which are not yet completely understood, some intuition can be gained by the consideration of the limiting cases $U/t \ll 1$ and $U/t \gg 1$ given repulsive interactions ($U > 0$). For $U/t \ll 1$ and a filling factor smaller than one the system behaves like a metal. The filling factor is given by the number of atoms divided by two times the number of lattice sites. In the limit of no tunnelling $U/t \rightarrow \infty$ the sites decouple, density fluctuations are suppressed and a Mott gap $\Delta = U$ emerges in the excitation spectrum at half filling. Different spin configurations are degenerate in this regime. However, for $U/t \gg 1$ but finite the spin configuration matters for the energy of the system. At half filling, and small temperatures a strongly correlated antiferromagnetic arrangement of the spins is favourable be-

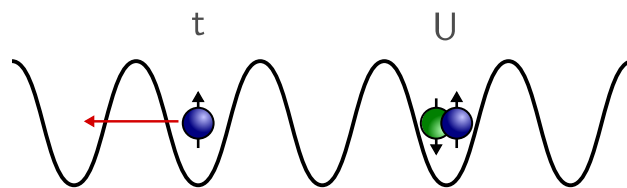


Figure 3.1.: Fermions in a periodic potential described by the Hubbard model. The two contributions to the model are tunnelling of the particles, which is connected to the kinetic energy of the system, and an on-site interaction. Due to the Pauli principle a single site can at most be doubly occupied.

3.1. The Hubbard Model at Half Filling and Beyond

cause the system aims to minimize its energy by virtual tunnelling processes. Due to the Pauli principle only super-exchange process of fermions with opposite spin are possible. During this second order process both fermions temporarily occupy the same site. The energy scale of the antiferromagnetic exchange is given by $J \equiv 4t^2/U$. In this limit the Hubbard Hamiltonian is equivalent to the Heisenberg spin Hamiltonian $\hat{H} = J \sum_{i,j} \mathbf{S}_i \mathbf{S}_j$ with \mathbf{S} being the spin operator. This Hamiltonian describes spin systems of immobile spins.

Cold atom experiments provide a promising tool for further investigations of the Hubbard model in regimes that are not accessible by numerical methods. For example they could be used to map out the ground state of the doped Fermi-Hubbard model. State of the art imaging techniques allow to measure strong correlations of the systems [Hal15; Edg15; Par16; Maz17; Ber18a]. Commonly, lattices in cold atoms realized by interference of two Gaussian beams. In our experiment we want to take a different approach by projecting 2D lattices onto a plane with a spatial light modulator (SLM). By making use of the abilities of the SLM we plan to obtain a high degree of control over the single lattice sites. The relation of on-site interaction and tunnelling U/t can be tuned with Feshbach resonances or the laser power. In our experiment we can in principle also work in the molecular regime of bound atoms instead of free fermions which allows us to investigate the Bose-Hubbard model as well.

3.1.2. Nagaoka Magnetism

Having learned that the ground state of the Fermi-Hubbard is antiferromagnetic at half filling and $U/t \gg 1$ one question that might arise is how the system behaves in the case of hole doping. In this scenario itinerant fermions—or, taking another point of view, holes—might reduce the kinetic energy of the system by moving in the lattice and delocalizing. However, for example, the movement of a single hole destroys antiferromagnetic order. Consequently, the energy gain by tunnelling is competing with the cost in energy due to incorrect bonds, i.e. bonds that are not favourable in terms of superexchange energy. In 1966 Yosuke Nagaoka presented rigorous proof of a ferromagnetic ground state in the Hubbard model at infinite on-site repulsion for one fermion less than half filling [Nag66]. It is an open question if other filling fractions might support ferromagnetism as well but exemplary calculations seem to suggest that this is not the case [Tak82]. The original Nagaoka theorem states that for one hole away from half filling, $U = \infty$, and $t < 0$ and given certain connectivity conditions the ground state is ferromagnetic [Nag66]. For bipartite lattices the last requirement has no impact because for those lattices there exists a mapping between $t > 0$ and $t < 0$. Taking

3. Avenues and Vision

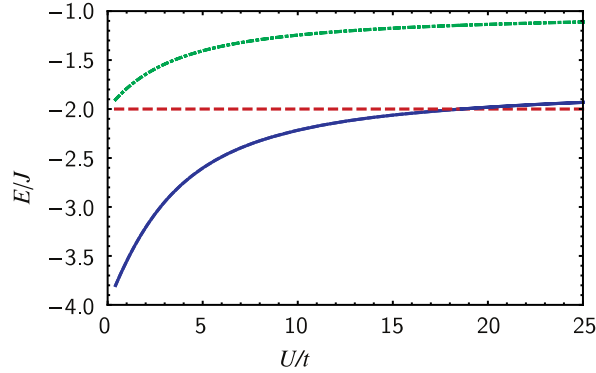


Figure 3.2.: Low-energy excitation spectrum of three fermions in a plaquette plotted against U/t . The energy of the states with $S = 1/2$ are presented in blue and green. The dashed red line shows the $S = 3/2$ configuration that is lowest in energy for $U/t > 18.6$ (inset). Adapted from [Ste10].

into account the connectivity condition¹ a plaquette filled by three fermions is the smallest non-trivial system that can fulfil all requirements [Tas98]. A proposal to realize this system with cold atoms by von Stecher et al. [Ste10] quantifies the energy spectra for its possible spin configurations (figure 3.2). Let us first consider the limit of infinite on-site interactions. As predicted by Nagaoka in this regime the ground state is given by a ferromagnetic arrangement of the fermions with spin $S = 3/2$ at an energy of $E = -2t$. Configurations of spin $S = 1/2$, which form a doublet, are higher in energy. However, going to weaker interactions a crossing of the $S = 1/2$ and the $S = 3/2$ branch takes place (inset figure 3.2). The reason for the crossing is the following. The energy of the ferromagnetic state does not change with U as the Pauli exclusion principle always forbids double occupancy. However, the spin doublet states decreases with decreasing U because admixtures to the state from doubly occupied states start to play a role. As a result for interactions $U/t < 18.6$ the ground state is given by an $S = 1/2$ state.

3.2. Majorana Bound States

It is a common feature of neutral bosons such as photons to be their own antiparticle. This differs for fermions. In the 1930s Ettore Majorana proved that potentially also neutral fermions being their own counterpart can exist but so far experimental proof of a fundamental particle with these properties is missing. However, in modern physics the concept of quasiparticles called Majorana bound

¹To fulfil the connectivity condition each site of the lattice needs to be part of a loop that consists at most of four lattice sites.

states—which are in some sense half of the well known Dirac fermions—attracted a lot of attention. In this section we introduce what Majorana fermions are, how they are connected to quasiparticles bound to defects in 1D condensed matter systems and why those are especially interesting for quantum computation. At the end of this section we discuss how to approach Majorana bound states experimentally.

3.2.1. Ettore Majorana's Discovery

In 1928 Paul Dirac presented an approach to overcome the limits of the purely real Klein-Gordon equation [Dir28]. In contrast to the Schrödinger equation the Klein-Gordon equation governs the relativistic regime but as it is a second order differential equation it lacks the possibility to deduce the time evolution of the wave function ψ , given ψ at a particular time because also $\dot{\psi}$ at this time would be needed as an initial condition. One would therefore aim for a first order differential that respects also a symmetry between energy and momentum. Therefore Dirac's original equation reads

$$i\hbar\frac{\partial\psi}{\partial t} = [c(\alpha_0 p_0 + \alpha_1 p_1 + \alpha_2 p_2 + \alpha_3 p_3) + \beta mc^2] \psi. \quad (3.2)$$

Here c is the speed of light, m is the mass, p_0 is the energy divided by the speed of light and p_1, p_2, p_3 are the components of the momentum vector. The α_i for $i = 0, 1, 2, 3$ and β turn out to be operators that are independent of the p_i and of time and space coordinates. Furthermore consistency with Klein-Gordon equation is demanded. Dirac found a set of complex 4×4 matrices meeting these conditions. Then the Dirac equation 3.2 actually consists of four coupled equations. The solutions describe spin-1/2 particles, i.e. the spin up and down components for particles (for positive energy solutions) and antiparticles (for negative ones). Dirac's predictions of antiparticles having the same mass but opposite charge as the particles turned out to be a great success as only a few years later experimental proof for the existence of the positron, the antiparticle of the electron, was provided [And33].

A decade after Dirac published his famous equation Ettore Majorana found out that there is also a possible choice of α 's and β that separates equation (3.2) into two systems of pairs of coupled, real wave equations. The solutions of these systems also describe spin-1/2 particles of the same mass. However, particles are neutral and they are their own antiparticles [Maj37]. These particles are their own counterpart, i.e. particle creation and particle annihilation is described by the same operator $\hat{\gamma} = \hat{\gamma}^\dagger$. Majorana concluded that the neutrino is a potential candidate for such a particle which makes the concept of an anti-neutrino redun-

3. Avenues and Vision

dant. Up to today there is proof for many elementary particles that follow Dirac's predictions but not yet any for a Majorana fermion. This also explains why at his time Majorana's interpretation was in the shadow of the just experimentally detected Dirac fermions. Today, however, Majorana's ideas gain a lot of attraction. In the field of high energy and particle physics researchers try to confirm whether Majorana fermions can be found in nature by exploring the potential existence of a neutrinoless double-beta-decay [Sch82; Ale96].

Nuclei that have an even number of protons and neutrons are mostly stable against beta decay. However, a secondary process, called the two-neutrino double-beta decay, is often possible

$${}^A_Z X \rightarrow {}^A_{Z+2} X + 2e^- + 2\bar{\nu}_e. \quad (3.3)$$

Here X stands for the decaying element, A for the mass number, Z the atomic number, e^- denotes an electron and $\bar{\nu}_e$ an anti-neutrino. Yet, this is not the only process under discussion to exist. The neutrinoless double-beta-decay

$${}^A_Z X \rightarrow {}^A_{Z+2} X + 2e^- \quad (3.4)$$

could also possibly occur. This process would then be a proof of neutrinos being their own antiparticles but there lacks experimental testimony of such a process and it is not even clear if it actually exists. Process (3.4) would not conserve the Lepton number. As a far reaching implication this could even help to explain the imbalance of matter and antimatter in the universe which is still a unsolved problem [Dav08].

3.2.2. Majorana Zero Modes in Condensed Matter Systems

In condensed matter systems Majorana fermions can emerge as quasiparticles that describe collective excitations in topological superconductors. These so called Majorana bound states or Majorana zero modes are an even hotter topic than their nuclear physics eponym (detailed discussions on Majorana bound states can be found in several reviews, e.g. [Ali12; Bee13; Sar15]). They inherit their name from the fundamental Majorana particles because their creation operators turn out to be hermitian as well. However, their core feature—which is their very special exchange statistics—is not applying to fundamental Majorana fermions. This property makes them potentially extremely useful for quantum computation.

Roughly spoken, the idea is to split up the fermion operators in the condensed matter many-body system into a real and imaginary part. In general, this rewriting has of course no physical implication. Yet, it turns out to be useful under

certain conditions, when topological defects come into play as the underlying physics of the system are then best described by these quasiparticles.

Topological Superconductors

Topological superconductors are of interest in this discussion their most intriguing feature is that they can host Majorana zero modes. As we only give a short insight into the topic the interested reader is referred to the reviews of Hasan et al. [Has10], Qi et al. [Qi11] and Sato et al. [Sat17]. Conceptually, topological superconductors are quite similar to topological insulators. The unique feature of the latter is a fully insulating bulk gap and gapless edge or surface states protected by time-reversal symmetry. Similarly, a topological superconductor has a superconducting bulk with a pairing gap and gapless surface states consisting of Majorana fermions. The topological structure of such systems is reflected in the wave function. From the mathematical field of topology we know that, for instance, a cup and a donut are topologically connected. We apply this idea now to wave functions. Any many-body wave function that is adiabatically connected to a combination of atomic wave functions is considered topologically trivial. For a many-body wave function describing a topological state, there exists no such connection.

The observation of the quantum Hall effect in 1980 proofed for the first time the existence of topologically non-trivial states [Kli80; Tho82]. Soon it was discovered that a whole group of many-body systems with a gap separating the (degenerate) ground state from the excited states can possess topological properties. They can be classified by finding integer numbers that represent their topology. The Chern number is an example of a topological invariant that can express the topological charge² of the system. For our purposes spinless one- and two-dimensional systems that exhibit superconducting p -wave pairing are especially useful. Let us stress that the reduced dimensionality will be crucial. Under these conditions a pair of quasiparticles being bound to a localized defect in the ordered state of the system can be excited at zero energy cost. Such a localized defect can be a vortex [Rea00] or a domain wall [Kit01], in two or one dimensions respectively. The binding gives rise to the name Majorana bound states for these quasiparticles. Alternatively, entitling them Majorana zero modes reflects that their creation costs zero-energy. For a system that can host a pair of Majorana quasiparticles the ground state would then be twofold degenerate³.

²The term topological charge and topological quantum number are used synonymously in this thesis.

³It should be mentioned that there exist other systems as well that can host Majorana modes such as $\nu = 5/2$ fractional quantum Hall states.

3. Avenues and Vision

A system being in a topological phase goes along with the fact that the many-body quasiparticle states exhibit very special exchange statistics. These so called non-Abelian statistics are subject of the next chapter.

Non-Abelian Statistics and their Significance for Universal Quantum Computation

The aim of this section is to show that lowering the dimensionality from three to two gives rise to richer exchange statistics of identical particles.

As a starting point it is helpful to consider the adiabatic exchange of two indistinguishable particles in a three dimensional space. We assume that the particles are originally located at positions $(\mathbf{r}_1(t_1), \mathbf{r}_2(t_1))$ and move to final positions $(\mathbf{r}'_1(t_2), \mathbf{r}'_2(t_2))$. Due to the fact that the particles are identical it is clear that the final position cannot be distinguished from $(\mathbf{r}'_2(t_2), \mathbf{r}'_1(t_2))$. In the following it is useful to express the example in terms of the centre of mass coordinates and relative coordinates of the system. Only in the relative coordinates $\mathbf{r} = \mathbf{r}_1 - \mathbf{r}_2$ we can possibly see an effect of exchanging the particles. If its absolute value is fixed, the relative coordinates can be visualized as the surface of a sphere (see figure 3.3 a)).

We consider the situation when particles are finally detected at the initial positions. Nothing special happens in the first scenario (I) where the particles just move around and go back to their initial position

$$\psi_1(\mathbf{r}_1)\psi_2(\mathbf{r}_2) \rightarrow \psi_1(\mathbf{r}_1)\psi_2(\mathbf{r}_2). \quad (3.5)$$

But for an observer it looks also the same if they are getting exchanged (II). This means \mathbf{r} goes to $-\mathbf{r}$, i.e.

$$\psi_1(\mathbf{r}_1)\psi_2(\mathbf{r}_2) \rightarrow \psi_2(\mathbf{r}_1)\psi_1(\mathbf{r}_2). \quad (3.6)$$

In the second case another exchange brings the particles back to their initial position (III). Scenario III can be continuously deformed into the trivial first scenario and thus is trivial as well⁴. A feature of these paths is that they can be shrunk into a single point. The two fixed endpoints, which cannot be reduced to a single point, distinguish path II. The physical implication is that the two-particle wave function gathers a phase θ

$$\psi_1(\mathbf{r}_1)\psi_2(\mathbf{r}_2) = e^{i\theta}\psi_1(\mathbf{r}_1)\psi_2(\mathbf{r}_2). \quad (3.7)$$

⁴The mathematical expression for the possibility of deforming them one into another is that they are in the same (in this case trivial) homotopy class.

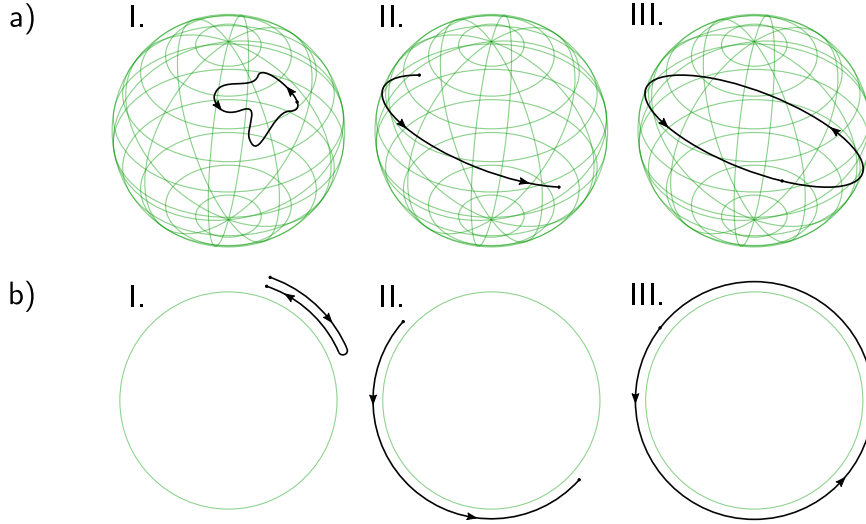


Figure 3.3.: Relative coordinates of two particles in three (a) and two (b) dimensions. Some adiabatic movement contractible to a single point is not changing the wave function (I). An adiabatic exchange of the particles, which moves the relative coordinate to the antipodal point, gives rise to a phase (II). Exchanging them twice (III) can be traced back to case I in three dimensions but in two dimensions multiplies a phase factor to the two-particle wave function.

Considering that two exchanges cancel the effect means θ can only take the values 0 and π referring to bosons and fermions, respectively.

This does not hold for a two dimensional system. The different topology, now represented by a circle (figure 3.3 b)), prevents that the path describing a double exchange of the particles is contractible to a single point because the space is multiply instead of singly connected as in 3D. The wave functions gather a phase but, of course, $|\psi_1(\mathbf{r}_1)\psi_2(\mathbf{r}_2)|^2 = |\psi_2(\mathbf{r}_1)\psi_1(\mathbf{r}_2)|^2$ still holds. However, the difference is that θ can now take in principal any value. Quasiparticles in a two dimensional space owning these special exchange statistics go under the name of anyons. For later use, let us denote the phase of a clockwise exchange of two anyons a and b with θ_{ab} .

From a mathematical point of view these adiabatic processes, which we have just considered, belong to the braid group. The braid group \mathbb{B}_N provides a suitable way to describe the trajectories of N indistinguishable particles that are moved from an initial position at time t_0 to a final position at time t_1 . The group is represented by $N - 1$ generators. A better understanding of the braid group can be obtained with an example, in our case we take four particles (figure 3.4).

3. Avenues and Vision

The three generators σ_1 , σ_2 and σ_3 correspond to the counterclockwise exchange⁵ of particle i and particle $i + 1$ (without loss of generality the particles can be labelled in an arbitrary way). With the visualization in figure 3.4 one can see how the connection with the word “braiding” came about. Exchanging particles adiabatically fulfils the following conditions:

$$\begin{aligned} 1. \quad & \sigma_i \sigma_j = \sigma_j \sigma_i && \text{for } |i - j| \geq 2 \\ 2. \quad & \sigma_i \sigma_{i+1} \sigma_i = \sigma_{i+1} \sigma_i \sigma_{i+1} && \text{for } 1 \leq i \leq N - 1. \end{aligned} \tag{3.8}$$

For the example of four particles both relations can be shown (figure 3.4 b) and d)). In spite of similarities the braid group needs to be distinguished from the permutation group in two dimensions. Although they satisfy almost the same relations, there is one fundamental difference: The permutation group additionally demands $\sigma_i^2 = 1$. Therefore, the number of its elements are given by the $N!$ possibilities to permute N particles. In figure 3.3 we saw what happens if one braids two particles twice. Whereas in three dimensions the braid group meets the additional condition of the permutation group—they are equal—there is an important difference between them in two dimensions. In contrast to the finite permutation group, the braid group is infinite because the phase θ can take any value.

The 2D system in figure 3.3 is a one-dimensional representation⁶ of the braid group. These “ 1×1 ” matrices are basically just numbers and thus commute. An example them are quasiparticles in fractional quantum Hall states. However, going to higher-dimensional representations of the braid group the exchange statistics are even more exotic as we will see in the following. Braiding can in this case even transfer a system into a completely different state. It is obvious that higher dimensional representations (higher dimensional matrices), as a rule, do not commute (see also figure 3.4). The corresponding quasiparticles are thus called non-Abelian anyons.

To understand conceptually what makes non-Abelian so special and why they are potentially of great use one first has to introduce the concept of fusion. When two anyons are brought close to each other they can fuse into a third particle. For our purposes particles can be classified into three different topological categories: those with a trivial topology (i.e. they are topologically equivalent to the vacuum), those with a fermionic topology and those with an anyonic topology. For

⁵A clockwise exchange is described by the inverse of the operator σ_i^{-1} .

⁶The existence of a n -dimensional representation of a group means that the group can be mapped with a homomorphism to a system of $n \times n$ matrices.

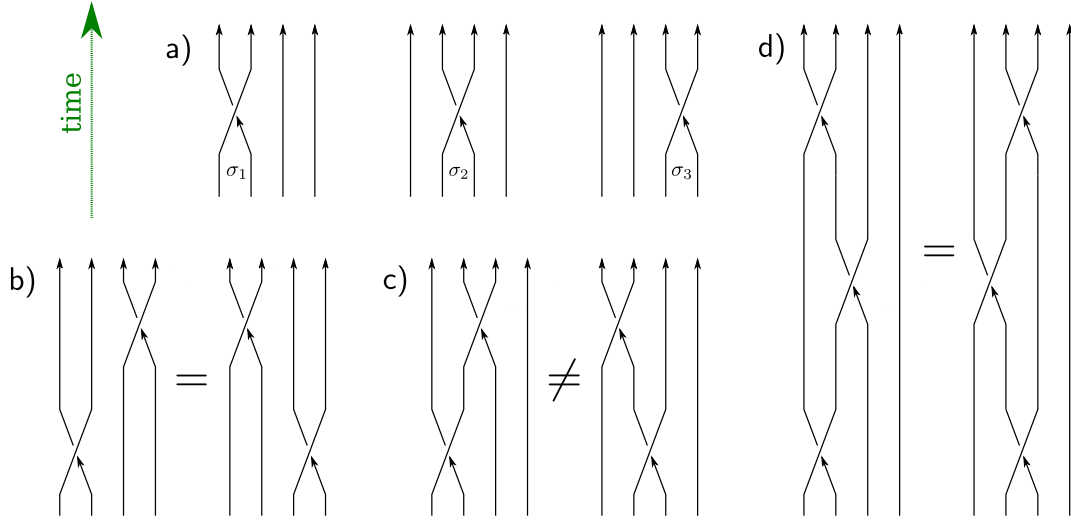


Figure 3.4.: Representation of the braid group \mathbb{B}_4 . a) The group consists of three generators. Figure (b) and (d) visualize the first and second braiding relation, respectively (equation (3.8)). c) In general, the group is not commutative.

the fusion process only the topological type of the particles is of interest. Naively, one would expect two particles, each with a certain topological charge, to fuse in a deterministic way into a third state of defined topology. This is, however, not true in a system with non-Abelian statistics. If here two anyons are combined they can either fuse into the vacuum or a fermion. The phase gained by exchanging two non-Abelian anyons a and b depends now also on the fusion output c , thus the phase should be appropriately denoted by θ_{ab}^c . It is very important to emphasize that non-Anyons are always connected to a degenerate ground state separated by an energy gap. The property that the system has (at least) two states that both minimize its energy makes it even possible that a pair of anyons can be created with zero energy cost from the vacuum. More complex systems hosting more than a pair of anyons are especially interesting because in certain configurations braiding can even evolve the system from one ground state into the other. Adiabaticity ensures that the system never leaves its subspace of degenerate ground states. Majorana zero modes bound to a localized disturbance⁷, shortly introduced in section 3.2.2, fulfil this condition.

⁷Importantly, the non-Abelian statistics only arise when a Majorana quasiparticle is bound to a topological defect and are not connected to fundamental Majorana particles.

3. Avenues and Vision

Altogether these properties make non-Abelian anyons like Majorana bound states very intriguing for quantum computation:

1. As the Majorana fermions are bound to topological defects they can be used to store information in a highly non-local way. Therefore they are robust against weak local perturbations.
2. The degenerate ground states are protected by an energy gap.
3. The existence of different fusion channels can be exploited in order to express the two states $|0\rangle$ and $|1\rangle$ of a qubit.
4. Braiding and the existence of different fusion channels provide the basics for unitary gate operations on a qubit system. The actual fusion process can be used for measurement of the final state. A better understanding of the encoding, the application of gate operations and the readout can be obtained in appendix A or the reviews [Nay08; Lah17].
5. Braiding operations are fault tolerant because they depend only on the topology of the process. In other words this means that they are robust against wiggles in the braid path.

Though braiding operations are unitary and can be used to express most of the gates required for universal quantum computation, they do not give a complete set of gates [Kit03]. Different approaches try to implement the missing $\pi/8$ - phase gate. One options would be the additional use of non-topological operations to make the set of gates complete [Bra06]. The problem is that they are unprotected and thus exhibit of course a source of error. However, together with additional error correction schemes non-Abelian anyons are so far still the best approach for the experimental implementation of universal quantum computation. Besides this idea more challenging proposals try to work around the problem by coupling to other qubit systems, e.g. [Sau10].

A few words should as well be spent on some weak points that should be considered in a real system. Systematic errors in topological quantum computing can, for instance, occur due to uncontrolled coupling to the environment. Furthermore, perfect degeneracy of the ground state can only be obtained for a system with infinitely separated anyons. For a finite distance their wave functions overlap and thus they interact. This interaction, which decays exponentially with increasing distance between the particles, needs to be taken into account if the quasiparticles are not kept far enough from each other (the important length scale is set by the inverse of the gap parameter). Then states with different energies dephase with time.

The Kitaev Chain—A System that Hosts Non-Abelian Anyons

The fractional quantum Hall state at a filling factor of $\nu = 5/2$, which was found in GaAs quantum wells [Wil87], was the first finding of quasiparticles attributed to non-Abelian statistics [Moo91].

A decade later in 2000 Read and Green came up with a model of a topological p -wave superconductor in 2D where Majorana zero modes bind to vortex cores [Rea00]. Shortly after Kitaev proposed Majorana bound states to appear on an even simpler playground—a p -wave superconductive 1D wire [Kit01]. We will now further investigate this model.

To create a quasiparticle that is its own antiparticle an obvious approach is to create a superposition of an electron and a hole. This concept is quite reminiscent of Bogoliubov quasiparticles in superconductors. Usually Cooper pairs are in a spin singlet configuration of an s -wave superconductor because this state is energetically favourable. Thus a Bogoliubov quasiparticle reads $\hat{b} = u\hat{f}_\uparrow^\dagger + v\hat{f}_\downarrow$. Here \hat{f}_σ with $\sigma = \uparrow, \downarrow$ is the annihilation operator of a fermion, and u and v denote complex numbers. This operator generating Bogoliubov quasiparticles is, however, not hermitian. An appropriate operator needs to be not only chargeless but spinless as well. This condition is met by the construction $\hat{\gamma} = u\hat{f}_\sigma^\dagger + u^*\hat{f}_\sigma$ for which $\hat{\gamma}^\dagger = \hat{\gamma}$ holds. The spin part of the wave function is now in a triplet state and thus symmetric which means the spatial part needs to be antisymmetric in order to keep the antisymmetry of the overall wave function. This can be provided by the rather exotic p -wave pairing but not by s -wave pairing of the fermions.

With this in mind, we look at the Kitaev model that describes N spinless fermions in a one-dimensional p -wave superconducting chain with long-range order⁸ and open boundary conditions

$$\hat{H}_{\text{chain}} = -\mu \sum_{x=1}^N \left(\hat{f}_x^\dagger \hat{f}_x - \frac{1}{2} \right) - \sum_{x=1}^{N-1} \left(t \hat{f}_x^\dagger \hat{f}_{x+1} + |\Delta| e^{i\theta} \hat{f}_x \hat{f}_{x+1} + h.c. \right). \quad (3.9)$$

The N lattice sites can be unoccupied or occupied by applying the fermion creation operator \hat{f}^\dagger , μ denotes the chemical potential, t the hopping amplitude and $|\Delta|e^{i\theta}$ the superconducting gap.

Now, formally, the fermion operator of each site can be rewritten such that it is, roughly spoken, “split up” into a real and imaginary part

$$\hat{f}_x = \frac{1}{2} e^{-i\frac{\theta}{2}} (\hat{c}_{B,x} + i\hat{c}_{A,x}). \quad (3.10)$$

⁸The Kitaev chain is the lattice version of a spinless p -wave superconductor in a mean-field description.

3. Avenues and Vision

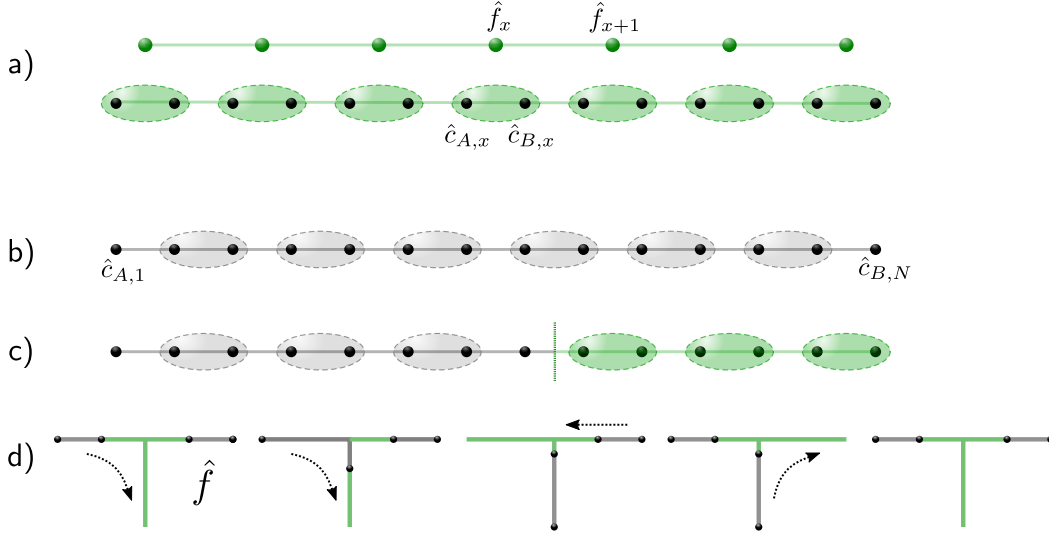


Figure 3.5.: The Kitaev chain. a) Fermions in a 1D chain can either be expressed by the fermionic operators \hat{f}_x or by the Majorana operators \hat{c}_A, x and \hat{c}_B, x . b) Under certain conditions Majorana operators of neighbouring sites pair up to a fermionic operator. At the boundaries isolated Majorana modes remain. c) Different chemical potentials create domain walls between topological and non-topological regions. d) With the help of a T-junction braiding operations can be performed with the 1D chain.

Inverting this equation

$$\hat{c}_{A,x} = -ie^{i\frac{\theta}{2}}\hat{f}_x + ie^{-i\frac{\theta}{2}}\hat{f}_x^\dagger, \quad \hat{c}_{B,x} = e^{i\frac{\theta}{2}}\hat{f}_x + e^{-i\frac{\theta}{2}}\hat{f}_x^\dagger, \quad (3.11)$$

one sees at once that the Majorana operators $\hat{c}_{\alpha,x}$ with $\alpha = A, B$ are hermitian. Besides, their commutation relation is given by $\{\hat{c}_{\alpha,x}, \hat{c}_{\alpha',x'}\} = 2\delta_{\alpha,\alpha'}\delta_{x,x'}$. The Hamiltonian in this new basis

$$\hat{H}_{\text{chain}} = -\frac{\mu}{2} \sum_{x=1}^N (i\hat{c}_{B,x}\hat{c}_{A,x} + 1) - \frac{i}{2} \sum_{x=1}^{N-1} [(t + |\Delta|) \hat{c}_{B,x}\hat{c}_{A,x+1} + (-t + |\Delta|) \hat{c}_{A,x}\hat{c}_{B,x+1}] \quad (3.12)$$

describes the original fermions in terms of pairs (figure 3.5 a)). The hopping term gives rise to nearest neighbour hopping and third nearest neighbour hopping of the quasiparticles in Majorana basis. Two cases can be easily discussed:

In the special case of $|\Delta| = t = 0$ and negative μ the system's energy is minimized when all lattice sites are unoccupied and any excitation costs a finite energy

$|\mu|$. This phase is topological trivial and the treatment in terms of Majorana operators is not giving additional insight into the system's properties⁹.

The second situation arises for $\mu = 0$ and $t = |\Delta| \neq 0$. Then the Hamiltonian reduces to

$$\hat{H}_{\text{chain}} = -it \sum_{x=1}^{N-1} \hat{c}_{B,x} \hat{c}_{A,x+1}. \quad (3.13)$$

In this case Majorana fermions belonging to adjacent sites form a pair (figure 3.5 b)). This is even clearer if one rewrites $\hat{d}_x = 1/2(\hat{c}_{A,x+1} + i\hat{c}_{B,x})$ and thus

$$\hat{H}_{\text{chain}} = 2t \sum_{x=1}^{N-1} \left(\hat{d}_x^\dagger \hat{d}_x - \frac{1}{2} \right). \quad (3.14)$$

In the bulk one needs to pay an energy $2t$ to create a fermion d_x with $x \in \{1, \dots, N-1\}$. But at the end of the chain there exist now Majorana modes $\hat{c}_{A,1}$ and $\hat{c}_{B,N}$ that are decoupled from the Hamiltonian (figure 3.5 a)). To occupy them by applying $\hat{\gamma} = 1/2(\hat{c}_{A,1} + \hat{c}_{B,N})$ costs no energy—thus the name Majorana zero modes. From this follows that two different ground states are possible. The system is now in the topological phase described in the previous chapter. For our choice of boundary conditions the two Majorana bound states at the edges give rise to a highly non-local fermion. If we had chosen periodic boundary conditions instead, these two Majorana modes would just pair up to a normal fermion mode.

Of course the cases, we have looked at, were idealized. There is as well a regime where a topological phase arises for $\mu \neq 0$ and $t \neq |\Delta|$ as long as $2t > |\mu|$ holds. Under these conditions a finite gap to protect the degenerate ground state still exists but the bulk modes are partially occupied.

However, for this—from an experimental point of view more realistic case—the wave functions of the two Majorana zero modes are exponentially localized at the ends of the wire. For finite distances of the modes they overlap and the twofold degeneracy is lifted as already mentioned at the end of the last paragraph. Under the conditions that the two edge modes are much further apart from each other than the inverse gap this effect can be neglected. Furthermore, as the Majorana zero modes are bound to a defect, the system is robust against thermal fluctuations because they cannot cause anyonic quasiparticle excitations by accident.

The aim is now to use the Majorana zero modes for quantum computational purposes as introduced in section 3.2.2. It is easy to imagine a braiding process in a two-dimensional system. In one dimension, however, braiding is ill-defined

⁹Alternatively, one could as well consider the case of positive μ . Then the energy is minimal for a completely filled chain with Majorana fermions coupling to the original fermion lattice sites.

3. Avenues and Vision

as the only possibility to exchange two modes would mean to bring them close to each other and thus to lift the degeneracy. The problem can be solved by performing braiding operations in two dimensions with the help of a T-junction (figure 3.5 d)). Additionally, with the T-junction it is possible to braid more than the two Majorana bound of a single chain. As shown in figure 3.5 c) different chemical potentials along the T-junction can be exploited to create domain walls between non-topological regions ($\mu > 2t$) and topological ones ($\mu < 2t$). This is essential if one wants to express unitary operations on qubits within our construction (appendix A). As discussed above (section 3.2.2) for Majorana modes there exist two different fusion channels. Two of them can either annihilate to vacuum or they fuse to an ordinary fermion. Also this process is not restricted to Majorana fermions of the same topological domain but can also take place between two different topological regions [Ali11].

3.2.3. Signatures of Majorana Fermions and how to Measure them

As discussed in the previous chapter spinless p -wave superconductivity is a key requirement in order to engineer a system that can host Majorana bound states. Yet, they are extremely rare in nature. It is possible to overcome this limit with induced superconductivity. Following the proposals of Lutchyn et al. [Lut10] and Oreg et al. [Ore10] which are based on [Fu08] it is shown that the requirement of an effectively p -wave superconductive 1D chain can be complied with a semi-conductive wire surrounded by an s -wave superconductor if strong spin-orbit coupling and Zeeman splitting are present in the system. The underlying mechanism that inherits superconductivity is called superconductive proximity-effect (see e.g. [Lut10]). In a spin-orbit coupled system the degenerate spin bands shift with respect to each other (figure 3.6 a) and b)). In the presence of a magnetic field the Zeeman splitting leads to an avoided crossing. If the chemical potential lies within the gap that opens up and there is effectively only a single band involved which only holds a single spin projection (figure 3.6 c)). For an adequate choice of parameters the wire passes into the p -wave superconducting phase. Mourik et al [Mou12] first reported on signatures that were likely to stem from Majorana fermions in a InSb nanowire that was designed following the proposal presented above. Measuring the differential conductance they discovered a peak at zero bias voltage in their nanowire device that might be connected to the occupancy of a Majorana edge mode of the wire. However, these results are still under debate in the community [Sar15]. A conclusive measurement could be based on braiding or by the measurement of the 4π fractional AC Josephson in topological superconductors not discussed in this thesis [Rok12].

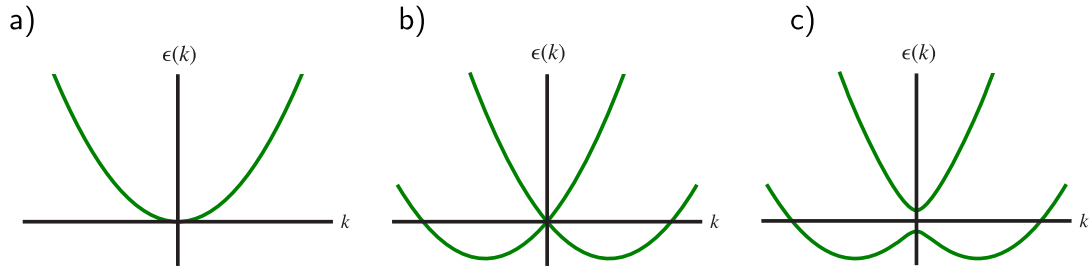


Figure 3.6.: Bandstructure. a) In the presence of no magnetic field and no spin-orbit coupling the dispersion relation of spin up and spin down electrons is identical. b) The two bands are displaced relative to each other in a strongly spin-orbit coupled system. c) Applying additionally a magnetic field opens up a band gap. If the chemical potential is placed within the gap the wire is effectively spinless. Adapted from [Sar15].

The tunability and the high degree of control of cold atoms makes them an interesting candidate for the search of Majorana bound states. However, the requirement of p -wave superconductivity poses a serious challenge. p -wave resonant gases suffer from very short lifetimes [Zha04; Gae07]. Although there exist proposals to work around the problem their complexity has prevented their realisation so far. Among others they include a proposal to adapt the idea of engineering p -wave superconductivity with the proximity-effect (see above) to cold atoms [Jia11].

We can conclude that although considerable efforts—especially in condensed matter physics—have been made, the unambiguous detection of Majorana fermions remains challenging.

4. Realization of an Ultracold 2D Fermi Gas

In this chapter we introduce the 2D setup which served as starting point for the upgraded experiment. We start out by discussing relevant properties of ${}^6\text{Li}$, followed by the description of the experimental sequence to create a quasi-2D gas. Finally, we give a short summary of the experimental results obtained over the last years with this setup. For details we refer to [Rie10] and [Nei17].

4.1. Properties of ${}^6\text{Li}$

In our experiment we work with the stable isotope of lithium ${}^6\text{Li}$. As it consists of three protons, three neutrons and three electrons the composite element is uncharged and fermionic. Its nuclear spin $I = 1$ and its electron spin $S = 1/2$ (${}^6\text{Li}$ has one electron in the outer shell) lead to a hyperfine splitting of the ground state into $F = 1/2$ and $F = 3/2$ (figure 4.1 a)). The degeneracy of the Zeeman levels can be lifted by applying a magnetic field. Already for a magnetic field of 30 G (1 G) for the $2^2S_{1/2}$ ($2^2P_{3/2}$) branch J and I decouple and one enters the Paschen-Back regime where the levels regroup according to the quantum number m_j . The six ground states are labelled from $|1\rangle$ to $|6\rangle$. All experiments are performed with (mixtures of) state $|1\rangle$, $|2\rangle$ or $|3\rangle$. We can convert the population from one state into another with a Landau-Zener passage by applying a radio frequency pulse. Throughout this thesis we use a mixture of the two lowest states ($|1\rangle$ and $|2\rangle$) which are separated by about 80 MHz in frequency for magnetic fields above 100 G. Interactions between two different species can be induced and controlled by applying a homogeneous magnetic offset field. ${}^6\text{Li}$ has an especially broad s -wave Feshbach resonance (see section section 2.2 around 800 G (figure 4.1 b)). At the Feshbach resonance scattering is resonantly enhanced and the s -wave scattering length diverges. Additionally, narrow p -wave resonances can be found at around 180 G for $|1\rangle$ - $|1\rangle$, $|1\rangle$ - $|2\rangle$ and $|2\rangle$ - $|2\rangle$ mixtures. The two imaging techniques used in our experiment, absorption and fluorescence imaging, both work with the transition from transition from $2^2S_{1/2}$ to $2^2P_{3/2}$ (D2-line) at $\lambda = 671$ nm of ${}^6\text{Li}$.

4. Realization of an Ultracold 2D Fermi Gas

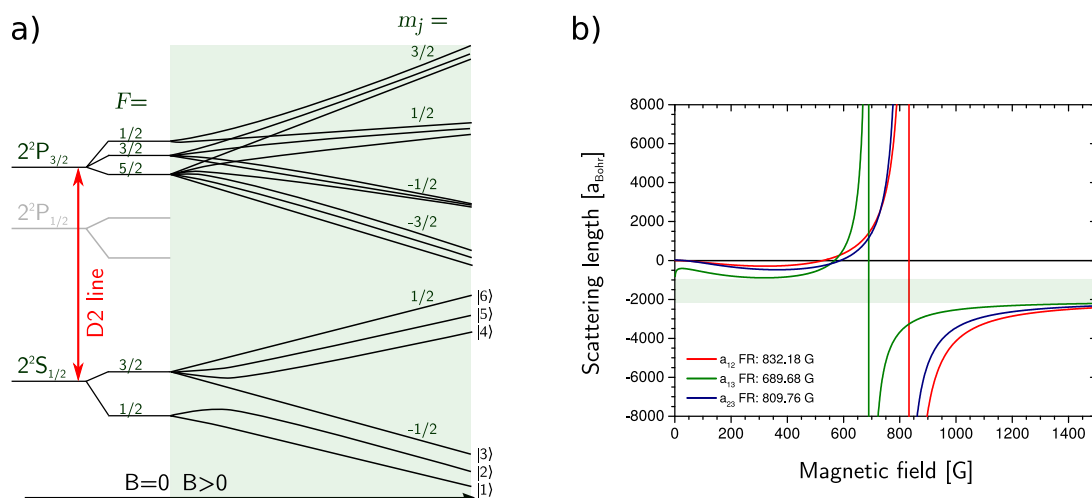


Figure 4.1.: a) Level structure of the lowest levels of ${}^6\text{Li}$. If a magnetic field is applied the degeneracy of the Zeeman levels is lifted. In the experiment we work with the three lowest hyperfine states of the ground state. Adapted from [Ber17]. b) Dependence of the scattering length on the magnetic offset field. A broad s -wave Feshbach resonance exists for all three possible mixtures [Nei17].

4.2. Experimental Sequence

To perform experiments in the regime of degeneracy a sophisticated preparation, comprising several cooling stages, is indispensable. The working principle of a magneto-optical trap (MOT), an optical dipole trap (ODT) and evaporative cooling are explained in section 2.1. We only give a short overview of the different steps here.

Working in the regime of 100 nK requires to shield the atom cloud as much as possible from collisions with thermal atoms of the environment. Consequently, we use ultra high vacuum achieved by combining titanium sublimators (position **A** in figure 4.2) and two ion-pumps (**B**) together with a non-evaporable getter coated experimental chamber. The main chamber (**C**) has an octagonal design allowing optical access along three horizontal axes and from the vertical axis. For the preparation of the sample an atomic vapour is produced from solid ${}^6\text{Li}$ in the oven at 350°C (**D**). Atoms enter the Zeeman slower (**E**) where they are decelerated to about 3% of their initial speed by exploiting absorption of a counter-propagating resonant beam (**F**) and spontaneous emission. The atoms' Doppler shift is compensated by the coils of the tapered Zeeman slower. At the main experimental chamber the speed of the atoms is sufficiently reduced to capture about 10^8 atoms in a magneto optical trap. The MOT consists of three pairs of counter-propagating, red-detuned, near-resonant beams and a pair of coils in

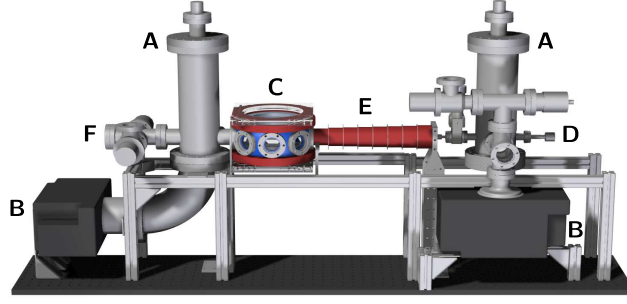


Figure 4.2.: Vacuum setup. Titanium sublimators (A) and ion-pumps (B) establish ultra high vacuum in the main chamber (C). A vapour of ${}^6\text{Li}$ is produced in the oven (D) of which a part is transferred through the Zeeman slower (E). During the transfer to the experimental chamber the atoms are cooled down with a counter-propagating beam of resonant light (F). Adapted from [Rie10].

anti-Helmholtz configuration (red in figure 4.2) producing a quadrupole field. In the MOT the atoms are cooled down to a few hundred microkelvin. To cool them down further they are loaded into an optical dipole trap¹. To load the atoms, which are in a mixture of the lowest two hyperfine states, from the MOT into the ODT the size of the cloud is reduced by decreasing the detuning and applying a steeper magnetic field gradient². The ODT consists of two crossed beams of perpendicular polarizations in the far red-detuned regime ($\lambda \approx 1064 \text{ nm}$).

Quantum degeneracy can then be achieved in the ODT by evaporative cooling. As high collision rates are favourable for this cooling technique we work with distinguishable fermions and a magnetic offset field in the vicinity of their Feshbach resonance. In this regime they are highly interacting. The offset field is produced by a pair of magnetic field coils, called Feshbach coils. After the evaporation we end up with about 10^5 atoms at a temperature of around 100 nK.

In the last step we want to load the degenerate sample from the cigar shaped crossed beam ODT (aspect ratio $1/\omega_x : 1/\omega_y : 1/\omega_z \approx 8.3 : 44 : 1$) into the quasi-2D trap. The latter trap is created by the interference pattern of a standing wave dipole trap (SWT). To load from the cigar shaped trap into a single central layer of the SWT it is important to reduce the axial extension of the ODT as far as possible. The size of the trap can be effectively reduced during the loading by creating a time-averaged potential in the horizontal plane with the help of an acousto optic modulator (AOM) so that up to 90% of the atoms can be transferred

¹As dipole traps have typically depths in the range below one millikelvin it is not possible to load the atoms directly into the ODT.

²For this purpose we use another set of coils, in the following referred to as Feshbach coils, which are closer to the atoms.

4. Realization of an Ultracold 2D Fermi Gas

to a single layer. The last step in the preparation is a further spilling process in the SWT. Due to an applied magnetic field gradient during the evaporation the atoms leave the trap very fast. This leaves us finally with about 35,000 atoms in a highly anisotropic potential at a temperature of about 70 nK. In units of the Fermi temperature T_F this corresponds to $T/T_F \leq 0.2$. The aspect ratio of the SWT given by $1/\omega_x : 1/\omega_y : 1/\omega_z \approx 330 : 330 : 1$ shows that it is energetically favourable for the system to populate a considerable amount of radial trap levels before axial excitations are of advantage for the system. As the chemical potential and the temperature are lower than the excitation energy in z -direction we can therefore assume to work in a quasi-two-dimensional regime.

For imaging the 2D system at the end of the experimental sequence we rely mainly on absorption imaging from top to bottom. Besides imaging in position space we are also able to detect the momentum distribution of the sample by taking an image after a certain time-of-flight. To this end the trapping potential is switched off. If the atoms evolve in a harmonic potential their position after a quarter of the trap period corresponds exactly to their momentum distribution. We use the Feshbach coils to create the required weak harmonic confinement in which we let the atoms expand [Mur14].

4.3. Previous Work on 2D Fermi Gases

The 2D experiment was initially designed to explore the crossover from a condensate of tightly bound molecules to weakly paired fermions in the Bardeen-Cooper-Schrieff (BCS) regime passing a strongly interacting regime (figure 4.3 a)). For a system with dimension lower than three no Bose-Einstein condensation is possible. However, in 2D a superfluid state in the form of a topological phase transition

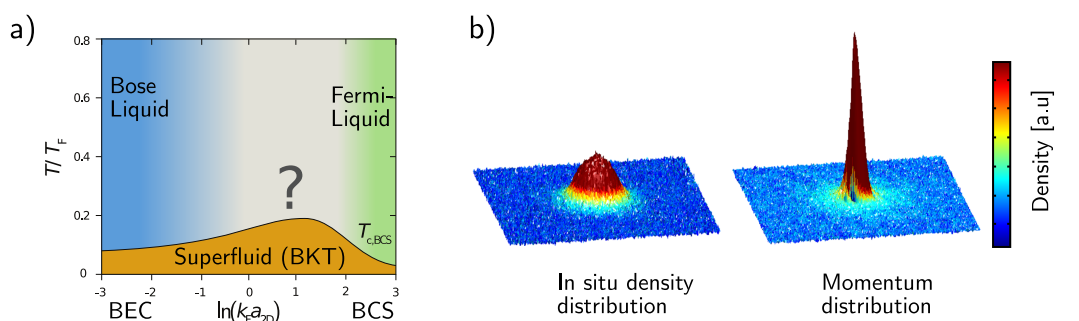


Figure 4.3.: Working in a quasi-two-dimensional regime. a) Schematic phase diagram for superfluid to BCS crossover. b) In situ density distribution and momentum distribution in the Berenzinskii-Kosterlitz-Thouless phase.

4.3. Previous Work on 2D Fermi Gases

being connected to the binding of vortices (Berezinskii-Kosterlitz-Thouless transition) still exists [Ber72; Kos73]. This phase transition was observed for the first time by our group (figure 4.3 b)) [Rie15], followed by further investigations of the condensate to BCS crossover [Mur15c] and the measurement of the thermodynamic equation of state for the crossover [Boe16]. In the strongly interacting regime, which is hard to approach theoretically, pairing was investigated in greater detail [Mur18b]. Differently to the BCS regime where the formation of pairs and their condensation happen simultaneously, it was discovered that in the strongly interacting regime pairs already form much earlier still in the normal phase of the gas. The most recent experiments on the 2D setup were focused on the observation of the breathing mode of the quantum gas. For both observables, position and pair momentum distribution of the superfluid, strong signatures for anomalous breaking of scale invariance in the 2D system were found [Hol18; Mur18a].

5. Experimental Extension

On the way beyond the capabilities of our group's approved 2D system we added a major extension to the setup in the course of this thesis. At its heart is the possibility of spatial light modulation paving the way to create tailor-made optical potentials projected onto a plane. One of the expectations regarding the new setup is the possibility of highly controlled lattice experiments at very low entropy. Another novel feature concerns the detection. The implementation of a high-resolution objective together with an EMCCD camera shall allow us to perform spin-resolved single-atom imaging in free space in future. These trapping and imaging tools at hand we are in a perfect position to start the investigation of strongly correlated many-body systems.

In this chapter we first explain how to identify phase patterns that lead to a desired potential landscape. We continue with a detailed description of the extension, followed by an overview of the implementation. We end with a separate discussion of the objective and single atom imaging.

5.1. Creating Tailor-Made Potentials

The experimental add-on is designed to allow the realization of almost arbitrary 2D trapping potentials. We address this challenge with a spatial light modulator (SLM) that modulates the phase of an incoming beam and therefore shapes a coherent beam in the way we desire. The SLM used here was already subject of different bachelor theses within our group [Hol14; Kug15; Cla16]. Beside SLMs, which are based on liquid crystals, another established candidate for light shaping are digital mirror devices which work with electro-mechanically controlled micromirrors. Depending on the application either one or the other device might be more suitable [Tur17]. For our purposes the preferred choice is a phase-modulating SLM since its higher diffraction efficiency is advantageous in order to create deep trapping potentials. Furthermore, an SLM is better suited for the creation of time-dependent patterns because it naturally changes in a continuous way between different potentials.

5. Experimental Extension

According to equation (2.23) a given SLM phase pattern and input field $U(x, y, z_{\text{in}})$ translate into an intensity distribution in the atoms' plane as

$$I_{\text{target}}(x, y) = 1/(\lambda f)^2 |\mathcal{F} [U(\cdot, \cdot, z_{\text{in}}) e^{-i\phi_{\text{SLM}}}] \left(\frac{x}{\lambda f}, \frac{y}{\lambda f} \right)|^2. \quad (5.1)$$

An important question to ask with this knowledge is, how can we determine a phase pattern that leads to a desired trapping potential $I_{\text{target}}(x, y)$? It is easiest to consider an incident plane wave. Its incident angles θ_x, θ_y result only in a shift of the intensity pattern in the atoms' plane. Therefore, for the sake of simplicity, we can assume $\theta_x = \theta_y = 0$ and set $U(x, y, z_{\text{in}}) \equiv \sqrt{I_{\text{pw}}}$. In a more realistic scenario one should consider a collimated Gaussian beam that has approximately flat wavefronts in the SLM plane and the atoms' plane and a Gaussian intensity distribution. Given approximate knowledge of the form of the incident wave and the constraints that we measure only intensities $I_{\text{target}}(x, y)$ in the Fourier plane and only modify the phase $\phi_{\text{SLM}}(x, y)$ in the SLM plane one cannot apply a simple Fourier transformation of the desired intensity pattern in the atom plane in order to trace back how $\phi_{\text{SLM}}(x, y)$ needs to be chosen.

However, there exist several numerical methods to receive a possible approximated SLM-phase pattern. Within our group different approaches to determine $\phi_{\text{SLM}}(x, y)$ for discrete and continuous targets were tested and evaluated [Hol14; Hol17]. In order to create an intensity pattern in the atoms' plane, such as an array of single spots, it is important to use an algorithm that refracts light from the whole SLM into each spot. Two different algorithms are predominantly applied in our experiment: One method called mixed-region amplitude freedom (MRAF) algorithm [Pas08] is based on an iterative Fourier transform algorithm where one starts with an arbitrary phase guess $\phi_{\text{SLM}}(x, y)$ and then propagates the field back and forth between SLM plane and atom plane with Fourier transforms until the calculation converges to a phase pattern that yields the desired intensity distribution in the atom plane (figure 5.1 a) and b)). The second algorithm is known as conjugate gradient descent (CGD) algorithm. The main idea here is to introduce a suitable cost function that describes the deviation from the desired light pattern and then to minimize this function gradually [Har14]. When comparing both algorithms, the MRAF algorithm is faster and more reliable (tested in [Hol14]) but has a lower light utilization efficiency than the CGD algorithm. For continuous targets the MRAF algorithm diffracts light into a noise region which reduces the light utilization efficiency of the SLM to about 40%. For discrete targets or when the CGD algorithm is applied the efficiency is up to 90%.

The finite size of the SLM, which makes it act as an aperture, naturally leads to a discrete description of the so called drawing area in the Fourier plane as both planes are connected by a Fourier transformation. The smallest structure

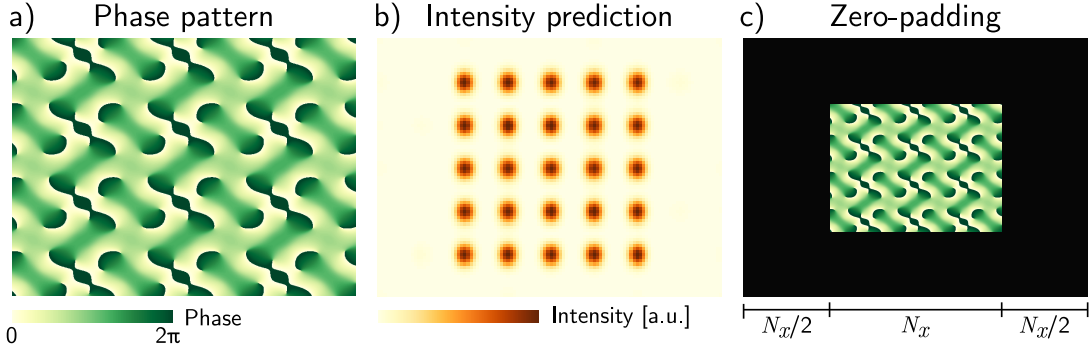


Figure 5.1.: Creation of trapping potentials. a) A phase pattern can be numerically calculated by the MRAF algorithm predicting the desired potential landscape in the atoms’ plane (b). c) A zero-padding added around the phase pattern is necessary to obtain the maximal resolution in the atoms’ plane. The black frame are the pixels which are set to zero.

$\Delta X \times \Delta Y$, denoted as focal unit according to [Bij13], the SLM itself can create in the drawing area is set by the inverse of the SLM chip size $L_x \times L_y$ via $\Delta X \times \Delta Y = \lambda f / L_x \times \lambda f / L_y$. In our setup this would lead to $\Delta X \times \Delta Y = 729 \text{ nm} \times 960 \text{ nm}$ in the atoms’ plane¹. However, this is finer than the smallest structures that the objective can resolve as discussed in section 5.4. Still, the focal unit is a useful concept to set the pixels of a desired phase pattern.

As explained the smallest structure the SLM can produce by itself after the Fourier transformation is of the size of a focal unit or expressed in the language of Fourier transformations this is the highest frequency component. Yet, the Nyquist–Shannon sampling theorem [Sha49] states that in order to reconstruct a signal correctly its sampling rate needs to be at least twice the highest frequency component. For this reason the focal unit is not precise enough to make appropriate predictions of the intensity distribution for a given SLM phase pattern. We can meet this requirement with the trick to assume for all calculations that L_x and L_y are twice as long as the SLM chip but to set only the inner pixels with the phase pattern that is actually applied to the SLM. All other pixels are set to zero for the calculations (figure 5.1 c)). The technique is at the cost of computation time and memory as the array to process is four times bigger now.

In a real setup one needs to compensate for aberrations in the optical system as well as for imperfections in the response of the SLM itself. A very convenient

¹Since we add an additional 4f-setup between SLM and objective, which projects the Fourier pattern on the atoms’ plane, the the size of a focal unit is given by $\Delta X \times \Delta Y = \lambda f_3 f_{\text{objective}} / (L_x f_2) \times \lambda f_3 f_{\text{objective}} / (L_y f_2)$ according to figure 5.3.

5. Experimental Extension

property of the SLM is that it can be used to correct these imperfections by applying an appropriate phase pattern to it. Therefore, the finally applied phase pattern is a sum of different correction patterns and the numerically calculated pattern of the desired potential [Hol14]. A correction pattern that takes care of imperfections of the liquid crystal chip itself and the glass window of the SLM is already provided by Hamamatsu. One can identify further aberrations in the beam path by a Shack-Hartmann method [Bow10]. The underlying principle is to scan over all positions (x_0, y_0) of the whole SLM chip and to deduce the wavefront errors stemming from each position. The method was tested in [Hol14]. Most importantly the technique can be applied while trapping atoms allowing to correct for aberrations even due to the vacuum window. Besides these correction patterns, it is very useful to apply the pattern of a Fresnel lens to the SLM. This allows to fine-tune the focus with respect to the atom plane. Finally, the total phase pattern contains a linear gradient in addition to shift the applied phase pattern away from the zeroth order of the SLM and a pattern derived with the help of a CCD camera feedback. Their importance will be discussed in the next section where the complete setup is explained.

5.2. Extensional Setup

This section gives an overview of the extension that was implemented in the course of this thesis. The add-on is composed of three breadboards which host the SLM, a high-resolution objective and an electron multiplying charge-coupled device (EMCCD). Figure 5.2 shows schematically how the new elements are integrated into the experiment. Together, they add a further layer of optics to the experiment. Far red-detuned trapping light is prepared on the breadboard that hosts the SLM (**A**), it is then guided to an adjacent vertically mounted breadboard placed above the main chamber (**B**). The high-resolution objective (**C**) attached to the latter forms a 6f-setup together with the optical system after the SLM and it focuses the light into the atoms' plane. Single-atom imaging shall be enabled by the newly implemented EMCCD camera which is mounted onto an additional breadboard (**D**). Due to the modification this breadboard does now also include the outcoupler of a beam used for absorption imaging with a wide field of view that was already part of the experiment before.

5.2.1. Optical Setup of the SLM

In our experiment we can now project tailor-made optical potentials onto the atoms using the SLM-setup. We use an X10468-03 LCOS spatial light modulator

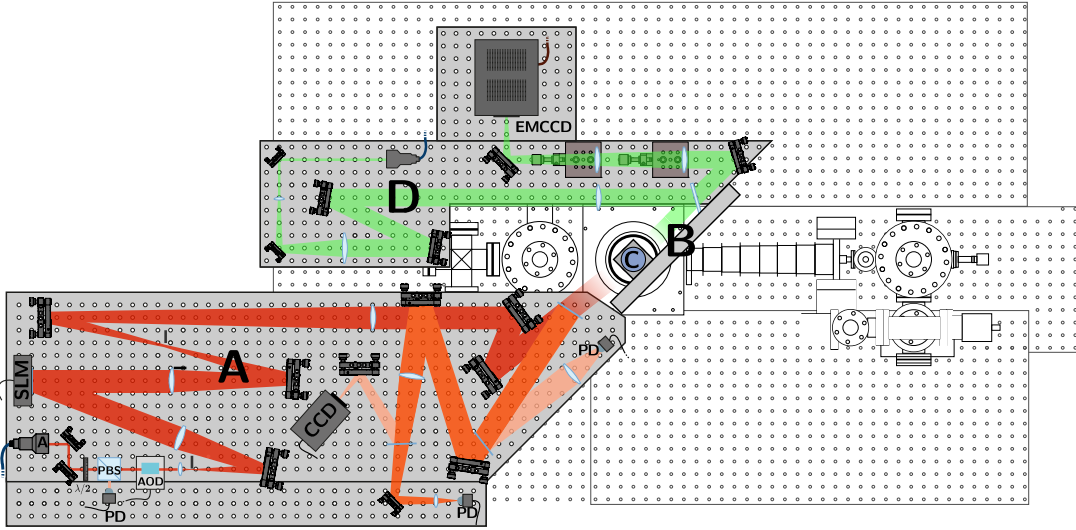


Figure 5.2.: Schematic overview of the extension. In the foreground the arrangement of the extension is shown. In the background the main chamber, Zeeman slower and the vacuum pumps are depicted as an orientation. Breadboard **A** hosts the SLM, the vertical **B** is placed above the vacuum chamber. Attached to it is the objective (**C**). The new imaging setup is arranged at breadboard **D**.

from Hamamatsu. The device consists of an array of 792×600 pixels electrodes each of which can be addressed separately. Phase shifts between 0 and 2π can be tuned in 256 steps. The electrodes are driven with constant voltage with alternating sign at 240 Hz to prevent drifts of the molecules within the alignment layer. Due to the high speed the orientation of the molecules is not affected—only the polarization of each liquid crystals alternates. Further specifications of the X10468-03 LCOS-SLM can be found in appendix B.

As explained in section 2.1 dipole traps in our experiment are created with far red-detuned light. The SLM-trapping light is provided by the Mephisto-seedlaser which is amplified by the NUFERN-fibre amplifier. In front of the high-power fibre which directs the light to the SLM-breadboard an acousto-optic modulator (AOM) is placed. It serves as a fast switch for the light and is used as a part in the intensity feedback loop. The trap created by the SLM confines the atoms in the x - y -plane and depending on the pattern also in the z -direction. Additional z -confinement can be achieved with the 2D-trap introduced in chapter (chapter 4).

Figure 5.3 shows the optical setup containing the SLM that is used to prepare the trapping light. At the outcoupler (**A**) the beam is collimated such that it has a diameter of 1.7 mm. It subsequently passes a $\lambda/2$ -waveplate and a polarizing

5. Experimental Extension

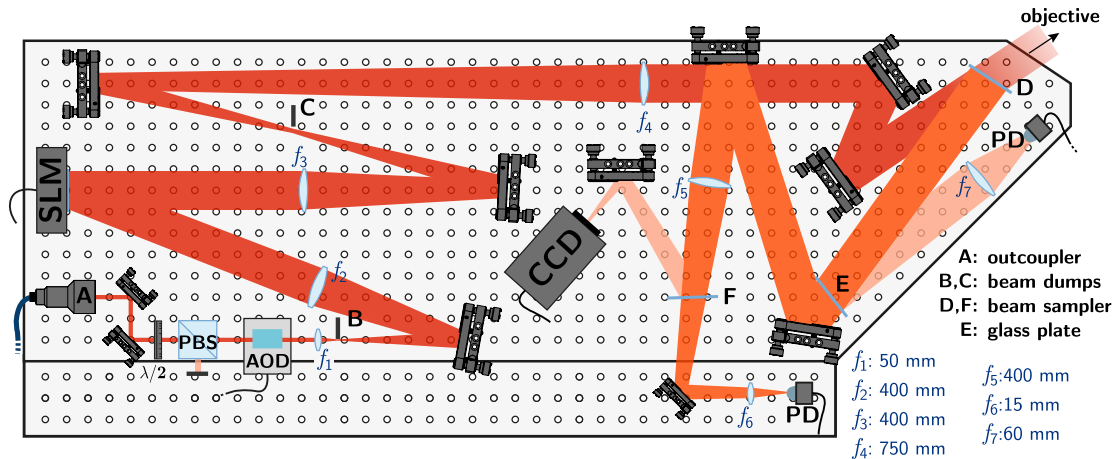


Figure 5.3.: The SLM board. Shown is the trapping beam coupled out (**A**) and polarized before it reaches the SLM. It is subsequently guided to the objective via a 4f-setup. Photo diodes and CCD camera serve for feedback purposes. Adapted from [Hol17].

beam-splitter (PBS) to obtain linearly polarized light. The polarization is crucial when it comes up to the diffraction efficiency of the SLM (defined by the light level diffracted into the first order divided by the zeroth order) because, as explained in the previous chapter, only light polarized in parallel to the untilted molecules gathers a spatially dependent phase.

In the next step the light passes a acousto-optic deflector (AOD). This device is used for spatial beam steering. By varying the frequency applied to the AOD the diffraction angle can be manipulated. With a reaction time of about 300 ns one can move the light pattern in the atoms' plane much faster with the AOD than with the SLM. The latter is limited by a refresh rate of only 120 Hz. Additionally, it is possible to apply a signal containing two different frequencies to the AOD. In this case two incident beams hit the SLM-chip under slightly different angles and therefore two copies of the same intensity pattern in the Fourier plane are produced. For instance, one possibility is to prepare the atoms in a lattice created by the SLM and adiabatically load it into a superlattice by turning on a second frequency with the AOD (see also chapter 7). The centre frequency of the AOD is around 80 MHz.

After the AOD the beam is passing a telescope (f_1 , f_2). It is eight times magnified such that the beam illuminates the whole SLM-chip. At the focus of the first lens (f_1) we cut the zeroth order of the AOD with a beam dump to which a razor blade is attached (**B**). The SLM is illuminated under an angle of about 20° because otherwise the light utilization efficiency is considerably reduced.

In the following the beam passes a 6f-setup (f_3 , f_4 and the objective) until it reaches the atoms' plane. Although this makes the beam path long and thus increases the probability of noise onto the beam there are two benefits. One advantage is that the zeroth order of the SLM can be cut at the focus of f_3 (**C**). The other more important aspect is that we want to use the full numerical aperture of the objective to obtain the smallest possible spot size which is only possible if the aperture of the objective limits the beam size. Only then maximal resolution can be obtained with the objective. The additional telescope between SLM and objective yields a magnification of about 1.9. Before the beam reaches the objective we added a beam sampler (**D**) to the beam path that transmits most of the light to the objective. The remaining part is reflected and is used for diagnostic and feedback purposes. The diagnostic tools are a CCD camera and two photodiodes (PDs)—one PD for small targets, such as few discrete lattice points that require a power in the milliwatt regime and one for continuous targets with powers of about a few hundred milliwatts. A small part of the reflected light is split up with a glass plate (**E**) and focused down (f_6) onto a InGaAs photodiode by Thorlabs (PDA10CS-EC). This photodiode is meant for use at high powers. The main part of the beam is focused down (f_5) and subsequently split up into two parts with another beam sampler (**F**). The transmitted part of the beam is further focused down (f_6) onto an InGaAs photodiode that is home made by the institute's electronic workshop. It is meant to be used for low powers. The few percent of the beam that are reflected by the beam sampler are incident on a CCD camera. The image of the intensity pattern on the CCD camera compared to the pattern in the atoms' plane is magnified by about a factor of 20 ($f_5 \approx 20f_{objective}$). The PDs in combination with the AOM mentioned above are used to regulate the total beam power with a PID feedback loop to keep the depth of the trapping potentials constant. Former measurements within our group already revealed intensity fluctuations of 480 Hz due to the refreshing of the SLM [Cla16]. As the tests showed that single spots of a phase pattern were fluctuating in phase with each other it is possible to compensate for this effect at least to first order by regulating the overall light intensity.

The camera is used for diagnostic and feedback purposes. Similar setups showed that a closed-loop optimization is essential to take care of imperfections in the real setup and thus improve the matching of theoretical distribution and real light distribution in the atoms' plane [Bru11; Gau12; Nog14].

In the future we aim to use dynamic trapping potentials. As stated in this paragraph it is straight forward to generate time-dependent potentials with the AOD. However, the possibilities provided by the AOD are limited. Yet, the realization of time-dependent potentials with the SLM is challenging for several reasons. One

5. Experimental Extension

would need to prepare a video composed of single images of the changing potential. To process such a movie in real time is hard because of the amount of data. There are two options how to proceed: Either one aims for a frame rate with less frames per second (fps) than the refresh rate, e.g. 40 fps, such that one can make sure that the SLM displays every single image or one goes for a higher frame rate, e.g. 240 fps, with deviations smaller than a focal unit between two sequent frames. This means that it is not essential to display every single image on the SLM. Provided one of these two procedures the time-dependent potentials would nevertheless only be suitable for atom preparation or to separate traps before readout, i.e. when precise timing of the movement relative to the complete sequence is not essential. Manipulating the atoms to observe fast dynamics requires a sufficient precision of the trigger (about 1 ms). This is so far out of reach for dynamics with the SLM due to its refresh rate of 8 ms which is also not synced to the experiment. Therefore, it is difficult to obtain reproducible timings.

The long beam path and the huge beam diameter make the beam susceptible to drifts caused by airflows and temperature gradients. To reduce these effects we added several tubes into the beam path and designed a cover that shields the system from the top. Additionally, it protects the optics from dust.

5.2.2. Optical Setup of the Objective and for Imaging

In the following paragraph the breadboard hosting the imaging optics and the breadboard installed vertically above the vacuum chamber, to which the high resolution objective is attached, are described. The latter breadboard is designed to meet the requirement of combining imaging light, SLM trapping beam and the vertical MOT beams.

After the trapping light (red beam in figure 5.4) leaves the SLM-breadboard it is directed onto the objective with the help of three mirrors. As access to the objective is required for several purposes the last mirror (**A**) is chosen to be dichroic—it is high reflective for light of 1064 nm wavelength which is used for trapping atoms and highly transmittive for resonant light ($\lambda = 671$ nm) used for imaging and the MOT beams. The objective then focuses down the trapping light onto the atoms' plane at a distance of 23 mm. A polarizing two inch cube on the vertical breadboard allows to combine/separate the MOT beam and the imaging beam on the vertical breadboard. In consequence of the implementation of the objective it was necessary to change the setup of the vertical MOT beams. The vertical MOT beam is now coupled out below the vacuum chamber and is retroreflected above the vacuum chamber after being reflected by the polarizing cube (figure 5.5 a)). Above (below) the upper (lower) $\lambda/4$ waveplate the imaging

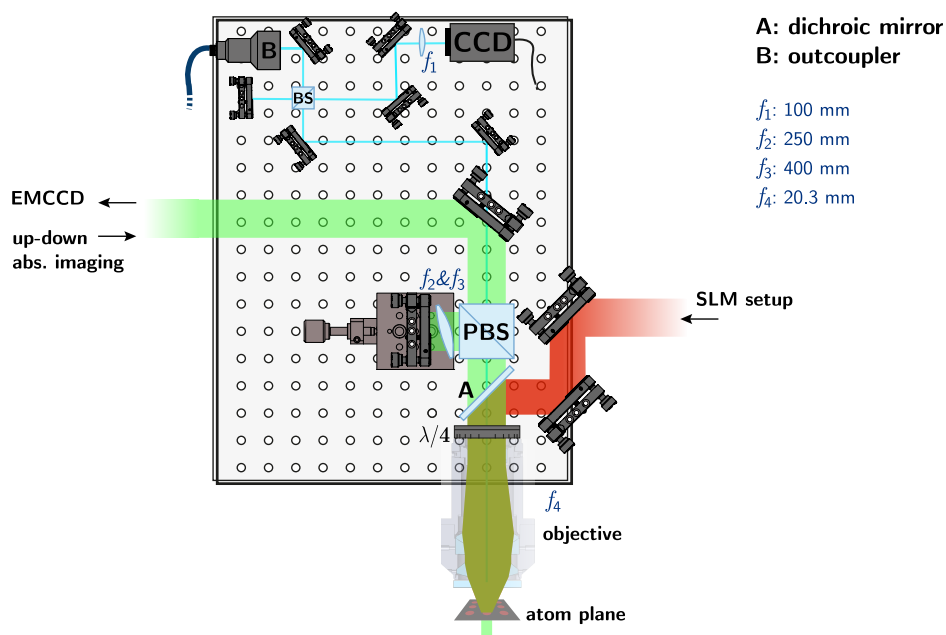


Figure 5.4.: Vertical breadboard positioned above the vacuum chamber. Light prepared at the SLM breadboard for trapping (red beam) is focused on the atoms' plane with the objective. Due to the use of a dichroic mirror (highly transmittive for $\lambda = 671 \text{ nm}$ and highly reflective for $\lambda = 1064 \text{ nm}$) access to the vacuum chamber is also guaranteed for the MOT beams (green) and the imaging beams (green). A PBS separates/combines the paths of the imaging light and the MOT beam. The MOT beam coming from below the vacuum chamber is reflected to the left by the PBS and subsequently retroreflected. Imaging light passes the cube without being reflected. The propagation direction of the imaging light depends on the imaging technique and the choice of the camera. A beam used to align the objective is sketched in turquoise (for details see section 5.3 and appendix D). Adapted from [Hol17].

beams have a linear polarization perpendicular to the MOT beam such that the imaging light passes straight through the cube.

So far absorption imaging of the experiment was possible for two axes from the side and from top-down. Additionally, fluorescence imaging from the side was provided for diagnostic purposes. The implementation of the objective left the imaging possibilities from the side unchanged but affected the vertical axis. We were able to retain the top-down imaging, which has a low resolution but a large field of view, by coupling out the light for the absorption imaging on a separate breadboard (position **A** in figure 5.6). The beam is magnified twice before it reaches the atoms as the objective needs to be taken into account (by

5. Experimental Extension

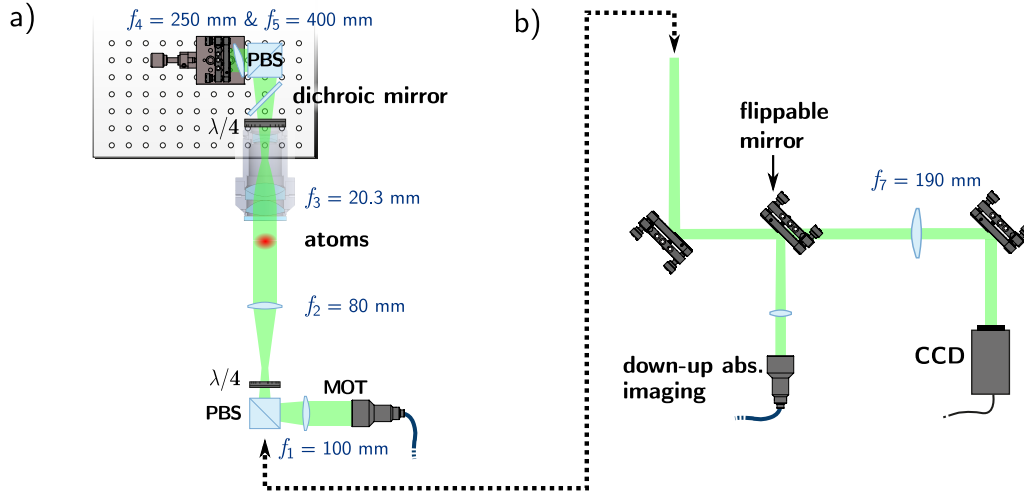


Figure 5.5.: a) With the extension the vertical MOT beam is coupled out from below the vacuum chamber with a $f = 50$ mm lens. A 4f-setup (f_1, f_2) is added between the outcoupler and the atoms. Behind the atoms the beam passes the objective (f_3) and a further combination of two lenses (f_4, f_5) before it is reflected back. By combining these three lenses (f_3, f_4, f_5) the size of the reflected beam is adapted to the incoming beam. A $\lambda/4$ waveplate below and above the vacuum chamber provide the circular polarization required for the MOT beams. The two polarizing beam splitters are used to make sure that the MOT beam as well as the imaging beams pass the atoms but that only the MOT beam is reflected back. b) Optics for absorption imaging are partly placed below the vacuum chamber. For down-up imaging the light is coupled out below the chamber, the flippable mirror is swung in and the EMCCD (figure 5.6) is used for detection. If the flippable mirror is swung out absorption imaging from top-down is possible. Lenses f_2, f_7 are used to image the atoms with a magnification of $M \approx 2.14$ on a CCD camera.

$M \approx 41$ with f_1, f_2 and by $M \approx 0.05$ with f_3 and the objective). The CCD camera for detection is placed below the vacuum chamber (figure 5.5 b)). Very importantly, we increase our imaging possibilities by the implementation of an electron multiplying CCD (EMCCD) camera which is also placed on the imaging board (figure 5.6). It can either be used for imaging single atoms by collecting their fluorescence or for absorption imaging where the beam is coupled out below the vacuum chamber (figure 5.5 b)). The latter imaging option provides a smaller field of view but a higher resolution than the absorption imaging from top-down described above. Depending on whether one wants to image a small cloud of atoms or atoms in a single well with the EMCCD either lens f_4 or f_5 needs to be flipped out.

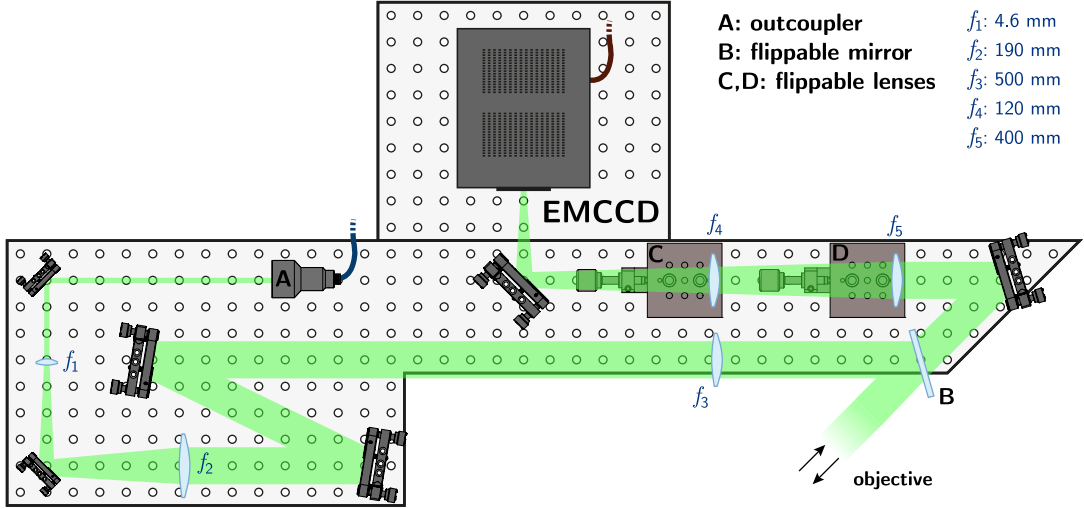


Figure 5.6.: Imaging breadboard. The beam coupled out at position **A** is used for absorption imaging from top to down. The newly implemented EMCCD camera allows high resolution absorption imaging from down-up or fluorescence imaging with single particle sensitivity. Adapted from [Hol17].

The new EMCCD camera allows to perform fluorescence imaging with single-atom resolution. Adapting the imaging technique developed in our groups second experiment the atoms can be imaged without any additional cooling scheme such that spin-resolution of the atoms can be maintained [Ber18b]. This imaging approach is described in detail in section 5.5.

To complete the usability of the extension a few further add-ons were needed. A new MOSFET bank and a new power supply were implemented in order to switch the direction of the current in the Feshbach coils. The option to invert the magnetic field is needed to drive the D2 transition for absorption imaging as imaging beams from top to down and down to top have opposite polarization in the atoms' frame. Additionally, this enables us to apply a magnetic field gradient and an offset field at the same time.

We also put the experiment's oven shutter into operation (figure 5.7). Previously, we did not need the oven shutter as only experiments with several thousand atoms were performed. However, for the preparation of single atoms it is essential to block the beam of atoms during the experimental sequence and the detection. The shutter, which is connected to a rotary motion vacuum feedthrough (670000-RotaryMotionFT, 1.33"Flg by MDC), was implemented in the experiment together with the vacuum chamber [Rie10]. Having coupled the feedthrough to a stepper motor which is controlled by an Arduino the position of the shutter can be changed during the experimental sequence.

5. Experimental Extension

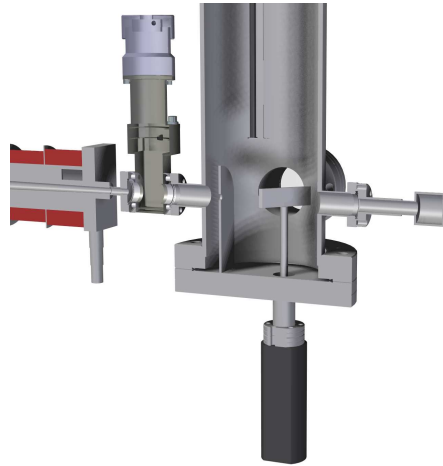


Figure 5.7.: The oven shutter (centre) can be used to block the beam of atoms coming from the oven (right) to enter the Zeeman slower (left, red). Adapted from [Rie10].

At the end of this section we present a photograph (figure 5.8) of the current status of the experimental setup.

5.3. Implementation

The challenge in the design of the optical setup was to meet the requirements imposed by the optics around the SLM, the EMCCD camera and the objective while taking into account the restrictions conditioned by the existing setup. The whole extensional setup was assembled in a test lab. In the final stage of the preparations all three additional breadboards were set up and arranged in a configuration identical to the one in the real setup. Different tests, including first checks of the wavefront errors, the examination of the resolution and the acceptability of the light pattern in the atoms' plane, were carried out in this environment. We mention shortly that the objective was cleaned thoroughly after these tests just before its implementation in the real experiment which increased its performance².

The test setup was also essential in order to determine how to align the objective with respect to the vacuum window. That the alignment critically influences the performance of the objective—such as the size of the focus—was shown in previous tests [Ber13]. Importantly, the position of the objective needs to be adjusted with

²That the cleaning had an impact was observed with the up-down (absorption) imaging beam. It was of very bad quality in the test lab but turned out to work reasonably good in the actual setup.

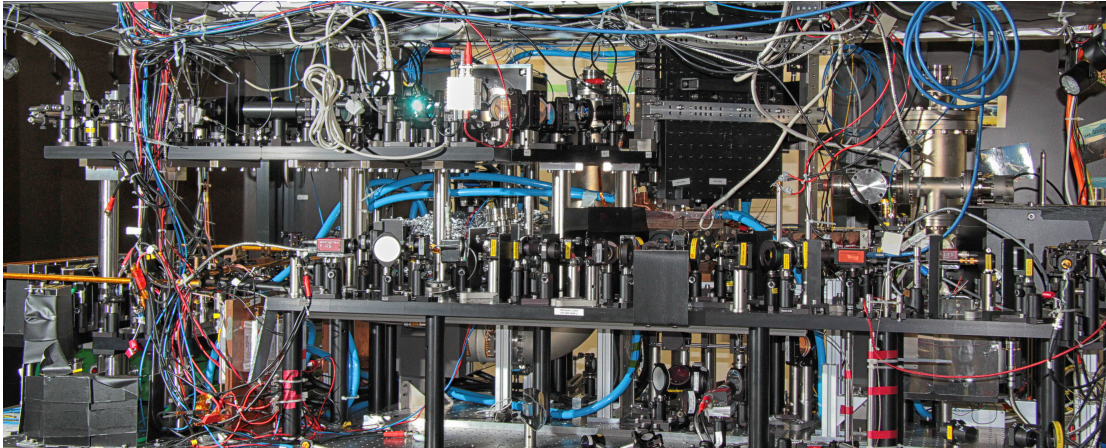


Figure 5.8.: Experimental setup including the extension: The top layer on the left hand side is the SLM breadboard. On its right side the vertical breadboard (black), which is hooked up above the vacuum chamber, can be identified from the rear view. The imaging breadboard is not visible here as it is covered by the SLM breadboard.

respect to the optical axis of its lens system which is not coinciding with the axis of its tubing. Once the objective is put into the experiment it is almost impossible to figure out the optical axis because the vacuum chamber restricts the access to the focal plane of the objective. A more comfortable way is to work in a test setup and establish an alignment procedure for a passive alignment to a reference that one can follow once the objective is integrated in the real setup. In the test setup we can simply mimic the vacuum window with a glass window of identical specifications and thus retain good access to the focal plane. The required tilt of the objective can be determined with the help of a gold grating placed in the focus. It is illuminated and after the light passes the objective we focus it down to a CCD camera with a $f = 750$ mm lens. The recorded diffraction pattern allows to draw conclusions whether the gold grating is placed exactly in the focal plane. Once this position is found, the aberrations of the pattern are minimized by adjusting the angle of the objective. This is possible as the objective is fixed to the vertical breadboard with a mount which provides the required degrees of freedom (Newport Lens Positioner LP-2A). Besides the option to adjust the tilt around the x - and y -axis, it also allows for translations in x -, y - and z -direction. We obtain a tilt of the tubing with respect to the the optical axis of 4 mrad in x -direction, and 12 mrad in y -direction. The optimal angle of the objective's tubing can be recorded with the help of an alignment beam. The vacuum window or the fake vacuum window serve as a reference for the angle, respectively. The alignment protocol is presented in detail in appendix D.

5. Experimental Extension

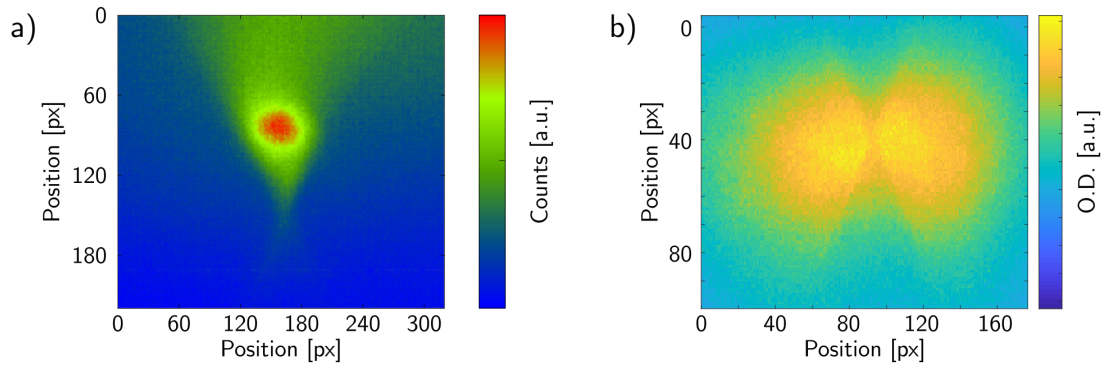


Figure 5.9.: Finding the focus. a) By directing a focused resonant beam onto the atoms captured by a compressed MOT we were able to detect enhanced scattering at the focus with fluorescence imaging from the side. b) Due to the high scattering rate atoms are removed from the MOT. We see the depletion at the focus when imaging with absorption imaging from the side.

The extension integrated into the experiment iteratively checking always the functionality of the experiment. The first step was to invert the beam of the vertical MOT axis within the existing setup such that the beam is coupled out from below and reflected back from above the chamber (for the optical setup of the MOT and the two absorption imaging setups from below the vacuum chamber see figure 5.5 a) and b)).

Next, we moved the SLM breadboard attached to two long posts was placed it above the vacuum chamber (figure 5.2). Before putting in the objective we made sure that the MOT was still working. Fitting in the objective and finding its focus turned out to be challenging as outer diameter of the objective’s tubing and inner diameter of the re-entrant viewport only differ by 1.7 mm (the objective was not designed in the first place for this experiment). Eventually, it was successful to first countersink the objective as much as possible into the re-entrant viewport and subsequently fix its mount to the vertical breadboard. Afterwards it was tilted to the required position as described in appendix D.

To find the focus we worked with a cloud of atoms captured in a compressed MOT. Installing the imaging breadboard and removing lens f_3 in (figure 5.6) we were able to work with ad focused beam roughly resonant to the D2 transition of ${}^6\text{Li}$ at an intensity about 10^6 times higher than the saturation intensity. Once the beam hit the atoms this caused a high scattering rate at the focus which we were able to observe with fluorescence imaging from the side (figure 5.9 a)). Due to the enhanced scattering at the focus and the associated momentum kicks atoms can be blown out from the trap with this technique. Therefore, we were also

able to detect the focus with absorption imaging from the side from two different axis (figure 5.9 b)). Being able to image the focus from three different horizontal directions we were able to move it to the position of the magnetic saddle in the centre of the trap using the translational degrees of freedom of the Newport Lens Positioner. After these preparations, finally, we were able to switch to the infrared light from the SLM setup. When applying no phase pattern to the SLM together with the objective we obtain a tightly focused optical tweezer. Due to its small waist we refer to it as microtrap. With the objective being aligned along the horizontal axes we could load the microtrap from the ODT. By reinstalling lens f_3 in figure 5.6 we retained the up-down imaging as used before.

To conclude we were able to implement the extensional setup as planned. For future experiments we recommend to consider critical dimensions carefully and to try to work with absolute references when it comes up to the implementation of an objective, for instance by mounting the objective directly to the vacuum chamber. As a result the implementation of the objective would be highly facilitated and roughly reproducible. This would be helpful for an objective that needs to be aligned with the precision on the order of a micron. In our case this is not given for which reason it was difficult to implement and align the objective. Whenever we take out and in the objective in future we need to redo the whole alignment procedure. In our experiment the vertical breadboard and the SLM breadboard are coupled. It is not yet proved whether the coupling enhances or diminishes the stability of the setup.

5.4. A High-Resolution Objective

A crucial part of the extension to our setup is the implementation of an objective that has a very small waist of the focus which allows to trap atoms in effectively one dimensional traps. Combined with the SLM it can be used to engineer potential structures of micrometer precision. A wide angle of aperture is also important to obtain a high photon collection efficiency required for diffraction-limited high-resolution imaging.

So far, our experiment was not reliant on a high resolution objective because experiments were performed with an atomic two-dimensional cloud of about 35,000 atoms. As the size of the 2D cloud in the standing wave trap is about 200 μm an objective was neither for trapping nor for detection a crucial component. With the ambition to trap and image single atoms an objective is needed. The one we implemented recently in our experiment was designed within the course of the thesis of [Ser11b] and an identical version of the objective is in use in the Jochim

5. Experimental Extension

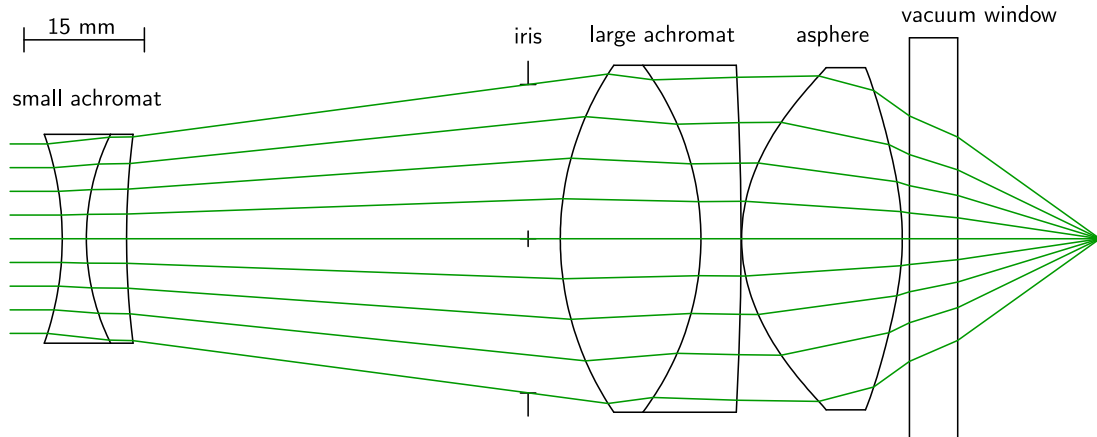


Figure 5.10.: The design of the high resolution objective. It corrects for the 6 mm thick vacuum window. The beam is focused with the large asphere that also reduces spherical aberrations. The large achromat takes care of chromatic aberrations of the two employed wavelengths, the smaller achromat is added to the design to optimize the numerical aperture of the beam. Adapted from [Ser11b].

group’s few-fermion experiment since 2013 [Ber13]. In the few-fermion experiment the preparation in the ground state of a double-well could be achieved with a fidelity of over 90% [Mur15a]. They also showed that the high photon collection efficiency of about 10% enables imaging of single atoms in free space [Ber18b].

The custom made re-entrant viewports of the lower and upper vacuum window were chosen to have a high numerical aperture (NA) such that when adding an objective outside of the chamber the imaging is not limited by the vacuum window. The design of the objective takes care of the 6 mm thick fused silica window and corrects for it. When being aligned in parallel to the objective the distance between vacuum window and objective is variable (as long as the window is closer than the focus) because the window only induces a beam displacement. Therefore, it is not critical that the vacuum window is further apart from the objective in our experiment than in the other experiment of our group. Besides the constraint imposed by the vacuum window, the design of the objective was determined by the quest for a small focus, the requirement to correct for chromatic aberrations of two wavelengths (1064 nm trapping light and 671 nm imaging light) as well as by the need of a high NA. A schematic picture of the objective is given in figure 5.10. The large aspheric lens focuses the beam. It reduces spherical aberrations and provides diffraction limited performance, the large achromat corrects aberrations for the two different wavelengths we use in the experiment ($\lambda = 1064$ nm, $\lambda = 671$ nm). Additionally, a small achromat was added to the design to reduce the required beam size of the ingoing beam and increase the numerical aperture of the objective.

5.4. A High-Resolution Objective

wavelength	$\lambda = 1064 \text{ nm}$	$\lambda = 671 \text{ nm}$
focal length		20.3 mm
image distances		∞
diameter field of view		200 μm
max. diffraction limited NA		0.6
entrance aperture diameter at max. NA		24.4 mm
resolution	1.08 μm	0.68 μm
waist of focus	0.72 μm	0.45 μm

Table 5.1.: The nominal design parameters of the custom-designed objective. Adapted from [Ser11b].

An overview of the nominal design parameters of the objective can be found in table 5.1. Checks on the performance of the objective were done in the theses of [Kli12] and [Ber13] in a test setup where the vacuum window was mimicked by a test window of the same thickness and material. To test the resolution of the objective one can mimic a point source at the focus of the objective by illuminating a small hole. Therefore the condition $\sin(\theta_{1\text{st min}}) > \sin(\theta_{\text{aperture objective}})$ needs to hold. With a refractive index of one this yields

$$1.22 \frac{\lambda}{D} > \text{NA}. \quad (5.2)$$

First tests on the objective used in the few-fermion experiment were performed by [Kli12] with a pinhole of $D = 800 \text{ nm}$ diameter placed slightly out of focus such that a magnified image of the expected pattern could be detected behind the objective. Further tests with a gold grating were conducted by [Ber13]. The holes of the grating have a diameter of 650 nm and are separated by 20 μm . Placing the gold grating in the focal plane of the objective and shining light from behind onto it, the grating acts as the desired point source. In the image plane of a lens—in our case the objective—that cuts a part of the light one expects to see the pattern of an Airy disc. Using the Rayleigh criterion the resolution is defined as the distance from the central intensity maximum to the closest minimum reading

$$\rho = 1.22 \frac{\lambda}{2\text{NA}}. \quad (5.3)$$

Adding a further lens after the objective the image plane can be shifted from infinity into the focal plane of this lens where the light pattern can be detected with a camera. The two former tests showed significant deviations of the resolution from the nominal values. Before we moved the SLM from the SLM test setup to

5. Experimental Extension

wavelength	nominal values	measurements by [Ber13]		recent measurements
		x -profile	y -profile	
1064 nm	1.08 μm	(1.61 \pm 0.10) μm	(1.51 \pm 0.10) μm	
671 nm	0.68 μm	(1.51 \pm 0.10) μm	(1.21 \pm 0.10) μm	(861 \pm 8) nm

Table 5.2.: Comparison of nominal resolution with different measurement results. Our recent measurement is significantly closer to the theoretical design value.

our experiment, we performed another test with the gold grating as described above using imaging light (671 nm). We used a Thorlabs beam profiler (BC106-VIS) to image the light pattern in the focal plane of a $f = 750$ mm lens which was placed behind the objective. From the image the resolution was determined by fitting the expected diffraction pattern

$$I(x, y) = I_0 \frac{2J_1\left(\frac{1.22\pi}{\rho}\sqrt{(x-x_0)^2+(y-y_0)^2}\right)}{\frac{1.22\pi}{\rho}\sqrt{(x-x_0)^2+(y-y_0)^2}} + I_{noise}. \quad (5.4)$$

Here J_1 denotes the Bessel function of the first kind. The fitting parameters I_0 , x_0 , y_0 , I_{noise} and ρ denote the peak intensity, the shift along x - and y -direction of the pattern, the background noise and the resolution. A single image of the camera captures the diffraction patterns of several holes of the grating. After applying a 2D fit to each spot we can therefore, in the end, take the average value of all fit results³. For this procedure the error is determined by the standard deviation of the mean. Length scales in the image can be determined very precisely as the inter-spot distance of the grating is known. The result we yield with this 2D fit are significantly closer to the nominal values than those of previous measurements (figure 5.11). In general, deviations from the nominal values can be caused by an imperfect alignment of the optics or because the objective itself is not perfectly assembled. Thus our improved results could be due to a better alignment or a better fitting procedure. A comparison of the obtained resolutions for the objective used in our experiment is given in table 5.2. In [Ber13] and [Kli12] further tests were performed on the wavefront error with an Michelson interferometer and on the focus of the trap by detecting a 40 times magnified image of it [Ber13]. The interference measurement showed that wavefront errors due to the objective are smaller than $\lambda/4$. The size of the focus depends on the wavelength, the NA, the illumination (in our case a Gaussian intensity distribution) and if the beam is

³For the result presented here, three different images with in total 15 diffraction patterns were analysed.

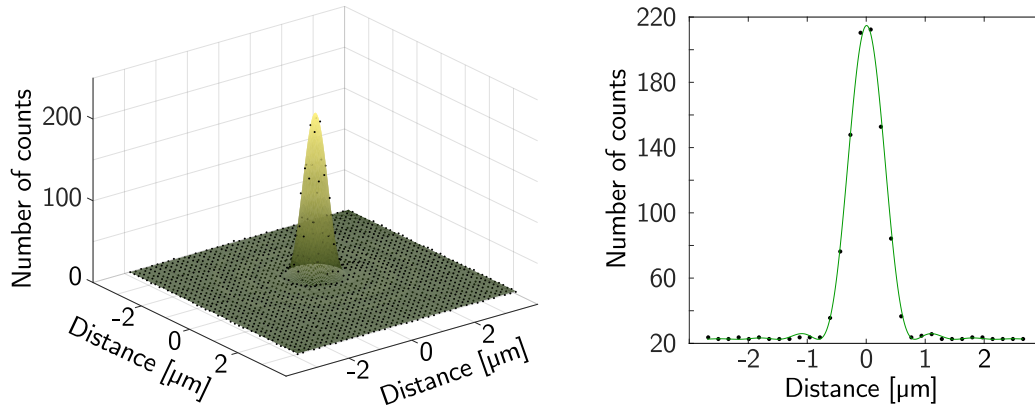


Figure 5.11.: Point-spread function measured in the SLM test-setup. The right panel shows a cut through the centre.

clipped by an aperture on its radius. Measurements performed in [Ber13] showed deviations of the size of the focus by more than 15% from its theoretical value. In the SLM test setup we checked that the beam looks acceptable in the focus by implementing a raspberry pi camera on a motorized stage (Sony IMX219PQ). However, it was not possible to resolve the size of the focus of the SLM as the camera has a pixel size of $1.1 \mu\text{m}$. In general, it is advantageous to work with a small focus because this makes the separation of the trap levels larger and therefore the preparation of a well-defined number of atoms becomes easier.

5.5. Single Atom Detection

Since we will work with small atom numbers in future detection schemes that allow to measure single atoms are crucial. In our setup we plan to use two different techniques. One of the techniques is based on recapturing the atoms in the MOT and collecting part of their fluorescence with a CCD camera placed in the horizontal axis. About 2.5×10^5 counts are detected per atom for an exposure time of 500 ms. As shown by first experimental results this technique allows to determine the number of atoms for small samples with over 99% fidelity (for details see section 6.2). However, spin and spatial information of the atoms are lost during imaging. The second imaging technique addresses this issue. By using the high NA objective in combination with the new EMCCD camera we want to detect single atoms in free space in future. Pulsing individual atoms for an exposure time

5. Experimental Extension

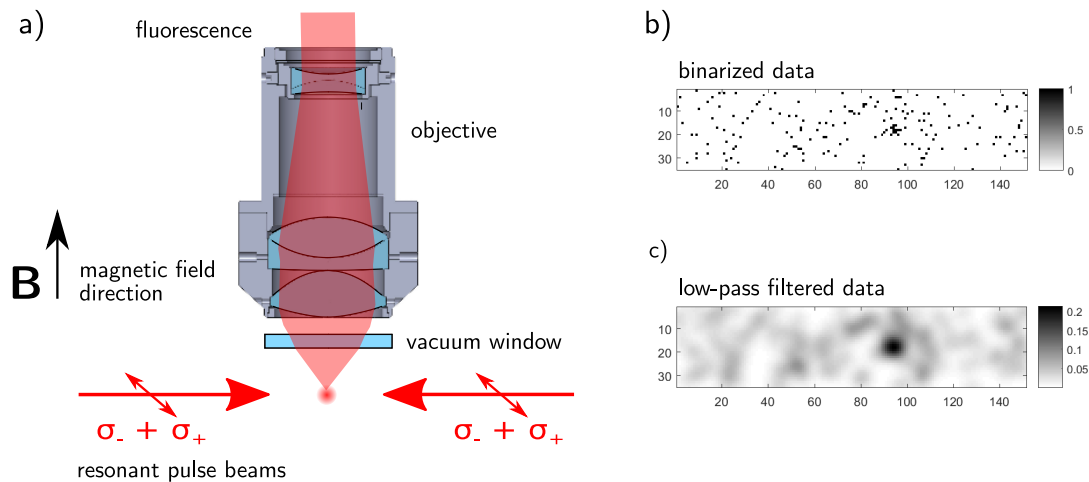


Figure 5.12.: Single-atom detection. a) Two counter-propagating beams pulse the atoms from the side. A part of the fluorescence is collected with the high NA objective. b) Binarizing the data removes readout noise (data taken from few-fermion experiment). c) Single atoms can be identified by applying a low-pass filter. Adapted from [Ber17].

of 20 ms with resonant light the detection of as few as 20 photons is sufficient to identify an atom with very high probability. We want to adapt this imaging scheme from our group’s second experiment, where it was recently developed. Based on [Ber17; Ber18b] the technique will be discussed in this section. In principle both imaging techniques mentioned here can be applied one after another for the same run starting with the free space imaging. Complementary to the possibility to resolve the atoms in free space the MOT-imaging can serve as a cross-check on the total atom number.

A central element for the free space imaging is the new electron multiplying charge-coupled device (EMCCD) from Nüvü (model HNü 512) which is ready to be taken into operation. An EMCCD camera works with an ordinary CCD chip that exploits the photo-electric effect. Additionally, in an EMCCD camera the photoelectrons are passing a multiplication register that launches an avalanche of several hundred secondary electrons before the charges are converted into a voltage. In the photon counting mode EMCCD cameras are well suited to work at low light levels due to their high quantum efficiency (around 90% for the model we use) and their low dark current. The main source of noise are clock-induced charges (CICs) which originate from the high shifting frequencies of the photoelectrons. In [Hol17] it was examined that an optimum point exists for the operation at a detection efficiency of 78% and a CIC count of 0.002 per pixel.

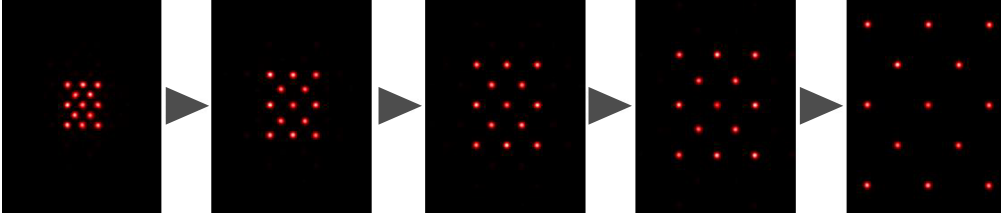


Figure 5.13.: Separating the lattice spacing for in-situ imaging. As the atoms perform a random walk during the imaging process they need to be well separated before the imaging process in order to distinguish them. We plan to use the SLM for increasing the lattice spacing before imaging.

Quantum gas microscopes are commonly used devices to resolve single lattice sites [Nel07; Kar09; Bak09; She10; Che15; Hal15; Par15; Omr15; Edg15; Mir15; Yam16]. However, they rely on sophisticated cooling schemes during the imaging process to prevent atoms heated up from several thousand scattering processes to leave the trap. As a consequence spin information is lost during the imaging process. We want to take another approach that does not require additional cooling techniques because we only image for a short time.

Working in the Paschen-Back regime at over 300 G allows to differentiate the hyperfine states that are separated by about 80 MHz for large fields. Two opposing beams vertical to the quantization axis are flashing the atom(s) alternately with a pulse duration of 200 ns (figure 5.12 a)). The beams are polarized linearly perpendicular to the magnetic field. The beam power needs to be chosen such that the scattering rate is high but the power broadening is far from being on the order of the splitting of the hyperfine states. As for the imaging technique presented here the atoms are not pinned, they perform a random walk during the exposure time. Both alternating pulses and a high scattering rate and therefore the possibility of short exposure times are important to keep the random walk of the atoms as minimal as possible. In our group's few-fermion experiment the parameters are chosen such that each individual atom experiences a few hundred scattering events for an exposure time of 20 ms. They can determine an atom's position up to a precision of about $4\ \mu\text{m}$ and distinguish between two atoms with a 90% probability if they are separated further than $32\ \mu\text{m}$. In our experiment we plan to use the SLM to increase the lattice constant before imaging in in-situ in order to increase the resolution (figure 5.13). Working with a confining harmonic potential and letting the atoms expand for a quarter of a trap period it is also possible to obtain the particles momentum distribution (see section 4.2). This is a clear advantage of the free space imaging technique over a quantum microscope.

The high NA objective allows to collect approximately 10% of the fluorescence signal. To reach a detection fidelity of over 99% it is enough to detect about 20

5. Experimental Extension

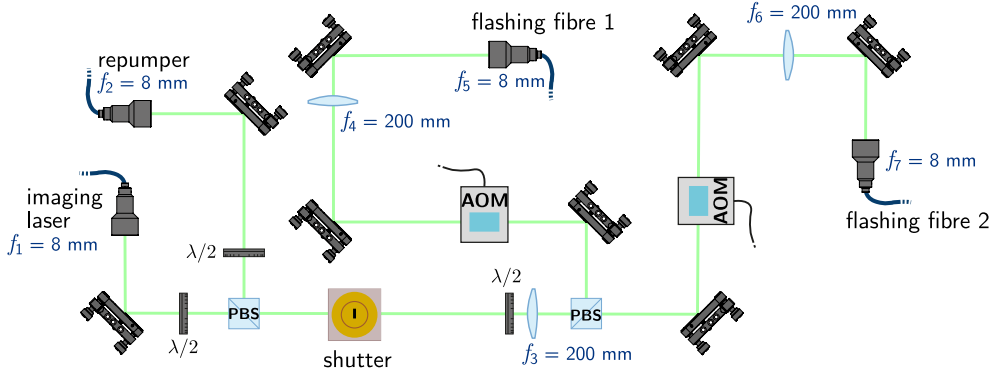


Figure 5.14.: Preparation of light for imaging the atoms. Two transitions need to be addressed (repumper and imaging laser). Their beams are overlapped and subsequently divided into two for the probe beams from different sides. AOMs allow to flash alternately.

photons. In the next step the data is binarized to remove readout noise (figure 5.12 b)). As the signal still suffers from CICs it is required to additionally apply a Gaussian low-pass filter (figure 5.12 c)). Then, local maxima with high amplitude can be identified with atoms; small amplitudes belong to CICs. In our experiment it is probably possible to work with fewer scattering events because our EMCCD camera has a lower CIC occurrence than the one used in the other experiment.

For imaging we drive the D2 transition of ${}^6\text{Li}$ (see section 4.1). Preparing the atoms in the lowest three hyperfine states one can drive a closed or almost closed σ_- -transition transition from $m_j = -1/2$ to $m_j = -3/2$. The σ_+ -transition is detuned by over 1.1 GHz at 300 G and therefore strongly suppressed. For atoms in state $|3\rangle = |m_j = -1/2, m_I = -1\rangle$ the transition is closed. However, state $|1\rangle$ and $|2\rangle$ contain small admixtures from the $m_j = 1/2$ manifold because I and j are only completely decoupled in the limit of an infinite magnetic field. When their excited states in the $m_j = 3/2$ manifold decay they have a probability on the order of a permille (for the range of the magnetic field we work with) to decay into the $m_j = 1/2$ manifold [Bec16]. To prevent dark states one can use an additional laser that drives a σ_+ -transition from $m_j = 1/2$ to $m_j = 3/2$. One can distinguish between the three lowest hyperfine states that are associated with different spin species in the same measurement by driving their individual D2 transitions one by one.

We prepare the light for the resonant pulses on a separate breadboard (figure 5.14). As explained above besides the imaging laser for the σ_- -transition from $m_j = -1/2$ to $m_j = -3/2$ imaging of states $|1\rangle$ and $|2\rangle$ requires a repumper for the σ_+ -transition from $m_j = 1/2$ to $m_j = 3/2$. Both beams are overlapped and then split to provide light for the two opposing flashing beams.

6. First Experimental Results

Having completed the implementation of the extensional setup the first step has been the optimisation and characterisation of the simplest system we can create with the new setup—a single microtrap. The microtrap is the basic building block for any mesoscopic system of discrete sites that we want to realize with the SLM. This section describes how we deterministically load and probe atoms in the microtrap.

6.1. Loading the Microtrap and Preparing Single Atoms

To put the new setup into operation our first step has been to work with a single microtrap which is created by a tightly focused far red-detuned laser beam. The SLM is not needed to create such a trap but we apply a phase pattern to it that corrects for aberrations of the objective and the lens system. For the preparation of atoms in the microtrap the first cooling stages described in chapter 4 are adapted. There exist different possible stages from which the microtrap can be loaded in the experiment. One option is to load the microtrap from the optical dipole trap at the end of the first evaporative cooling stage (section 2.1). In the past, the experiments on the 2D setup have usually been performed in a regime where the particles form bound states for all values of the particle interaction (attractive branch). This regime offers a variety of intriguing phenomena to study, for instance, the BEC-BCS crossover in two dimensions [Rie15; Mur15c; Boe16]. To prepare the atoms in the attractive branch the evaporation and the loading into the 2D trap were performed at positive scattering lengths close to the Feshbach resonance where molecules are formed during evaporation. With the extension, however, we want to realize experiments with free fermions—for example to investigate the Hubbard model. In this case it is still advantageous to start the evaporation process in the ODT at large positive scattering length close to the Feshbach resonance because the high collision rate in this regime leads to fast thermalisation. However, it is important to ramp to small positive scattering lengths before molecules start to form.

6. First Experimental Results

Another possibility, with the advantage of significantly shorter experimental cycling times, is to load a non-degenerate gas from the ODT into the microtrap (i.e. no or little evaporation in the ODT) and to cool the atoms evaporatively in the microtrap itself. This is very efficient because the large density in the microtrap leads to short thermalisation times. To transfer the atoms into the microtrap the power of the ODT is reduced from 200 W to 37 W and the microtrap is ramped within 200 ms to a final power of 33.8 mW at a magnetic field of 300 G. After the sample thermalized the attractively interacting atoms can be cooled evaporatively (for the working principle of evaporative cooling section 2.1) in the microtrap within 10 ms. To this end, the ODT is switched off and a magnetic field gradient B' created by the MOT coils is ramped up to $B' = 59 \text{ G/cm}$ within 100 ms. The interaction between the magnetic field gradient and the magnetic moment of the atoms leads to a superposition of the microtrap with a linear potential and therefore to an asymmetric potential $V(z)$ of the form

$$V(z) = V_{\text{optical}}(z) + V_{\text{magnetic}}(z) = V_0 \left(1 + \left(\frac{z}{z_R} \right)^2 \right) + \mu B', \quad (6.1)$$

with z_R being the Rayleigh length and V_0 the depth of the microtrap. The asymmetric shape of the potential is similar to the shape of the potential shown in figure 6.1 b). Additionally to the linear gradient, the barrier height is reduced during evaporation by decreasing the power of the trapping beam to 1.5% of its initial value. With this cooling process one ends up with a sample of 200 fermions where the lowest trap levels are completely filled with a probability close to unity. Due to the Pauli principle and since we work with two hyperfine states each of the trap levels is occupied with two fermions. After the evaporation is finished the magnetic field gradient is ramped back off and the original depth of the microtrap is restored.

Small samples of even atom number can in the final stage of the preparation be prepared deterministically by spilling fermions from the microtrap (figure 6.1). This part of the experimental sequence has similarities with the evaporative cooling sequence. However, the crucial difference is that during the spilling process we work with non-interacting atoms at $B = 527 \text{ G}$ and therefore no scattering and rethermalisation processes take place as it is the case for the evaporation. As a result, only atoms in higher quantum states are getting unbound when the potential is tilted (figure 6.1 b)) and leave the trap while lower lying states are unaffected¹ To create an asymmetric potential the magnetic field gradient is ramped up to $B' = 23.7 \text{ G/cm}$ on a timescale of 80 ms. When the maximal gradient is reached

¹Note that this statement is only true if the timescale of the spilling is small compared to the timescale associated with the tunnelling through the barrier shown in figure 6.1 b).

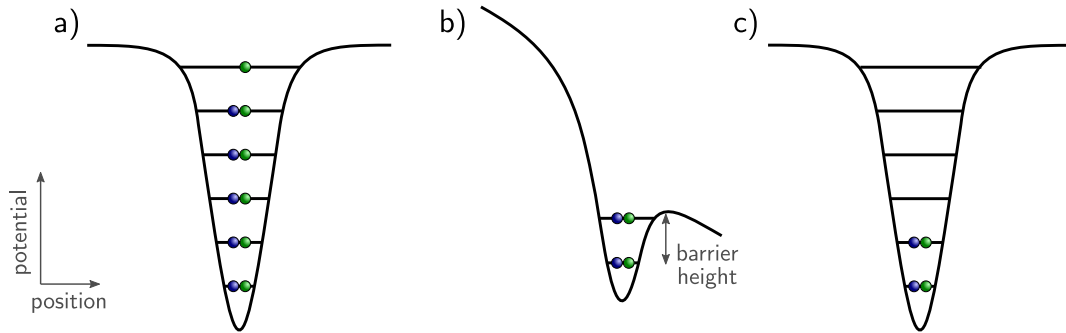


Figure 6.1.: Spilling scheme. a) Degenerate fermions in the tight microtrap. The lowest trap levels are fully occupied with an atom of each hyperfine state. b) Atoms in higher trap levels are removed by applying a magnetic field gradient and therefore creating an asymmetric potential. Fine-tuning of the atom number is reached by decreasing the potential barrier. c) After the spilling process the magnetic field gradient is removed again.

the power in the dimple is lowered to about $60 \mu\text{W}$ for 50 ms. Fine-tuning of the power can be used to control the barrier height and therefore the atom number in the microtrap deterministically (see figure 6.1 b)). Subsequently, the power and the magnetic field gradient are ramped to their initial values (figure 6.1 c)).

In general, it is also conceivable to load the microtrap directly from the MOT or from the 2D trap. At first attempts of the former option only the preparation of one or two atoms was possible. The problem might be that we are limited by light assisted collisions at high densities when resonant light is present.

6.2. Single Atom Detection with MOT Imaging

One possibility to detect single atoms with a fidelity over 99% is by recapturing the atoms in the compressed MOT section 4.2 and collecting a part of their fluorescence signal [Ser11a]. To create the compressed MOT we use the Feshbach coils in the anti-Helmholtz configuration to apply magnetic field gradient of roughly 260 G/cm in addition MOT beams of a $1/e^2$ -diameter of 11 mm that are red-detuned by about half a natural linewidth of the transition. The fluorescence of the captured atoms is collected on a CCD camera (Grasshopper3 GS3-U3-15S5M). In a first step, all the pixels in a region on the CCD chip where we find a significant fluorescence signal above the background noise are summed up. From the data a scaled background value is subtracted. The scaling is required because diffusive reflections of the resonant and unregulated MOT beams lead to a large fluctuation of the number of background counts. The background

6. First Experimental Results

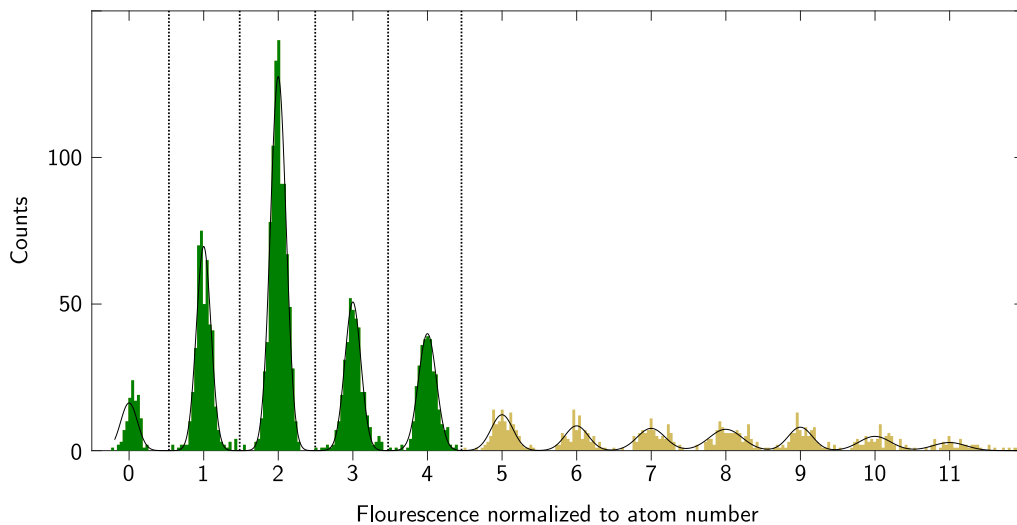


Figure 6.2.: Fluorescence signal normalized to atom number. For atom numbers from zero to eleven well separated peaks indicate a well-defined atom number. Due to low statistics the ochre region is not suitable to determine the detection fidelity. The green data is assigned to different atoms numbers by determining the crossing of the normalized Gaussian distributions of the peaks. They are indicated with dotted lines. This leads to a detection fidelity of over 99.99%.

image is obtained by taking the mean of a set of five background images under the same conditions as the actual data, the only difference being that no atoms are recaptured in the MOT. To determine a base value of the background we sum over the region of interest defined beforehand. The next step is to scale the base value. To this end a frame around the region of interest is chosen. The scaling factor is given by the ratio of the number of counts within this frame of the actual data and the number of counts within the same region of the background image. When choosing an exposure time of 500 ms, which is significantly shorter than the $1/e$ -lifetime of (11.6 ± 0.4) s of the atoms in the compressed MOT, we collect about 2.5×10^5 counts per atom. Taking into account the numerical aperture of 0.15 of the vacuum window and the quantum efficiency of 60% of the camera we estimate to detect about 0.3% of the fluorescence signal on the CCD camera. With this information one can estimate the scattering rate to be 4×10^6 photons/s. The results for the total fluorescence count after many experimental cycles with different prepared atom numbers are binned into a histogram and the obtained peaks can be fitted with a sum of Gaussians. For the interpeak distance one obtains $(2.3 \pm 0.1) \times 10^5$ counts. This value is used to convert from counts to atom number. Working with a fixed interpeak distance of the Gaussian distributions one obtains

the fit presented in figure 6.2. The single peaks are clearly separated (separation of 10σ for two atoms, by 7σ for six atoms). The presented measurement is not suitable to determine the detection fidelity for atom numbers higher than four atoms because of too little statistics which leads to a bad signal to noise ratio (ochre regions in figure 6.2). To assign the other data to a concrete atom number the Gaussian distributions of the single peaks are normalized and the intersection points of adjacent peaks determined. All data within two borders is then mapped to the corresponding atom number (green regions in figure 6.2). The detection fidelity is given by $f = 1 - \epsilon$, where ϵ is the probability of incorrectly assigning a value. Since the probability distributions connected to different atom numbers are extremely well separated we obtain $f \geq 99.99\%$. This method does not take into account errors due to the uncertainty of the fit. A drawback of the MOT-imaging technique is, of course, the loss of spin information and spatial information of the atoms. Once the EMCCD camera is put into operation this problem can be tackled with the imaging technique presented in section 5.5.

6.3. State Preparation

To gain full control over the system the ability to prepare a well-defined number of atoms deterministically in the ground state is crucial. The small waist in the focus of our experiment's microtrap setup makes it suitable for this purpose because the smaller the beam waist, the larger the spacing between the levels which in turn facilitates the number state preparation. To determine the waist of the focus directly is not possible because such a measurement would require a second imaging system vis-à-vis of the objective. However, we can measure the trap frequencies in radial (ω_{rad}) and axial (ω_{ax}) direction which are directly connected to the waist. According to [Gri00] for a harmonic approximation of the optical potential the trap frequencies can be expressed as

$$\omega_{\text{rad}} = \sqrt{\frac{4U_0}{mw_0^2}}, \quad \omega_{\text{ax}} = \sqrt{\frac{2U_0}{mz_R^2}}, \quad (6.2)$$

where w_0 and z_R are waist and Rayleigh range of the Gaussian beam, U_0 describes the trap depth and m the mass of ${}^6\text{Li}$. Furthermore, knowledge of the trap frequencies allows us to estimate how localized the wave function is and therefore also to determine the tunnelling parameters of the microtrap.

Frequency modulation spectroscopy is a technique that can be used to measure the trap parameters. (For detailed descriptions of the method see also [Ser11b; Zür12; Ber13]). The idea of the method is to map out the energy separation

6. First Experimental Results

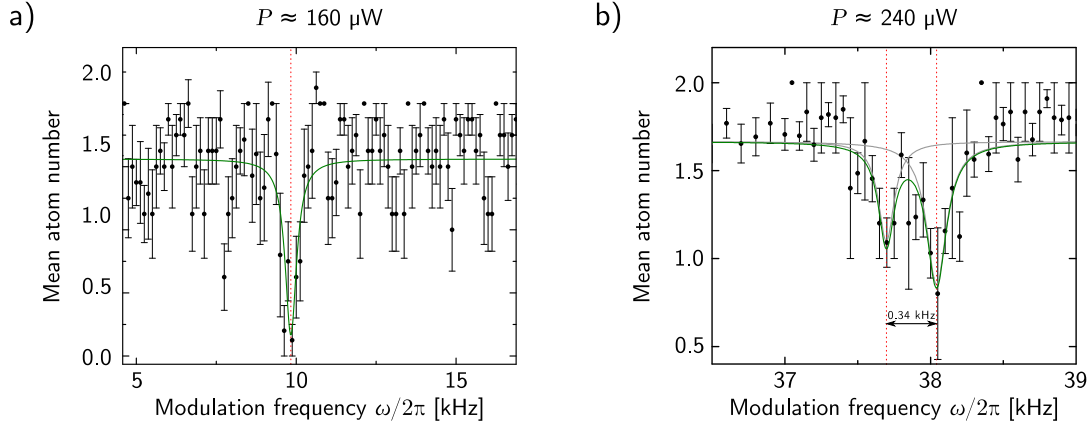


Figure 6.3.: Determination of the trap frequencies. a) At a power of about $160 \mu\text{W}$ a depletion in the mean atom number indicates a resonance at $(9.83 \pm 0.04) \text{ kHz}$. This corresponds to twice the axial trap frequency at this power. b) At a power of $240 \mu\text{W}$ we observed a double dip at around 38 kHz . It can be assigned to resonances corresponding to the radial trap frequencies. The separation of about 0.34 kHz indicates a small anisotropy of the trap of about 1% .

of the lowest trap levels and from this infer the trap frequencies. Samples of mostly two non-interacting fermions are prepared predominantly in the ground state of the microtrap according to the procedure described in section 6.1. By connecting a function generator to the AOM which is used to regulate the power of the light on the SLM breadboard we can periodically modulate the depth of the microtrap around a certain value. At the resonance the fermions are excited motionally and they start to oscillate in the approximately harmonic trap. At multiples of twice the trap frequency² the atoms oscillate at resonance resulting in a huge energy transfer. They can be excited into higher states and subsequently removed from the trap by spilling a second time. Figure 6.3 shows examples of the observed loss features for a fixed microtrap depth. Plotted are the mean atom number of several shots and their statistical error against the modulation frequency. At resonance, where the atoms are removed from the ground state, the mean atom number is clearly reduced. In figure 6.3 a) the position of the resonance is inferred with the help of a Lorentz fit to the data. By comparing the obtained frequency with results from measurements in other regimes (beam powers and modulation frequencies) it can be mapped to an excitation in axial direction. In figure 6.4 a) the axial trap frequency is plotted against microtrap beam power. Their dependence is given by a square root. Picture figure 6.3 b) shows an example for excitations of radial trap levels. The splitted structure of

²The atoms are only excited at twice the trap frequency for symmetry reasons of the modulation.

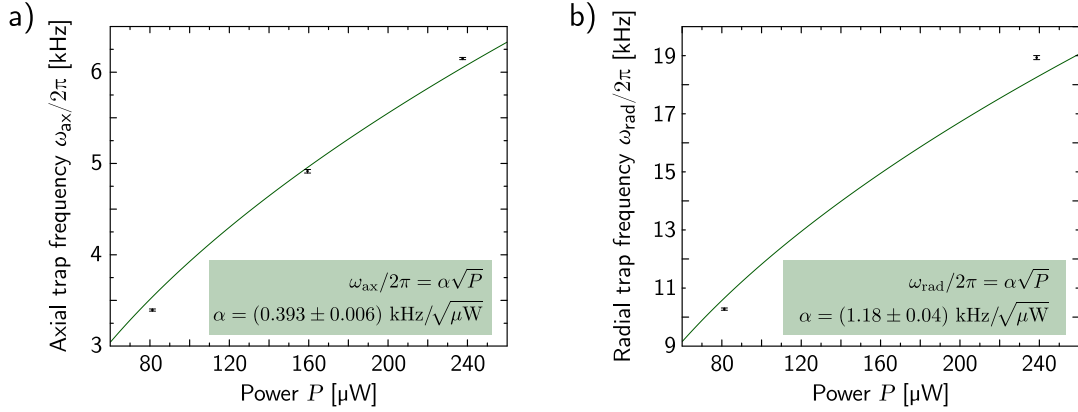


Figure 6.4.: Dependence of trap frequency on beam power. The trap frequencies are connected by a square root to the beam power. a) and b) present the results in axial and radial direction respectively. For figure b) the mean value of the frequencies measured in figure 6.3 b) was used. For the second value at lower beam power no splitted structure was observed.

the depletion, to which we fit a superposition of two Lorentzians, indicates an anisotropy of the trap of about 1%. For the dependence on the beam power in figure 6.4 b) the mean value of two radial trap frequencies is taken additionally to another measurement which does not resolve the anisotropy. With the fit results of figure 6.4 a) and b) the aspect ratio $\eta = \omega_{\text{rad}}/\omega_{\text{ax}}$ of the microtrap is given by $\eta = 3.0 \pm 0.1$. This value is significantly reduced compared to the aspect ratio measured in our groups second experiment that has an aspect ratio of $\eta \approx 7$ which works with an identical objective but cannot correct for aberrations with an SLM [Ber17].

When only the lowest trap levels of the microtrap are occupied the system can be considered as quasi one-dimensional. With the measured aspect ratio it is possible to calculate that only after the lowest five axial trap levels are filled it is energetically favourable for the system to occupy trap levels in radial direction as well. The aspect ratio together with equation (6.2) can also be used to determine the waist of the focus for which we obtain $w_0 = (718 \pm 24) \text{ nm}$.

For a deterministic preparation of a particular number of atoms the control of the barrier height while spilling is essential [Ser11a; Zür12]. Therefore, during the spilling process we scan the depth of the microtrap over a certain range at a given magnetic field gradient. The left panel in figure 6.5 shows the mean atom number in dependence of the trap depth. For each trap parameter about 370 runs are averaged. With increasing trap depth the mean number of atoms increases. It is clearly visible that for even atom numbers plateaus build up. As each trap

6. First Experimental Results

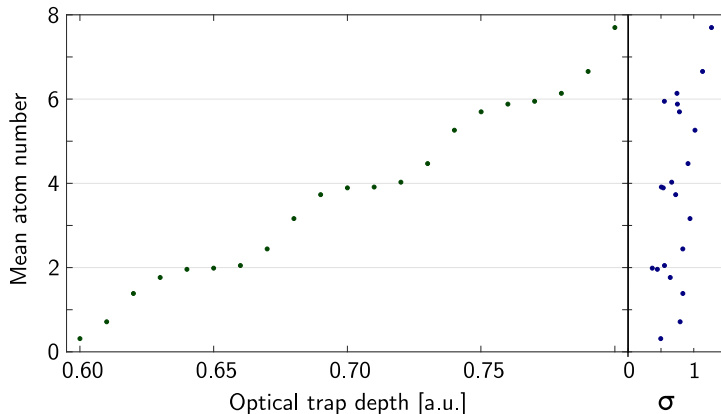


Figure 6.5.: Mean atom number against microtrap depth. The mean atom number of 370 runs is plotted against optical trap depth (left). The corresponding standard deviations of the mean value σ are plotted next to it. With increasing trap depth the number of trap levels occupied on average is growing. For even atom numbers plateaus build up and the number fluctuation is notably suppressed. These states are especially stable because each trap level can be filled with one fermion per spin state.

level can be filled with one fermion of each spin state, it is possible to prepare even atom numbers deterministically with this technique. This is also reflected by the corresponding standard deviations of the mean atom numbers (right panel). The number state fluctuations are strongly suppressed at the centre of a plateau. For two atoms (six) atoms they are reduced to $\sigma/\langle N \rangle = 0.11$ ($\sigma/\langle N \rangle = 0.07$) compared to fluctuations up to 25% for uneven atom numbers. To quantify the preparation fidelity we prepare two atoms in the regime of minimal number fluctuations. The data of 900 runs is plotted into a histogram (figure 6.6 a)). To map out the fidelity with which two atoms can be prepared the data is binned according to section 6.2. (Because the experimental parameters for the measurement taken to map out the preparation fidelity differ from those used in section 6.2 the latter results cannot be used for calibration here. Instead, the data was fitted with a superposition of Gaussians to normalize the fluorescence signal.) The fidelity to prepare two atoms is given for this measurement by 95.2%. As the detection fidelity is very close to unity it does not influence the previous result.

It is possible that the detected two-atom state is not the ground state. The sharp distribution of the atom numbers one, two and three with a probability as low as 1.9% to prepare three atoms indicates that it is unlikely to prepare atoms in trap levels higher than the first one initially and not to lose them during the spilling process. However, it is also possible that atoms are excited due to fluctuations of the trap depth or at the end of the spilling when the trap

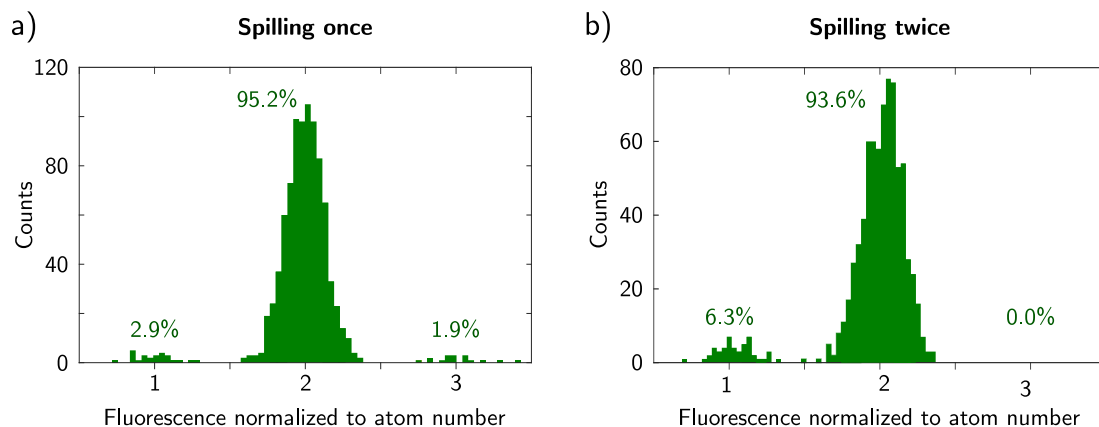


Figure 6.6.: Determination of the preparation fidelity. a) A histogram shows the result of 900 measurements at favourable parameters for the preparation of two atoms. We obtain a preparation fidelity of 95.2% for this state. b) It is possible that atoms are excited into higher trap levels due to heating. To quantify this effect one can perform a second spilling process. Taking into account the redistribution from measurements with three atoms to the measurement of two atoms after the second spilling process one obtains a probability of 91.7% to prepare the two atoms in the ground state.

is ramped back to its initial depth. To quantify the probability of ending up with an excited state after the state preparation we can perform a second spilling process which removes atoms from higher trap levels. Taking into account that all shots where three atoms were prepared after the first spilling process are ending up in the two-atom-state after the second spilling one can estimate that with $(93.6\% - 1.9\%) \approx 91.7\%$ fidelity one can prepare the two atom state in the ground state.

6.4. Testing Different Trap Geometries

Having demonstrated that we can prepare and detect atoms with high fidelity in the simplest trapping potential we can realize with the new setup in the last sections, now we want to show the capability of trapping atoms in different potential structures. As described in section 5.1 with the help of the SLM almost arbitrary two-dimensional trapping potentials can be projected onto the focal plane of the objective. A few examples of non-interacting fermions trapped in possible trapping configurations are presented in figure 6.7. For each image the average of about 20 absorption images is taken. We are not yet able to resolve single

6. First Experimental Results

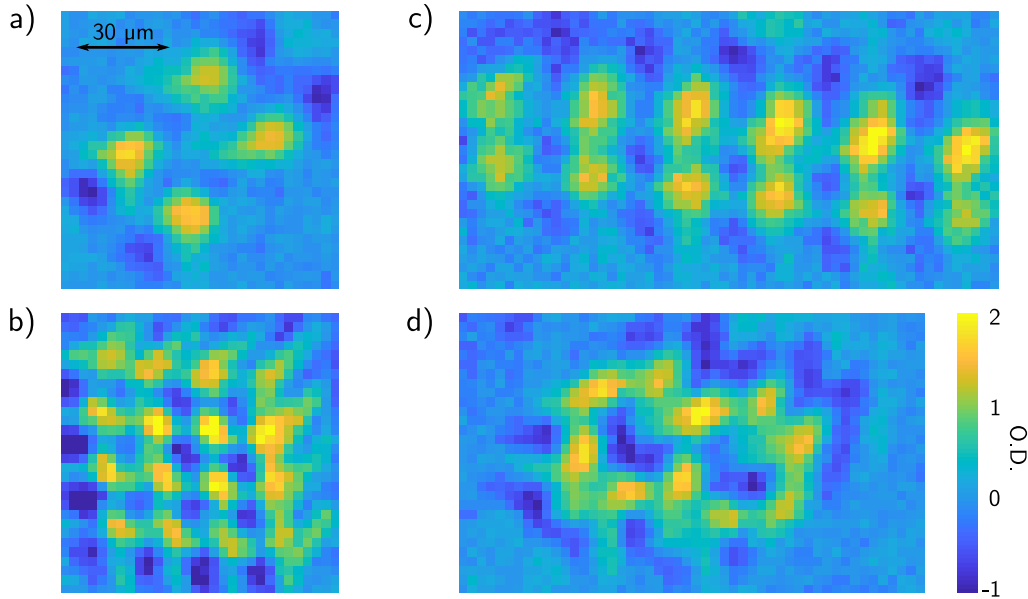


Figure 6.7.: Tailoring of the potential landscape with the SLM. Atoms can be loaded into different trap geometries projected to the Fourier plane, e.g. a plaquette (a), a square lattice (b), chains (c), a graphene structure (d). With the current imaging setup only structures of several micrometers belonging to the signal of over hundred atoms can be resolved spatially.

atoms spatially. (This will be possible with the fluorescence imaging procedure described in section 5.5.) The dimensions of the structures presented here are therefore chosen in the range of tenths of micrometers with each lattice site containing a few hundred atoms. Consequently, the potentials presented here are not suitable for tunnelling experiments where atoms of different lattice sites interact. Yet, the measurements can be used for demonstration purposes. First results for a tunnelling experiment with two distinguishable atoms in a double well follow this section (section 6.5). Once we are able to load single atoms into a lattice where the distances between neighbouring sites are at the order of a micron it is possible to create structures of more lattice sites as the examples shown here.

In summary we can show that it is in practice possible to shape the potential landscape with the SLM and load atoms into these potentials. This possibility at hand, the current experimental setup provides a promising platform to perform physics of small and mesoscopic systems trapped in potentials shaped at will in future. Especially, if we succeed to load lattices in the ground state, a great diversity of physical questions of interest, can be investigated with our setup.

6.5. Fermions in a Double-Well

The first step to increase the system of a single optical tweezer is the addition of a second trap. Such a two lattice site system can already be considered as a minimal realisation of the Hubbard model. Importantly, the double-well is the first step towards engineering mesoscopic lattice experiments and needs to be investigated in order to characterize the abilities of our experiments.

We want to apply the Hubbard model in the regime where it is restricted to a single band. This means that the bandwidth needs to be much smaller than the band gap. A small bandwidth is obtained by well localized on-site wave functions. These are provided in the experiment by adequate barriers between the wells. This means basically that the tight-binding approximation holds. To obtain a large band gap high excitation energies are required. In the experiment they are achieved by engineering large trapping frequencies. Furthermore, if interactions are included they must also be much smaller than the band gap in order to avoid population in other bands.

A consistency check if the tight-binding approximation holds in our experiments can be made by comparing the excitation energy to the tunnelling frequency as the tunnelling t between the wells is governed by the overlap of the wave functions. We analysed in section 6.3 that $\omega_{\text{ax}}/2\pi$ is on the order of a few kilohertz. For the tunnelling frequencies in the double-well we measure $\omega_{\text{tun}} = t/h \approx 230$ Hz which are well below the trap frequency. The corresponding measurements will be presented in the course of this section.

Besides, the term connected to the tunnelling t which can be controlled by the barrier height between the two wells the other contribution to the Hubbard Hamiltonian is the on-site interaction U . In our experiment interactions among atoms of different hyperfine state can be adjusted by means of the Feshbach resonance. In addition to t and U we can tune a third parameter in our experiment which is the relative depth Δ between the wells. To make sure that excited states are not contributing to the dynamics we assume U and Δ to be small compared to the excitation energy.

Let us start with the consideration of a single particle in the double-well and denote its localized states by $|L\rangle$ and $|R\rangle$ for the particle being in the left or right state respectively. The Hubbard Hamiltonian of this two level system in the $|L\rangle - |R\rangle$ -basis then reads

$$\hat{H}_{1\text{ptcl}} = \begin{pmatrix} +\Delta & -t \\ -t & -\Delta \end{pmatrix}. \quad (6.3)$$

For the balanced system $\Delta = 0$ the eigenstates of the diagonalized Hamiltonian

6. First Experimental Results

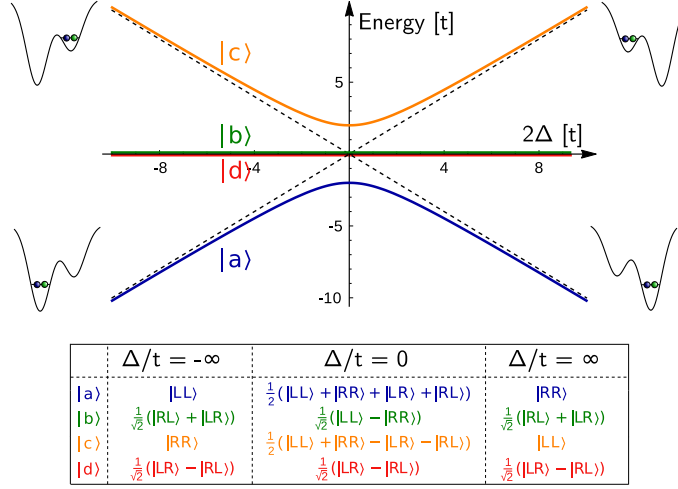


Figure 6.8.: Eigenstates and the corresponding energies of a non-interacting double-well. The plot shows the energy dependence on the potential tilt Δ/t in the regime of no on-site interaction ($U = 0$) for the corresponding eigenstates which are given in the basis of the diagonalized Hamiltonian in the table below. The physical description of the limit $U = 0$ is equivalent to the single particle case. Adapted from [Ber17]

are given by

$$|+\rangle = \frac{1}{\sqrt{2}}(|L\rangle + |R\rangle) \quad \text{and} \quad |-\rangle = \frac{1}{\sqrt{2}}(|L\rangle - |R\rangle) \quad (6.4)$$

with energies $E_+ = -t$ and $E_- = +t$.

If the complexity of the system is increased by adding a second particle of different (pseudo-)spin to the double-well the number of basis states is increased to four. With the notation introduced above for a single particle in the double-well a set of basis states is given by $\{|LL\rangle, |LR\rangle, |RL\rangle, |RR\rangle\}$ for which the Hamiltonian reads

$$\hat{H}_{2\text{ptcl}} = \begin{pmatrix} U + 2\Delta & -t & -t & 0 \\ -t & 0 & 0 & -t \\ -t & 0 & 0 & -t \\ 0 & -t & -t & U - 2\Delta. \end{pmatrix}. \quad (6.5)$$

In the experiments presented in the following we restrict ourselves to the non-interacting case $U = 0$ which is physically equivalent to the single particle scenario. The eigenstates of the diagonalized Hamiltonian are presented in the table in figure 6.8 for different regimes of Δ/t and the corresponding eigenvalues are plotted above. At finite coupling t of the balanced wells a gap of $4t$ builds up at

$\Delta/t = 0$ because in the presence of a second well $|LL\rangle$ and $|RR\rangle$ are no longer eigenstates of the system.

In a cold atoms experiment a double-well can be realized with optical dipole traps. However, different approaches are possible to do so. One option would be to partly overlap two trapping beams that are obtained from the same far red-detuned laser beam using an AOD [Mur15b]. By applying two different radio frequencies to the AOD the frequency of the incoming beam can be shifted on the order of a few megahertz $(\omega_2 - \omega_1)/2\pi$. Let us denote the electric fields of the two beams by $\mathbf{E}_j(\mathbf{r}) = \mathbf{E}_{0j} \exp(i(\mathbf{k}_j\mathbf{r} - \omega_j t + \theta))$ for $j = 1, 2$. Consequently, the intensity distribution of the beams is described by

$$\begin{aligned} I(\mathbf{r}) &= \langle |\mathbf{E}(\mathbf{r})_1 + \mathbf{E}(\mathbf{r})_2|^2 \rangle \\ &= \langle |\mathbf{E}(\mathbf{r})_1|^2 \rangle + \langle |\mathbf{E}(\mathbf{r})_2|^2 \rangle + \langle \mathbf{E}(\mathbf{r})_1 \mathbf{E}(\mathbf{r})_2^* \rangle + \langle \mathbf{E}(\mathbf{r})_2 \mathbf{E}(\mathbf{r})_1^* \rangle. \end{aligned} \quad (6.6)$$

As tunnelling of the atoms takes place at the order of 100 Hz the frequency shift in the megahertz regime averages out the last two terms. Consequently, the intensity distribution of the double-well can be simply approximated by $I_1(\mathbf{r}) + I_2(\mathbf{r})$. In this scenario the barrier height between the two wells is not given by the depth of a single

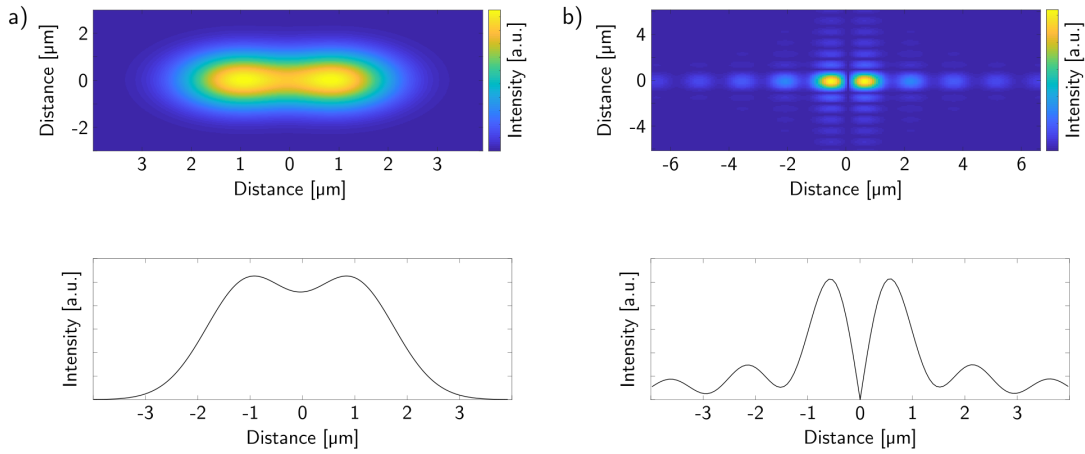


Figure 6.9.: Creation of a double-well (simulation). a) If a double-well is created by partially overlapping two microtraps the barrier height of the resulting intensity pattern is governed by the overlap of the two beams. b) Contrary, if a double-well is created by dividing the phase pattern applied to the SLM into two regions that are phase-shifted by $\Delta\Phi = \pi$ the intensity between the wells goes down to zero and therefore, the barrier has maximal height. The lower panels show cuts along x through the centre of the corresponding intensity profiles.

6. First Experimental Results

well but depends on the intensity of the single wells and the distance by which they are separated (figure 6.9 a)). This approach is taken by our groups second experiment in which tunnelling in a double-well has already been investigated in great detail [Mur15a; Mur15b; Ber17; Kli18].

With an SLM, the approach that we take, the phase of the light in the focal plane of the objective can be modulated but the frequency is unaltered. By making use of interference the limits for the intensity distribution are therefore set by $I(\mathbf{r}) = \langle |\mathbf{E}(\mathbf{r})_1 \pm \mathbf{E}(\mathbf{r})_2|^2 \rangle$. For destructive interference one can consequently work at much lower intensities compared to the method based on the AOD. An easy method to create two wells separated by a cusp of the intensity pattern that goes to zero is by dividing the SLM pattern at the centre of one axis into two regions and ramp up a phase shift of $\Delta\Phi = \pi$ in one of the halves. By this means one obtains theoretically a perfectly balanced double-well with maximized barrier height (figure 6.9 b)). In our experiment the two wells are theoretically about $1.2\ \mu\text{m}$ apart from each other. Next to the main wells side minima appear. However, their depth is at most 20% of the peak intensity and consequently it is not necessary to take them into account in our considerations. This technique allows to work at laser powers almost two orders of magnitude lower as if an AOD is used assuming to work in the same experimental regime.

In reality the two wells are not exactly balanced at $\Delta\Phi = \pi$. A possibility to determine the value $\Delta\Phi$ for a balanced double-well is to prepare two fermions of different hyperfine state in the ground state of a single well ($\Delta\Phi = 0$) and to adiabatically ramp up the second well such that one ends up in the ground state of the combined wells (see state $|a\rangle$ in figure 6.8). Pictorially we follow the blue curve in figure 6.8. Starting in the regime of a single well $\Delta/t \rightarrow -\infty$ in the ground state $|LL\rangle$ the system evolves to the ground state of the balanced well ($\Delta/t = 0$) for which the mean occupation of a single well goes to one. The route we take in the experiment is depicted in figure 6.10 from left to right. The upper panels show the applied SLM pattern and the second line the corresponding predicted intensity distribution. The lower panels are obtained by a cut along x through the centre of the intensity distribution. Plotted is the potential seen by the atoms. We proceed in the following way. We start with two atoms in a single well, for which a uniform phase pattern is applied to the SLM³ (I). We slowly ramp up a second well by splitting the SLM phase pattern into two halves and successively increasing the phase shift between the regions⁴ (II) until there is approximately no energy shift between the wells (III). The barrier height between the wells is low enough to have a coupled system of finite t . In the next step we increase

³Aberrations of the lens system are always corrected by adding a correction pattern to the SLM display.

⁴For phases between π and 2π the roles of the left and right well are exchanged.

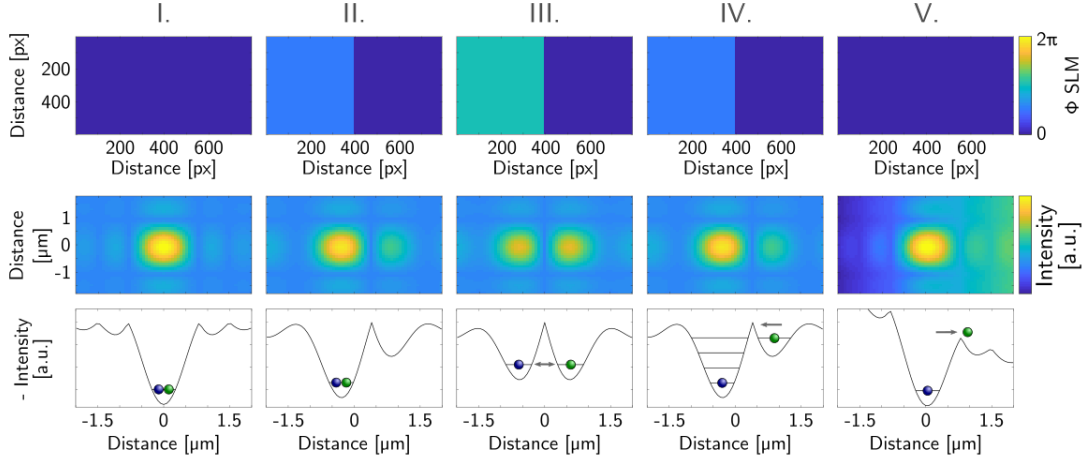


Figure 6.10.: Balancing of double-well created by the SLM. To create a double-well a phase shift $\Delta\Phi$ is ramped up on the SLM display (upper row). As a result the predicted intensity pattern in the Fourier plane transforms from a single well ($\Delta\Phi = 0$) to a double-well at $\Delta\Phi \approx \pi$ (second row). A cut through the predicted intensity distribution is shown in lower panels. To balance the system two atoms are prepared in the ground state of a single well (I), a second well is adiabatically ramped up (II & III) such that the atoms are still in the ground state of the system when the wells are approximately balanced ($\Delta\Phi \approx \pi$). For symmetric double-wells we expect to find in average one atom per well. To measure the population of a single well both wells are diabatically ramped deeper and subsequently the second well is ramped back such that particles from the right well tunnel to excited states of the left well during the process (IV). These atoms that are not in the ground state of the remaining microtrap can be removed by spilling them before the atom number is measured (V). Scanning $\Delta\Phi$ around π and checking the mean atom number allow to find out for which $\Delta\Phi$ the wells are symmetric.

the depth of both wells with a fast non-adiabatic ramp by a factor 5 to 10. As a result the states are frozen as tunnelling is suppressed. Ramping back the second well atoms tunnel from the right well into higher trap levels of the left well (IV). Finally, atoms are spilled from excited states of the remaining trap (for spilling see section 6.1). By scanning the phase around $\Delta\Phi \approx \pi$ and measuring the mean atom number we find the $\Delta\Phi$ for which the wells are balanced.

Technically, the time evolution of the double-well is realized by playing different short video tracks on the SLM each consisting of 128 pictures. Each video track consists of 128 pictures that are displayed at a 500 Hz. As the refresh rate of the SLM is 120 Hz it is not entirely deterministic how the pictures are displayed by the SLM. However, the phase increments between the pictures are sufficiently

6. First Experimental Results

small that it does not matter if pictures are skipped.

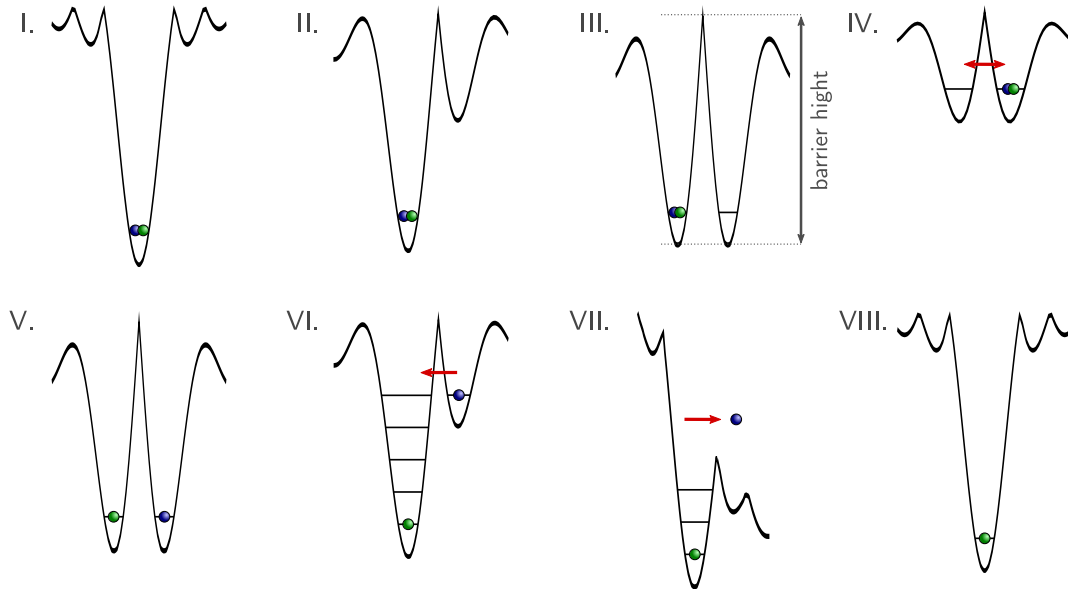


Figure 6.11.: Resonant tunnelling in a double-well. Two distinguishable fermions are prepared in the ground state of a deep microtrap (I). The second well is ramped up using the SLM (II & III). Then, we suddenly reduce the total power by 80% such that the atoms, still prepared in state $|LL\rangle$ start to tunnel (IV). As this is not a ground state of the system it evolves in time. To probe the system the depth of the wells is increased again after a variable hold time (V). The right well is ramped back (VI) such that the atoms tunnel from it into excited states of the left well (VI) and can be removed with a spilling process (VII). As a result we can measure the atom number in the ground state of the left well (VIII).

Being able to balance the double-well we can study the time evolution of resonantly tunnelling fermions (figure 6.11). As mentioned above all tunnelling experiments documented in this thesis are performed at $U = 0$. Again we start with the preparation of two fermions of two different hyperfine states in a single well (I) and ramp up a second well with the SLM (II). However, the wells are too deep to allow tunnelling between them (III). We quench the power of the trapping beam to a regime, where tunnelling is possible (IV). The time scale of the quench is much faster than the timescale of the tunnelling but slow enough not to excite atoms into higher trap levels. As a result the atoms stay in the state $|LL\rangle$. Yet the state is no longer an eigenstate of the Hamiltonian for $t \neq 0$ but can be expressed as a superposition of the set of eigenstates $\{|a\rangle, |b\rangle, |c\rangle, |d\rangle\}$ and therefore the state starts to evolve in time. After a defined hold time the trap

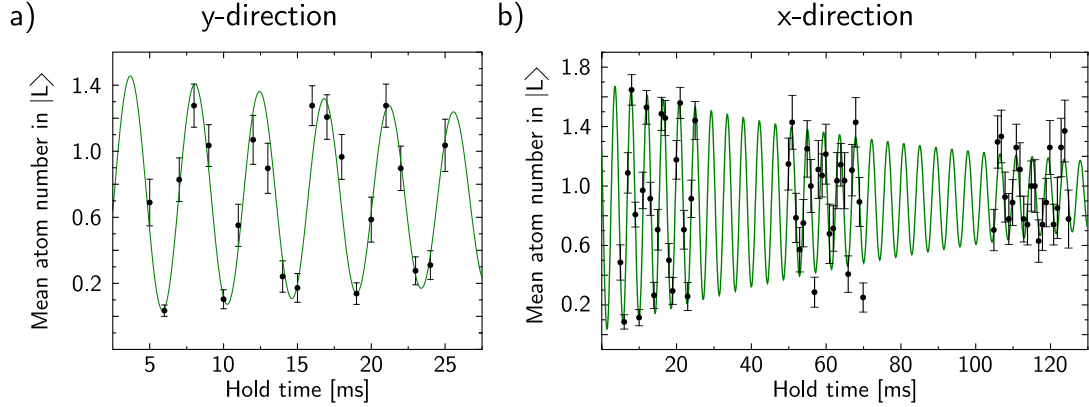


Figure 6.12.: Tunnelling in the non-interacting double-well. We are able to create double-wells along two axes depending on the axis of the SLM pattern on which we divide it into two. a) (b)) belongs to division along y (x). Plotted is the mean atom number in a single well against hold time. Several oscillations of the atoms can be detected leading to a tunnelling frequency of about 230 Hz for both orientations of the double-well. The oscillation is decaying with a rate $\Gamma = 9.85 \text{ s}^{-1} = 0.042 t/h$ which is to be interpreted as dephasing of the states and indicates noise in the regime of the tunnelling frequency.

depth is suddenly increased again (V). In the next step atoms from the right well are moved to excited states of the left well by reducing the depth of the second well such that tunnelling to higher trap levels is possible (VI). Those atoms can be removed by spilling them (VII). Finally the atoms in the ground state of the remaining microtrap can be imaged. In figure 6.12 the time evolution of the state $|LL\rangle$ is plotted. As a double-well can be created by dividing the SLM screen either along y or x into two parts we present results for both directions in a) and b) respectively. Plotted is the mean atom number in the left well against hold time. As a fit function a sinus with an exponential envelope is used to which a linear gradient is added. We obtain tunnelling frequencies $t/h \approx$ around 230 Hz for both measurements. As the atom number over a cycle is nearly constant, there seems to be no significant heating to higher trap levels (which can occur due to noise of frequencies at the order of the trap frequencies). Due to the small possibility to prepare only one atom initially we expect the mean atom number to be smaller than one. For a hold time of 25 ms for the double-well along y -direction one sees a small decay in the amplitude of the oscillation, i.e. dephasing takes place. The decay rate is fitted to be $\Gamma = 9.85 \text{ s}^{-1} = 0.042 t/h$. This becomes more evident in the measurement presented in figure 6.12 b) where the maximal hold time is five times longer. The dephasing is an indicator for noise at the order of the tun-

6. First Experimental Results

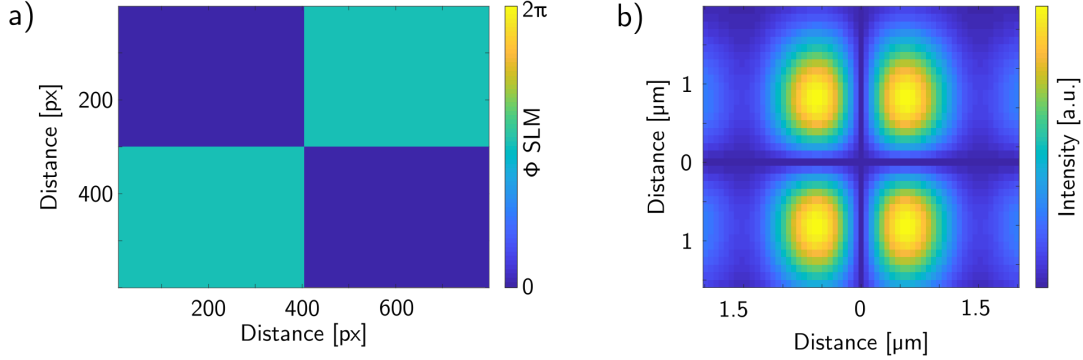


Figure 6.13.: Creating a plaquette with the SLM. a) By dividing the SLM screen into four region between which the phase is altered by π the intensity distribution for a two times two lattice sites Hubbard model can be created (b)).

nelling frequencies. A possible origin of the noise are instabilities of the relative depths of the wells. The dephasing is worse for the wells aligned along y which is likely to be linked to the technical background of how the SLM changes from one phase pattern to the other. It updates row by row of the pixels along the y direction of the screen. When the SLM is cut into halves along this axis the phase applied to the two regions flickers with respect to each other. With a refresh rate of the SLM of 120 Hz it is in the same regime as the tunnelling frequency.

With the possibility to prepare the double-well the way we desire with two possible spatial orientations the next step we want to take is to create a plaquette with the SLM. The plaquette can also be obtained by applying different phase shifts to the SLM. For the configuration shown in figure 6.13 a) the predicted trapping potentials can be described by the Hubbard model for four wells (figure 6.13 b).

This is the minimal system in which Nagaoka ferromagnetism can be possibly observed (section 3.1.2). Therefore, we aim to prepare initially three fermions in their ground state in a single well and subsequently ramp up the three other wells adiabatically. To prepare an imbalanced system with high fidelity one can prepare first a balanced system—in our case four fermions—and then exploit the magnetic field dependence of the magnetic moment of the atoms, which are prepared in two different hyperfine states. At a magnetic offset field of around 30 G the magnetic moment of atoms in hyperfine state $|2\rangle$ goes to zero. As a result the performance of a second spilling process at this field allows to only address state $|2\rangle$ during the spilling while state $|1\rangle$ is not experiencing a tilted potential. For details see for example [Zür12].

The plaquette created by the adiabatic ramp is in the state $S = 1/2$. Applying a magnetic field gradient one can couple the $S = 1/2$ state to the $S = 3/2$

6.5. Fermions in a Double-Well

state which results in an avoided crossing of the $S = 3/2$ and $S = 1/2$ branch at $U/t = 18.6$ [Ste10]. By tuning the interactions with a Feshbach resonance one can adiabatically connect the initial $S = 1/2$ state with the $S = 3/2$ state (compare figure 3.2) and therefore end in the ferromagnetic ground state predicted by Nagaoka. To probe the system one could diabatically increase the trap depth and enlarge the lattice spacing as described in section 5.5 and use the spin-resolved imaging technique described in the same section.

7. Conclusion and Outlook

In this thesis we presented the implementation of a significant extension to our experiment. The new configuration of the setup allows the creation of holographic potentials on a plane within a region of at most diameter 200 microns. Almost arbitrary structures can be realized with submicron precision. The optical potentials are projected using a spatial light modulator and a high-resolution objective. Along with the enhanced trapping setup goes a new imaging setup. Its core component is an EMCCD camera which is ready to be taken into operation.

We started by examining the most basic potential that can be created with the improved setup: a single optical tweezer. The tightly focused Gaussian beam has a waist below a micrometer. It allows to prepare small numbers of fermions in the ground state for the radial trap direction and only populating excited states in the axial direction. Our current single atom imaging method relies on recapturing the atoms at the end of the experimental sequence in the MOT and collecting part of their fluorescence on a CCD camera. By calibrating the number of measured counts we could deduce the atom number. With this scheme we reached a detection fidelity of 99.99%. A closer examination of the preparation procedure showed that we could prepare precisely two atoms in the system with a probability of more than 95%. The fidelity to prepare two atoms in the ground state was over 91%.

The next important step is the commissioning of the EMCCD camera. Although the current detection scheme allows us to deduce small atom numbers with very high precision any spin and spatial information gets lost with this technique. Once the EMCCD camera is taken into operation we can obtain these information by adapting the new imaging technique presented in [Ber18b]. This method allows to localize an atom in free space by capturing as few as 20 fluorescence photons with the high NA objective. It is possible to apply both single atom imaging techniques, first the free space imaging and subsequently the MOT imaging. The advantage to still keep the MOT imaging is that thereby the detection fidelity of the total atom number can be increased. Another important technical project for the near future is the development of methods to control the SLM dynamically. Increasing the lattice spacing is, for example, required to image lattices in real space with the EMCCD camera. On the long run additional features such as the implementation of a DMD to shoot out atoms from single lattice sites or the

7. Conclusion and Outlook

exchange of the AOD on the SLM board by a 2D-AOD could further increase the possibilities of our experiment.

In this thesis we also showed that we can prepare two atoms in a double-well and observed their tunnelling dynamics. This two-site system represents already the most basic realisation of the Hubbard model. We demonstrated that we can create a double-well along both main axes of the focal plane by introducing a phase shift of π with the SLM. With this scheme one can engineer the same barrier height between the wells with significantly less power than for a double-well created with partially overlapping Gaussian beams. Altogether, we are now in a position to gain full benefit from the add-on and to investigate larger lattices starting with a plaquette. This system offers already rich physics to discover [Par08; Ste10]. We want to use it as a starting point to explore Nagaoka ferromagnetism which is predicted to exist for half filling with a single hole but so far has never been observed. In the next step, we can enlarge the system even further up to about 10×10 lattice sites. Increasing the lattice size iteratively offers the possibility to investigate the crossover from few to many particles and to address the issue how and for which particle numbers a many-body state emerges.

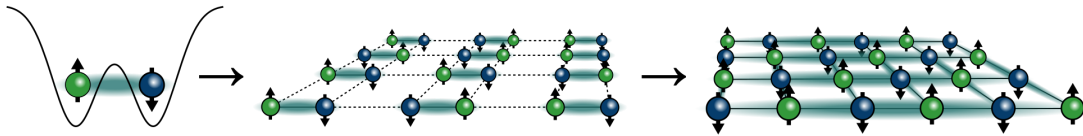


Figure 7.1.: Our vision is to individually prepare double-wells in the ground state of the Hubbard model at half filling. By adiabatically merging them we want to obtain a many-body state at very low entropy.

To initialize low entropy many-body systems in a lattice our idea is to separately prepare small building blocks which are subsequently adiabatically merged to a many-body state (figure 7.1). Double-wells serving as these building blocks could be created with the AOD which is placed in front of the SLM. To merge the wells with the AOD is more handy as it is faster and easier to handle than if one uses the SLM for the same purpose. With the approach explained here the control over the state preparation is much higher and states of much lower entropies can be reached compared to the common procedure where atoms are loaded into a lattice directly from a bulk gas. This puts us into an optimal position to investigate the rich phase diagram of the Fermi-Hubbard model. Due to the presence of strong correlations the regime is not well understood and reliable theoretical predictions lack. The imaging technique described above can be used to detect the atoms in

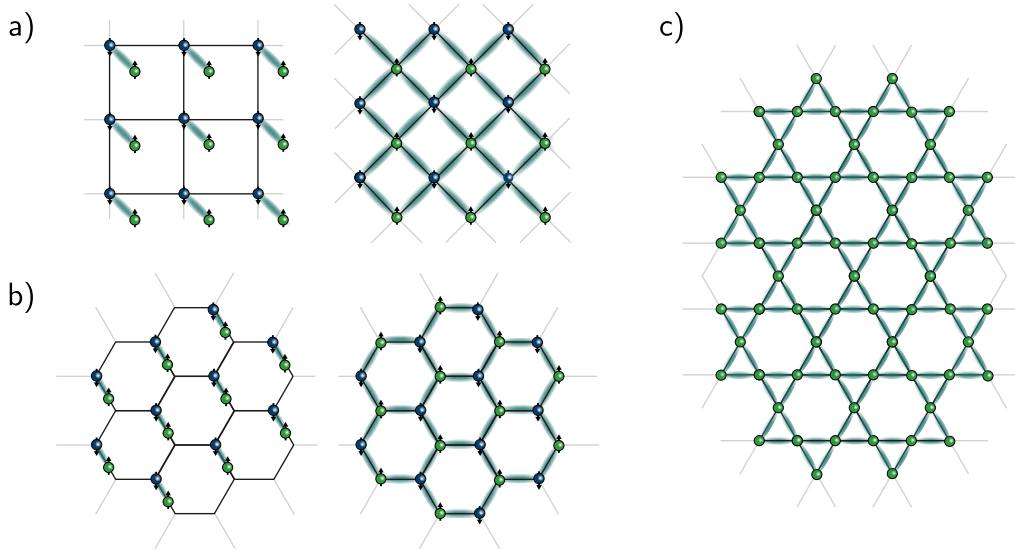


Figure 7.2.: Shaping 2D lattices. The square lattice (a) and the honeycomb lattice (b) can be created with double-wells as building blocks. c) For the kagome lattice a different approach is required. a) and b) adapted from [Hol17].

real space and momentum space making it a suitable tool for the investigation of correlations [Ber18a].

The double-well is not only suitable as building block for square lattices, including superlattices, but for any lattice geometry that can be mapped to a two-atomic basis such as spin ladders, chains of discrete lattice points or the honeycomb lattice. For other geometries, like the kagome lattice, the AOD does not represent a helpful tool (figure 7.2).

The increased flexibility to shape trapping geometries might also help to take a step towards the investigation of Majorana bound states in a 1D chain. Due to their non-Abelian braiding statistics they are considered a very promising candidate for the implementation of quantum computation. However, the major obstacle towards their realisation within our experiment is the need of p -wave superconductivity. The question if a stable p -wave superconductor can be engineered in our system needs to be addressed first.

Appendices

A. Quantum Computation

In this chapter we give more details on braiding and fusing non-Abelian anyons and on the idea how these processes could come into play in universal quantum computation.

A.1. Fusion Rules and Topological Charge Measurements

The model of non-Abelian anyons pursued in the course of this thesis is that of Ising anyons. In this model three different classes of particles exist: a topologically trivial type denoted by $\mathbf{1}$, and two non-trivial kinds with topological charges called σ (for anyonic nature) and ψ (for the fermionic case). It is not possible to convert particles of different topological charge into one another by local operations. But if they are brought close to each other they can fuse to a single quasiparticle or annihilate each other. The possible fusion processes are

$$\psi \times \psi = \mathbf{1}, \quad \sigma \times \psi = \sigma, \quad \sigma \times \sigma = \mathbf{1} + \psi. \quad (\text{A.1})$$

The first rule means that bringing two fermions close together is from a topological point of view equivalent to the case of having no particles. This can be easily understood if one thinks of the ground state of Cooper pairs in a superconductor. The second rule states that a fermion and an anyon cannot be distinguished from a single anyon. The last fusion rule is of special interest because here particles can fuse into two different channels—two combined anyons behave either like a fermion or vacuum. A projective measurement

$$F_p = -i\hat{c}_p\hat{c}_{p+1} \quad (\text{A.2})$$

can be used to quantify the fusion process of two adjacent anyons at position p and $p+1$. The operators \hat{c}_i denote the Majorana operators. They can be expressed in terms of Pauli matrices [Bra06]. The possible eigenvalues $+1$ and -1 correspond

A. Quantum Computation

to a trivial particle and one of fermionic nature, respectively. The parity operator

$$Q = (-i)^n \hat{c}_1 \hat{c}_2 \dots \hat{c}_{2n} \quad (\text{A.3})$$

extends this concept to $2n$ particles. It reflects that the topological charge is a conserved number that it cannot change by any local operation [Bra06].

A.2. Unitary Operations and Qubits in the Fusion Space

The space we work on in order to encode a qubit is called the fusion space. For Abelian anyons, which only gain a phase θ due to braiding, the fusion space is one-dimensional. For non-Abelian anyons it is multi-dimensional and depends on the chosen order for the particles to fuse. In a system consisting only of two non-Abelian anyons it is not possible to associate the two fusion channels with the basis states $|0\rangle$ and $|1\rangle$ of a single qubit because the two fusion outcomes have different topological charge (or in other words belong to different parity sectors). Since the topological charge needs to be preserved it is not possible to create states that are a superposition of $|0\rangle$ and $|1\rangle$. To overcome this n qubits must be encoded in more than $2n$ anyons. That this is useful can be illustrated by an example. A system consisting of three anyons $\sigma \times \sigma \times \sigma$ always has global topological 2σ but there are different fusion diagrams that lead to this result. For instance, one could first braid the first two quasiparticles (two different processes are possible) and then fuse the resulting particle with the third constituent (outcome is always 2σ). This provides a possible basis fusion space

$$\{ |(\sigma\sigma)\sigma \rightarrow \mathbf{1}\sigma \rightarrow \sigma\rangle, |(\sigma\sigma)\sigma \rightarrow \psi\sigma \rightarrow \sigma\rangle \} \quad (\text{A.4})$$

of the fusion space. Arrows indicate the passage of the different stages of the fusion process. The two states of the fusion space can now perfectly express the two states of a qubit and superpositions of the states necessarily conserve the topological charge. On an equal footing it is possible to consider the fusion process where 2nd and 3rd particles fuse first. Equally to our previous considerations this provides us as well with a basis of the fusion space

$$\{ |\sigma(\sigma\sigma) \rightarrow \sigma\mathbf{1} \rightarrow \sigma\rangle, |\sigma(\sigma\sigma) \rightarrow \sigma\psi \rightarrow \sigma\rangle \}. \quad (\text{A.5})$$

A.2. Unitary Operations and Qubits in the Fusion Space

A change from one basis into the other can be performed by applying a so called F -matrix. For our example it can be expressed by

$$F_{\sigma\sigma\sigma}^{\sigma} = \frac{1}{\sqrt{2}} \begin{pmatrix} 1 & 1 \\ 1 & -1 \end{pmatrix}. \quad (\text{A.6})$$

The three lowered σ denote the three internal anyons, the upper one refers to the final output after all particles are fused. For the reader familiar with quantum gates, the correspondence with the Hadamard gate is seen at once. Besides, making a basis change in the fusion space it is also possible to braid the particles. This is done by applying R -matrices which change the phase. In general, a braid in clockwise direction of two of two particles with topological quantum number a and b , which can potentially fuse into a particle of topology c , is expressed by $R_{ab}^c = \exp(i\theta_{ab}^c)$. Consider as an example the clockwise exchange of the left-most σ anyons

$$R = \begin{pmatrix} R_{\sigma\sigma}^{\mathbf{1}} & 0 \\ 0 & R_{\sigma\sigma}^{\psi} \end{pmatrix} = \begin{pmatrix} e^{-i\pi/8} & 0 \\ 0 & e^{i3\pi/8} \end{pmatrix}. \quad (\text{A.7})$$

On the diagonal are the two different options for a braiding process of two σ anyons¹. With these tools, now also other braiding scenarios can be realized if the particles are braided in a different order.

To create now a system with more than one qubit exactly the same methods we have just gotten to know can be used. For example, two qubits can be created with six anyons. Their total topological charge is always $\mathbf{1}$, i.e. trivial. Now a basis is again chosen by deciding on a fusing order. Counting the fusion channels for this “path” gives four eigenstates—each of them can be assigned to one of the two-qubit states $|00\rangle$, $|01\rangle$, $|10\rangle$ and $|11\rangle$. Single-qubit transformations, as in the example above, can be implemented by only acting on a subspace (see [Lah17] for details).

Clifford operations together with a $\pi/8$ -phase gate are a possibility to give a complete set of gates for universal quantum computation. As already indicated in the main text and as we saw here, this cannot be achieved with the F - and R -matrices. The $\pi/8$ -phase gate needs to be introduced in another way, e.g. non-topologically by bringing the two anyons close to each other for a certain time and exploiting the fact that they dephase.

We conclude with a short summary of basic steps to engineer quantum computation in an experiment:

¹The missing R -matrices not introduced yet are given by $R_{\psi\psi}^{\mathbf{1}} = -1$ and $R_{\sigma\psi}^{\sigma} = i$

A. Quantum Computation

1. The system can be initialized by creating the required number of pairs of anyons from the vacuum and fixing their position.
2. B - and F -matrices can be used for the computational process.
3. A projective measurement can be performed on the final state. This can be done by bringing the particles close to each other and measuring the energy.

B. Fourier Transforming with a Thin Lens

In section 2.3.2 it was already explained on a qualitative level how a spherical thin lens transforms an ingoing wave into its Fourier transformation. This chapter provides a more substantial demonstration of the transformation properties of a lens¹.

We consider the scenario where a plane wave that can be described as $f(x, y) = U(x, y, 0)$ at the plane $z = 0$ travels towards a thin lens of thickness Δ positioned at $z = d$. The focal plane of the lens is at a distance f from the lens (figure B.1). For later use it is helpful to introduce the *transfer function* in Fresnel approximation²

$$H_d(\nu_x, \nu_y) = \mathcal{H}_d e^{i\pi\lambda d(\nu_x^2 + \nu_y^2)}, \quad \text{with } \mathcal{H}_d = e^{-ikd}. \quad (\text{B.1})$$

Fourier transforming this expression gives the *impulse response function*

$$h_d(x, y) = \mathfrak{h}_d e^{-ik\frac{x^2 + y^2}{2d}}, \quad \text{with } \mathfrak{h}_d = \frac{i}{\lambda d} e^{-ikd}. \quad (\text{B.2})$$

To examine the transformation properties of a thin lens let us start with a single plane wave $U(x, y, 0) \equiv f(x, y) = F(\nu_x, \nu_y) \exp(-i2\pi(\nu_x x + \nu_y y))$ that travels under a small angle $\theta_x = \lambda\nu_x$ and $\theta_y = \lambda\nu_y$. The wave passes three different stages subsequently. First it propagates in free space over a distance d , next it passes a thin lens of thickness Δ and finally, it propagates in free space to the focal plane at distance f . Comparing with equation (2.16) one sees that for the free space propagation of a single plane wave the integration can be omitted. Crossing the lens in the next step multiplies the lens phase factor $\exp(i\pi(x^2 + y^2)/(\lambda f))$

¹An optical Fourier transform can also be obtained in the far field without using a lens if the Fraunhofer approximation is applicable [Sal91].

²In the Fresnel approximation is applicable for a wave that travels close to the axis of propagation. Provided this axis is the z -axis this condition can be expressed as $\nu_x^2 + \nu_y^2 \ll 1/\lambda^2$. Under this constraint a Taylor expansion of the ray travelling close to the z -axis is possible.

B. Fourier Transforming with a Thin Lens

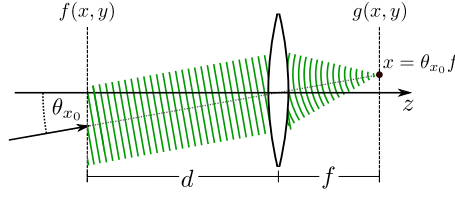


Figure B.1.: An incoming plane wave is focused down to a point in the focal plane by a lens. The position of this point depends on the angle the ingoing wave has with respect to the lens.

to the wave function³. At position $d + \Delta$ it reads

$$U(x, y, d + \Delta) = \underbrace{U(x, y, 0)}_{\text{initial wave}} \underbrace{H_d(\nu_x, \nu_y)}_{\text{propagation for } d} \underbrace{e^{i\pi \frac{(x^2+y^2)}{(\lambda f)}}}_{\text{lens phase factor}}. \quad (\text{B.3})$$

As $U(x, y, d + \Delta)$ is now a spherical wave one needs to perform a convolution (equation (2.17)) in order to express the subsequent free space propagation over the distance f

$$g(x, y) \equiv U(x, y, d + \Delta + f) = \int_{-\infty}^{\infty} \int_{-\infty}^{\infty} dx' dy' U(x', y', d + \Delta) h_f(x - x', y - y'). \quad (\text{B.4})$$

To evaluate $g(x, y)$ the transfer function and impulse response function in Fresnel approximation (equations B.1, B.2) are used [Sal91]. This yields

$$g(x, y) = \mathcal{H}_d \mathcal{H}_f e^{i\pi \frac{(x^2+y^2)(d-f)}{(\lambda f^2)}} F\left(\frac{x}{\lambda f}, \frac{y}{\lambda f}\right) \quad (\text{B.5})$$

in the focal plane with $\nu_x = x/(\lambda f)$ and $\nu_y = y/(\lambda f)$. For $d = f$ the phase factor can be omitted and the equation simplifies further to

$$g(x, y) = \mathcal{H}_f \mathcal{H}_f F\left(\frac{x}{\lambda f}, \frac{y}{\lambda f}\right). \quad (\text{B.6})$$

Equation (B.6) shows that a lens can be used to apply a Fourier transform to a wave function.

³The phase factor $\exp(-ik\Delta)$ is neglected.

C. Technical Details of the LCOS Spatial Light Modulator by Hamamatsu

In our experiment we use a phase modulating liquid crystal on silicon spatial light Modulator (LCOS-SLM) by Hamamatsu [Ham]. The X10468-03 SLM that is implemented in our experiment model uses a dielectric multilayer mirror that is specified for (1050 ± 50) nm and has a light utilization efficiency of up to 95 %. The following list gives further device specifications.

- chip size: 15.8 mm \times 12.0 mm
- resolution: 792 \times 600
- pixel size: 20 μ m
- number of input levels: 256 levels (8 bits)
- input signal: Digital Video Interface (DVI-D)
- refresh rate: 120 Hz
- liquid crystal drive cycle: 240 Hz (AC)
- rise time: 20 ms
- fall time: 80 ms
- maximal incident laser power: ~ 5 W

The SLM has its own controller unit which is connected to the graphics card of a computer. The SLM can then be controlled with a LabVIEW program that is designed in a modular style. It is used to control the SLM, calculate phase patterns and read out different cameras.

D. Alignment Protocol for the Objective

As stated in the main text it is important to align the optical axis of the objective perpendicular to the vacuum window in order to attain a good performance. Reproducibility of the objective's alignment is achieved by using an alignment beam (beam of wavelength $\lambda = 532$ nm, green in figure D.1). It reaches the breadboard at outcoupler **A** and is subsequently split up by a cube. One part, we call it *reference beam*, is focused down with a $f = 100$ mm lens to a CCD camera (Pointgrey Flea FL2G-13S2M-C). The other part, referred to as *alignment beam*, is directed to the vacuum window. To determine the optical axis of the objective we work with a test setup and imitate the vacuum window with a test window. In the first step the objective is taken out of the setup. Without passing the objective the alignment beam hits the surface of the test window and a part of the light is reflected at its surface. We make sure that the alignment beam is perpendicular to the test window by checking that some of the reflected light is coupled back into the fibre. (In the test setup one can overlap the two beams simply by turning the test window.) Now, the reference beam is aligned to the back reflected beam (mirror 1) such that the position of the two beams coincide on the CCD camera. The position of the back reflected beam on the camera is sensitive to the angle of the objective and thus, in the following, we can use it to record the tilt of the tubing of the objective with respect to the optical axis, which is required to be parallel to the back reflection from the vacuum window. We proceed by taking back the objective and placing a mirror on top of it. As a starting position we tilt the objective such that the beam that is reflected back from the mirror impinges at the reference position on the CCD camera. To adjust the tilt around the x - and y -axis the mount of the objective provides two screws. Next, the mirror is removed and a gold grating attached to a x -, y -, z -stage is placed roughly in the focus of the objective. Its holes have a diameter of 650 nm and are separated by 20 μm . The gold grating is illuminated from below (position **B** in figure D.1) with red light ($\lambda = 671$ nm), after the light passed the objective it is focused down with a $f = 750$ mm lens to another CCD camera (Thorlabs beam profiler BC106-VIS). One can observe a diffraction pattern that depends on the z -position of the grating called Talbot effect. Only when the grating is placed perfectly in the focal

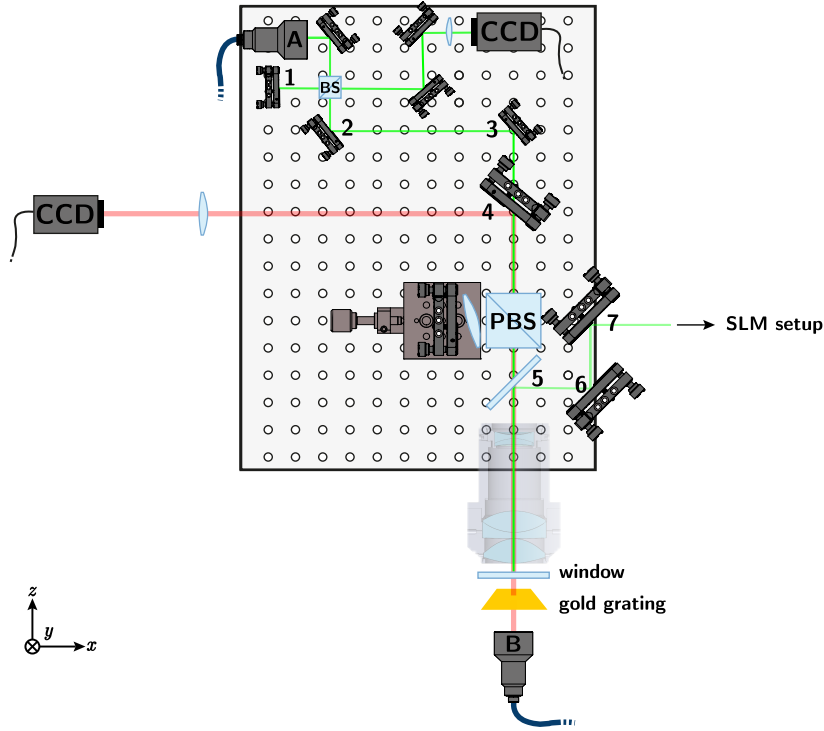


Figure D.1.: A gold grating placed in the focus of the objective is used as a tool to find the optical axis of the objective (beam path of red beam). The green alignment beam is used to attain a reference of this position. Adapted from [Hol17].

plane we see a clear image of it. This way the grating can be placed in focus with a very high precision. However, the pattern still shows aberrations. They can be reduced by tilting the objective around the x - and y -axis with the corresponding screws. The least aberrations are obtained when the optical axis of the objective is vertical to the vacuum window. It is important to make sure that this tilt is maintained after locking the tilting screws. This part is critical because the mount is designed for lighter optics which results in the effect that the tilt is coupled to the locking. If now the mirror is again placed on top of the objective. The spot of the reference position and of the back reflected beam on the alignment camera are separated by a distance Δx and Δy in x - and y -direction, respectively. The tilt of the tubing can be calculated according to

$$\theta_i = \frac{\Delta i}{f} \quad \text{for } i = x, y \quad (\text{D.1})$$

D. Alignment Protocol for the Objective

with $f = 100$ mm being the focal length of the lens placed before the camera. One obtains $\theta_x = 4$ mrad and $\theta_y = 12$ mrad.

Once the vertical breadboard is implemented in the experiment the alignment beam is aligned central (mirror 2) and perpendicular (mirror 3) to the vacuum window. (The beam is perpendicular if the spot of back reflection on the CCD camera coincides with the one of the reference beam.) We check if some light is coupled back to the fibre to make sure that the incident and back reflected beam overlap. The next step is to implement the objective. Due to the fact that the diameter of the re-entrant viewport in our experiment is smaller than the one in the experiment the objective was designed for in the first place (40 mm compared to 44 mm) the objective fits only with millimetre precision. Additionally, there is only one orientation to fit in the objective because the re-entrant viewport is partly occupied by pipes for water cooling of the Feshbach coils and small iron blocks that are placed there to move the magnetic saddle of their magnetic field when used in Helmholtz configuration¹. Once being installed in the experiment the objective is aligned passively: The mirror is placed on top of it and by looking at the CCD camera its tilt is adjusted to the one determined in the test setup.

Additionally, we use the alignment beam to align the infrared beam that stems from the SLM breadboard. Therefore, the mirror is again placed on top of the objective. A part of the beam is reflected at the dichroic at position 5 in figure D.1. With the help of mirror 6 we can align the green beam to the infrared beam at the focus of the latter (position **C** in figure 5.3). Mirror 7 can be used to align the beam to the centre of the objective's entrance.

¹During the implementation procedure we needed to change the position of these magnetizable blocks to free enough space for the objective. It was taken care that the position of the zero-crossing of the coils in anti-Helmholtz configuration was identical to the one of the magnetic saddle.

Bibliography

- [Ale96] Alessandrello, A, Brofferio, C, Bucci, C, Camin, D.V, Cremonesi, O, Fiorini, E, Giuliani, A, Nucciotti, A, Pavan, M, Pessina, G, Previtali, E, and Zanotti, L. *The Milano-Gran Sasso double beta decay experiment: toward a 20-crystal array. Nuclear Instruments and Methods in Physics Research Section A: Accelerators, Spectrometers, Detectors and Associated Equipment* 370.1 (1996). Proceedings of the Sixth International Workshop on Low Temperature Detectors, pp. 241–243.
- [Ali11] Alicea, Jason, Oreg, Yuval, Refael, Gil, Oppen, Felix von, and Fisher, Matthew P. A. *Non-Abelian statistics and topological quantum information processing in 1D wire networks. Nature Physics* 7 (Feb. 2011). Article.
- [Ali12] Alicea, Jason. *New directions in the pursuit of Majorana fermions in solid state systems. Reports on Progress in Physics* 75.7 (2012), p. 076501.
- [And33] Anderson, Carl D. *The Positive Electron. Phys. Rev.* 43 (6 Mar. 1933), pp. 491–494.
- [Bak09] Bakr, Waseem S, Gillen, Jonathon I, Peng, Amy, Fölling, Simon, and Greiner, Markus. *A quantum gas microscope for detecting single atoms in a Hubbard-regime optical lattice. Nature* 462.7269 (2009), pp. 74–77.
- [Bar18] Barredo, Daniel, Lienhard, Vincent, Léséleuc, Sylvain de, Lahaye, Thierry, and Browaeys, Antoine. *Synthetic three-dimensional atomic structures assembled atom by atom. Nature* 561.7721 (2018), pp. 79–82.
- [Bec16] Becher, J. H. W. *Towards Spin and Site-Resolved, Single-Atom Imaging of ^6Li Atoms in a Multiwell Potential*. Master thesis. Heidelberg University, 2016.

Bibliography

- [Bee13] Beenakker, C.W.J. *Search for Majorana Fermions in Superconductors. Annual Review of Condensed Matter Physics* 4.1 (2013), pp. 113–136.
- [Ber13] Bergschneider, Andrea. *Ultracold few-fermion systems in multiwell potentials*. Master thesis. Heidelberg University, 2013.
- [Ber17] Bergschneider, Andrea. *Strong correlations in few-fermion systems*. PhD thesis. Heidelberg University, 2017.
- [Ber18a] Bergschneider, Andrea, Klinkhamer, Vincent M., Becher, Jan Hendrik, Klemt, Ralf, Palm, Lukas, Zürn, Gerhard, Jochim, Selim, and Preiss, Philipp M. *Correlations and Entanglement in an Itinerant Quantum System*. 2018.
- [Ber18b] Bergschneider, Andrea, Klinkhamer, Vincent M., Becher, Jan Hendrik, Klemt, Ralf, Zürn, Gerhard, Preiss, Philipp M., and Jochim, Selim. *Spin-resolved single-atom imaging of ${}^6\text{Li}$ in free space*. *Phys. Rev. A* 97 (6 June 2018), p. 063613.
- [Ber72] Berezinskii, V. L. *Destruction of long-range order in one-dimensional and two-dimensional systems possessing a continuous symmetry group. II. Quantum systems*. *Sov. Phys. JETP* 34.610 (1972), p. 1181.
- [Bij13] Bijnen, Rick Martinus Wilhelmus van. *A Strongly Interacting Fermi Gas in a Two-Dimensional Optical Lattice*. PhD thesis. Eindhoven University of Technology, 2013.
- [Boe16] Boettcher, I., Bayha, L., Kedar, D., Murthy, P. A., Neidig, M., Ries, M. G., Wenz, A. N., Zürn, G., Jochim, S., and Enss, T. *Equation of State of Ultracold Fermions in the 2D BEC-BCS Crossover Region*. *Phys. Rev. Lett.* 116 (4 Jan. 2016), p. 045303.
- [Bol16] Boll, Martin, Hilker, Timon A., Salomon, Guillaume, Omran, Ahmed, Nespolo, Jacopo, Pollet, Lode, Bloch, Immanuel, and Gross, Christian. *Spin- and density-resolved microscopy of antiferromagnetic correlations in Fermi-Hubbard chains*. *Science* 353.6305 (2016), pp. 1257–1260.
- [Bow10] Bowman, Richard W, Wright, Amanda J, and Padgett, Miles J. *An SLM-based Shack–Hartmann wavefront sensor for aberration correction in optical tweezers*. *Journal of Optics* 12.12 (2010), p. 124004.

- [Bra06] Bravyi, Sergey. *Universal quantum computation with the $\nu = 52$ fractional quantum Hall state*. *Phys. Rev. A* 73 (4 Apr. 2006), p. 042313.
- [Bru11] Bruce, Graham D, Mayoh, James, Smirne, Giuseppe, Torralbo-Campo, Lara, and Cassettari, Donatella. *A smooth, holographically generated ring trap for the investigation of superfluidity in ultracold atoms*. *Physica Scripta* 2011.T143 (2011), p. 014008.
- [Cao18] Cao, Yuan, Fatemi, Valla, Fang, Shiang, Watanabe, Kenji, Taniguchi, Takashi, Kaxiras, Efthimios, and Jarillo-Herrero, Pablo. *Unconventional superconductivity in magic-angle graphene superlattices*. *Nature* 556 (Mar. 2018).
- [Che15] Cheuk, Lawrence W., Nichols, Matthew A., Okan, Melih, Gersdorf, Thomas, Ramasesh, Vinay V., Bakr, Waseem S., Lompe, Thomas, and Zwierlein, Martin W. *Quantum-Gas Microscope for Fermionic Atoms*. *Phys. Rev. Lett.* 114 (19 May 2015), p. 193001.
- [Che16] Cheuk, Lawrence W., Nichols, Matthew A., Lawrence, Katherine R., Okan, Melih, Zhang, Hao, Khatami, Ehsan, Trivedi, Nandini, Paiva, Thereza, Rigol, Marcos, and Zwierlein, Martin W. *Observation of spatial charge and spin correlations in the 2D Fermi-Hubbard model*. *Science* 353.6305 (2016), pp. 1260–1264.
- [Cla16] Classen, Benjamin. *Intensity Stability of Potentials created with an Analog Spatial Light Modulator*. Bachelor Thesis. Heidelberg University, 2016.
- [Dal85] Dalibard, J. and Cohen-Tannoudji, C. *Dressed-atom approach to atomic motion in laser light: the dipole force revisited*. *J. Opt. Soc. Am. B* 2.11 (Nov. 1985), pp. 1707–1720.
- [Dal89] Dalibard, J. and Cohen-Tannoudji, C. *Laser cooling below the Doppler limit by polarization gradients: simple theoretical models*. *J. Opt. Soc. Am. B* 6.11 (Nov. 1989), pp. 2023–2045.
- [Dav08] Davidson, Sacha, Nardi, Enrico, and Nir, Yosef. *Leptogenesis*. *Physics Reports* 466.4 (2008), pp. 105–177.

Bibliography

- [Dir28] Dirac, Paul. *The quantum theory of the electron. Proceedings of the Royal Society of London A: Mathematical, Physical and Engineering Sciences* 117.778 (1928), pp. 610–624.
- [Edg15] Edge, G. J. A., Anderson, R., Jervis, D., McKay, D. C., Day, R., Trotzky, S., and Thywissen, J. H. *Imaging and addressing of individual fermionic atoms in an optical lattice. Phys. Rev. A* 92 (6 Dec. 2015), p. 063406.
- [End16] Endres, Manuel, Bernien, Hannes, Keesling, Alexander, Levine, Harry, Anschuetz, Eric R., Krajenbrink, Alexandre, Senko, Crystal, Vuletic, Vladan, Greiner, Markus, and Lukin, Mikhail D. *Atom-by-atom assembly of defect-free one-dimensional cold atom arrays. Science* 354.6315 (2016), pp. 1024–1027.
- [Fu08] Fu, Liang and Kane, C. L. *Superconducting Proximity Effect and Majorana Fermions at the Surface of a Topological Insulator. Phys. Rev. Lett.* 100 (9 Mar. 2008), p. 096407.
- [Gae07] Gaebler, J. P., Stewart, J. T., Bohn, J. L., and Jin, D. S. *p-Wave Feshbach Molecules. Phys. Rev. Lett.* 98 (20 May 2007), p. 200403.
- [Gau12] Gaunt, Alexander L. and Hadzibabic, Zoran. *Robust Digital Holography For Ultracold Atom Trapping. Scientific Reports* 2 (Oct. 2012). Article.
- [Gre02] Greiner, Markus, Mandel, Olaf, Esslinger, Tilman, Hänsch, Theodor W., and Bloch, Immanuel. *Quantum phase transition from a superfluid to a Mott insulator in a gas of ultracold atoms. Nature* 415 (Jan. 2002). Article, pp. 39–44.
- [Gri00] Grimm, Rudolf, Weidemüller, Matthias, and Ovchinnikov, Yurii B. *Optical Dipole Traps for Neutral Atoms. Advances In Atomic, Molecular, and Optical Physics* 42 (2000). Ed. by Bederson, Benjamin and Walther, Herbert, pp. 95–170.
- [Gut63] Gutzwiller, Martin C. *Effect of Correlation on the Ferromagnetism of Transition Metals. Phys. Rev. Lett.* 10 (5 Mar. 1963), pp. 159–162.

- [Hal15] Haller, Elmar, Hudson, James, Kelly, Andrew, Cotta, Dylan A., Peaudecerf, Bruno, Bruce, Graham D., and Kuhr, Stefan. *Single-atom imaging of fermions in a quantum-gas microscope*. *Nature Physics* 11 (July 2015), pp. 738–742.
- [Ham] Hamamatsu. *LCOS-SLM (Optical Phase Modulator) X10468-03*. <http://www.hamamatsu.com/jp/en/X10468-03.html>. [Online; accessed 2018-06-25].
- [Har14] Harte, Tiffany, Bruce, Graham D., Keeling, Jonathan, and Cassettari, Donatella. *Conjugate gradient minimisation approach to generating holographic traps for ultracold atoms*. *Opt. Express* 22.22 (Nov. 2014), pp. 26548–26558.
- [Has10] Hasan, M. Z. and Kane, C. L. *Colloquium: Topological insulators*. *Rev. Mod. Phys.* 82 (4 Nov. 2010), pp. 3045–3067.
- [Hol14] Holten, Marvin. *Hamiltonian Engineering in Ultracold Atom Experiments using a Spatial Light Modulator*. Bachelor Thesis. Heidelberg University, 2014.
- [Hol17] Holten, Marvin. *Collective Modes and Turbulence in Two-Dimensional Fermi Gases*. Master thesis. Heidelberg University, 2017.
- [Hol18] Holten, Marvin, Bayha, Luca, Klein, Antonia C., Murthy, Puneet A., Preiss, Philipp M., and Jochim, Selim. *Anomalous breaking of scale invariance in a two-dimensional Fermi gas*. 2018.
- [Hub63] Hubbard, John. *Electron correlations in narrow energy bands*. *Proceedings of the Royal Society of London A: Mathematical, Physical and Engineering Sciences* 276.1365 (1963), pp. 238–257.
- [Jia11] Jiang, Liang, Kitagawa, Takuya, Alicea, Jason, Akhmerov, A. R., Pekker, David, Refael, Gil, Cirac, J. Ignacio, Demler, Eugene, Lukin, Mikhail D., and Zoller, Peter. *Majorana Fermions in Equilibrium and in Driven Cold-Atom Quantum Wires*. *Phys. Rev. Lett.* 106 (22 June 2011), p. 220402.
- [Kan63] Kanamori, Junjiro. *Electron Correlation and Ferromagnetism of Transition Metals*. *Progress of Theoretical Physics* 30.3 (1963), pp. 275–289.

Bibliography

- [Kar09] Karski, M., Förster, L., Choi, J. M., Alt, W., Widera, A., and Meschede, D. *Nearest-Neighbor Detection of Atoms in a 1D Optical Lattice by Fluorescence Imaging*. *Phys. Rev. Lett.* 102 (5 Feb. 2009), p. 053001.
- [Ket08] Ketterle, W. and Zwierlein, M. W. *Making, probing and understanding ultracold Fermi gases*. (2008).
- [Kim17] Kim, Hyosub, Lee, Woojun, and Ahn, Jaewook. *Deterministic single-atom array preparation using dynamic holographic optical tweezers*. *Conference on Lasers and Electro-Optics*. Optical Society of America, 2017, FTu3E.8.
- [Kit01] Kitaev, A Yu. *Unpaired Majorana fermions in quantum wires*. *Physics-Uspekhi* 44.10S (2001), p. 131.
- [Kit03] Kitaev, A.Yu. *Fault-tolerant quantum computation by anyons*. *Annals of Physics* 303.1 (2003), pp. 2–30.
- [Kli12] Klinkhamer, Vincent Mirou. *An apparatus for few-fermion systems in multiple well potentials*. Master thesis. Heidelberg University, 2012.
- [Kli18] Klinkhamer, Vincent Mirou. *Few-Fermion Systems under a Matter-wave Microscope*. PhD thesis. Heidelberg University, 2018.
- [Kli80] Klitzing, K. v., Dorda, G., and Pepper, M. *New Method for High-Accuracy Determination of the Fine-Structure Constant Based on Quantized Hall Resistance*. *Phys. Rev. Lett.* 45 (6 Aug. 1980), pp. 494–497.
- [Kos73] Kosterlitz, J M and Thouless, D J. *Ordering, metastability and phase transitions in two-dimensional systems*. *Journal of Physics C: Solid State Physics* 6.7 (1973), p. 1181.
- [Kug15] Kugele, Alexander. *Time-resolved Image Acquisition of Optical Potentials created by a Spatial Light Modulator*. Bachelor Thesis. Heidelberg University, 2015.
- [Lah17] Lahtinen, Ville and Pachos, Jiannis K. *A Short Introduction to Topological Quantum Computation*. *SciPost Phys.* 3 (3 2017), p. 021.
- [Lut10] Lutchyn, Roman M., Sau, Jay D., and Das Sarma, S. *Majorana Fermions and a Topological Phase Transition in Semiconductor-Superconductor Heterostructures*. *Phys. Rev. Lett.* 105 (7 Aug. 2010), p. 077001.

- [Maj37] Majorana, Ettore. *Teoria simmetrica dell'elettrone e del positrone. Il Nuovo Cimento (1924-1942)* 14.4 (1937), p. 171.
- [Maz17] Mazurenko, Anton, Chiu, Christie S., Ji, Geoffrey, Parsons, Maxwell F., Kanász-Nagy, Márton, Schmidt, Richard, Grusdt, Fabian, Demler, Eugene, Greif, Daniel, and Greiner, Markus. *A cold-atom Fermi-Hubbard antiferromagnet. Nature* 545 (May 2017), pp. 462–466.
- [Mir15] Miranda, Martin, Inoue, Ryotaro, Okuyama, Yuki, Nakamoto, Aki-masa, and Kozuma, Mikio. *Site-resolved imaging of ytterbium atoms in a two-dimensional optical lattice. Phys. Rev. A* 91 (6 June 2015), p. 063414.
- [Moo91] Moore, Gregory and Read, Nicholas. *Nonabelions in the fractional quantum hall effect. Nuclear Physics B* 360.2 (1991), pp. 362–396.
- [Mou12] Mourik, V., Zuo, K., Frolov, S. M., Plissard, S. R., Bakkers, E. P. A. M., and Kouwenhoven, L. P. *Signatures of Majorana Fermions in Hybrid Superconductor-Semiconductor Nanowire Devices. Science* 336.6084 (May 2012), pp. 1003–1007.
- [Mur14] Murthy, P. A., Kedar, D., Lompe, T., Neidig, M., Ries, M. G., Wenz, A. N., Zürn, G., and Jochim, S. *Matter-wave Fourier optics with a strongly interacting two-dimensional Fermi gas. Phys. Rev. A* 90 (4 Oct. 2014), p. 043611.
- [Mur15a] Murmann, Simon. *Many-Body Pairing in a Two-Dimensional Fermi Gas*. PhD thesis. Heidelberg University, 2015.
- [Mur15b] Murmann, Simon, Bergschneider, Andrea, Klinkhamer, Vincent M., Zürn, Gerhard, Lompe, Thomas, and Jochim, Selim. *Two Fermions in a Double Well: Exploring a Fundamental Building Block of the Hubbard Model. Phys. Rev. Lett.* 114 (8 Feb. 2015), p. 080402.
- [Mur15c] Murthy, P. A., Boettcher, I., Bayha, L., Holzmann, M., Kedar, D., Neidig, M., Ries, M. G., Wenz, A. N., Zürn, G., and Jochim, S. *Observation of the Berezinskii-Kosterlitz-Thouless Phase Transition in an Ultracold Fermi Gas. Phys. Rev. Lett.* 115 (1 June 2015), p. 010401.

Bibliography

- [Mur18a] Murthy, Puneet A., Defenu, Nicolò, Bayha, Luca, Holten, Marvin, Preiss, Philipp M., Enss, Tilman, and Jochim, Selim. *Quantum scale anomaly and spatial coherence in a 2D Fermi superfluid*. 2018.
- [Mur18b] Murthy, Puneet A., Neidig, Mathias, Klemt, Ralf, Bayha, Luca, Boettcher, Igor, Enss, Tilman, Holten, Marvin, Zürn, Gerhard, Preiss, Philipp M., and Jochim, Selim. *High-temperature pairing in a strongly interacting two-dimensional Fermi gas*. *Science* 359.6374 (2018), pp. 452–455.
- [Nag66] Nagaoka, Yosuke. *Ferromagnetism in a Narrow, Almost Half-Filled s Band*. *Phys. Rev.* 147 (1 July 1966), pp. 392–405.
- [Nay08] Nayak, Chetan, Simon, Steven H., Stern, Ady, Freedman, Michael, and Das Sarma, Sankar. *Non-Abelian anyons and topological quantum computation*. *Rev. Mod. Phys.* 80 (3 Sept. 2008), pp. 1083–1159.
- [Nei17] Neidig, Mathias. *Few-particle quantum magnetism with ultracold atoms*. PhD thesis. Heidelberg University, 2017.
- [Nel07] Nelson, Karl D., Li, Xiao, and Weiss, David S. *Imaging single atoms in a three-dimensional array*. *Nature Physics* 3.8 (2007), pp. 556–560.
- [Nog14] Nogrette, F., Labuhn, H., Ravets, S., Barredo, D., Béguin, L., Vernier, A., Lahaye, T., and Browaeys, A. *Single-Atom Trapping in Holographic 2D Arrays of Microtraps with Arbitrary Geometries*. *Phys. Rev. X* 4 (2 May 2014), p. 021034.
- [Omr15] Omran, Ahmed, Boll, Martin, Hilker, Timon A., Kleinlein, Katharina, Salomon, Guillaume, Bloch, Immanuel, and Gross, Christian. *Microscopic Observation of Pauli Blocking in Degenerate Fermionic Lattice Gases*. *Phys. Rev. Lett.* 115 (26 Dec. 2015), p. 263001.
- [Ore10] Oreg, Yuval, Refael, Gil, and Oppen, Felix von. *Helical Liquids and Majorana Bound States in Quantum Wires*. *Phys. Rev. Lett.* 105 (17 Oct. 2010), p. 177002.
- [Par08] Paredes, Belén and Bloch, Immanuel. *Minimum instances of topological matter in an optical plaquette*. *Phys. Rev. A* 77 (2 Feb. 2008), p. 023603.

- [Par15] Parsons, Maxwell F., Huber, Florian, Mazurenko, Anton, Chiu, Christie S., Setiawan, Widagdo, Wooley-Brown, Katherine, Blatt, Sebastian, and Greiner, Markus. *Site-Resolved Imaging of Fermionic ${}^6\text{Li}$ in an Optical Lattice*. *Phys. Rev. Lett.* 114 (21 May 2015), p. 213002.
- [Par16] Parsons, Maxwell F., Mazurenko, Anton, Chiu, Christie S., Ji, Geoffrey, Greif, Daniel, and Greiner, Markus. *Site-resolved measurement of the spin-correlation function in the Fermi-Hubbard model*. *Science* 353.6305 (2016), pp. 1253–1256.
- [Pas08] Pasienski, Matthew and DeMarco, Brian. *A high-accuracy algorithm for designing arbitrary holographic atom traps*. *Opt. Express* 16.3 (Feb. 2008), pp. 2176–2190.
- [Qi11] Qi, Xiao-Liang and Zhang, Shou-Cheng. *Topological insulators and superconductors*. *Rev. Mod. Phys.* 83 (4 Oct. 2011), pp. 1057–1110.
- [Raa87] Raab, E. L., Prentiss, M., Cable, Alex, Chu, Steven, and Pritchard, D. E. *Trapping of Neutral Sodium Atoms with Radiation Pressure*. *Phys. Rev. Lett.* 59 (23 Dec. 1987), pp. 2631–2634.
- [Rea00] Read, N. and Green, Dmitry. *Paired states of fermions in two dimensions with breaking of parity and time-reversal symmetries and the fractional quantum Hall effect*. *Phys. Rev. B* 61 (15 Apr. 2000), pp. 10267–10297.
- [Rie10] Ries, Martin. *A magneto-optical trap for the preparation of a three-component Fermi gas in an optical lattice*. Diploma thesis. Heidelberg University, 2010.
- [Rie15] Ries, M. G., Wenz, A. N., Zürn, G., Bayha, L., Boettcher, I., Kedar, D., Murthy, P. A., Neidig, M., Lompe, T., and Jochim, S. *Observation of Pair Condensation in the Quasi-2D BEC-BCS Crossover*. *Phys. Rev. Lett.* 114 (23 June 2015), p. 230401.
- [Rok12] Rokhinson, Leonid P., Liu, Xinyu, and Furdyna, Jacek K. *The fractional a.c. Josephson effect in a semiconductor-superconductor nanowire as a signature of Majorana particles*. *Nature Physics* 8 (Sept. 2012).
- [Sal91] Saleh, Bahaa E A and Teich, Malvin Carl. *Fundamentals of photonics; 2nd ed.* Wiley-Interscience Publication, 1991.

Bibliography

- [Sar15] Sarma, Sankar Das, Freedman, Michael, and Nayak, Chetan. *Majorana zero modes and topological quantum computation*. *Npj Quantum Information* 1 (Oct. 2015). Review Article.
- [Sat17] Sato, Masatoshi and Ando, Yoichi. *Topological superconductors: a review*. *Reports on Progress in Physics* 80.7 (2017), p. 076501.
- [Sau10] Sau, Jay D., Tewari, Sumanta, and Das Sarma, S. *Universal quantum computation in a semiconductor quantum wire network*. *Phys. Rev. A* 82 (5 Nov. 2010), p. 052322.
- [Sch82] Schechter, J. and Valle, J. W. F. *Neutrinoless double- β decay in $SU(2) \times U(1)$ theories*. *Phys. Rev. D* 25 (11 June 1982), pp. 2951–2954.
- [Ser11a] Serwane, F., Zürn, G., Lompe, T., Ottenstein, T. B., Wenz, A. N., and Jochim, S. *Deterministic Preparation of a Tunable Few-Fermion System*. *Science* 332.6027 (2011), pp. 336–338.
- [Ser11b] Serwane, Friedhelm. *Deterministic preparation of a tunable few-fermion system*. PhD thesis. Heidelberg University, 2011.
- [Sha49] Shannon, C. E. *Communication in the Presence of Noise*. *Proc. Institute of Radio Engineers* 37.1 (1949), pp. 10–21.
- [She10] Sherson, Jacob F., Weitenberg, Christof, Endres, Manuel, Cheneau, Marc, Bloch, Immanuel, and Kuhr, Stefan. *Single-atom-resolved fluorescence imaging of an atomic Mott insulator*. *Nature* 467.7311 (2010), pp. 68–72.
- [Ste10] Stecher, J von, Demler, E, Lukin, M D, and Rey, A M. *Probing interaction-induced ferromagnetism in optical superlattices*. *New Journal of Physics* 12.5 (2010), p. 055009.
- [Tak82] Takahashi, Minoru. *$I=\infty$ Hubbard Model on Finite Lattices*. *Journal of the Physical Society of Japan* 51.11 (Nov. 1982), pp. 3475–3487.
- [Tas98] Tasaki, Hal. *From Nagaoka’s Ferromagnetism to Flat-Band Ferromagnetism and Beyond*. *An Introduction to Ferromagnetism in the Hubbard Model*. *Progress of Theoretical Physics* 99.4 (1998), pp. 489–548.

- [Tho82] Thouless, D. J., Kohmoto, M., Nightingale, M. P., and Nijs, M. den. *Quantized Hall Conductance in a Two-Dimensional Periodic Potential*. *Phys. Rev. Lett.* 49 (6 Aug. 1982), pp. 405–408.
- [Tur17] Turtaev, Sergey, Leite, Ivo T., Mitchell, Kevin J., Padgett, Miles J., Phillips, David B., and Čižmár, Tomáš. *Comparison of nematic liquid-crystal and DMD based spatial light modulation in complex photonics*. *Opt. Express* 25.24 (Nov. 2017), pp. 29874–29884.
- [Wal14] Walraven, J. T. M. *Quantum Gases - Statistics and Interactions*. (2014).
- [Wen08] Wenz, Andre N. *Few-Body Physics in a Three-Component Fermi Gas*. Diploma thesis. Heidelberg University, 2008.
- [Wil87] Willett, R., Eisenstein, J. P., Störmer, H. L., Tsui, D. C., Gossard, A. C., and English, J. H. *Observation of an even-denominator quantum number in the fractional quantum Hall effect*. *Phys. Rev. Lett.* 59 (15 Oct. 1987), pp. 1776–1779.
- [Yam16] Yamamoto, Ryuta, Kobayashi, Jun, Kuno, Takuma, Kato, Kohei, and Takahashi, Yoshiro. *An ytterbium quantum gas microscope with narrow-line laser cooling*. *New Journal of Physics* 18.2 (2016), p. 023016.
- [Zha04] Zhang, J., Kempen, E. G. M. van, Bourdel, T., Khaykovich, L., Cubizolles, J., Chevy, F., Teichmann, M., Tarruell, L., Kokkelmans, S. J. J. M. F., and Salomon, C. *P-wave Feshbach resonances of ultracold ${}^6\text{Li}$* . *Phys. Rev. A* 70 (3 Sept. 2004), p. 030702.
- [Zha14] Zhang, Zichen, You, Zheng, and Chu, Daping. *Fundamentals of phase-only liquid crystal on silicon (LCOS) devices*. *Light: Science & Applications* 3 (Oct. 2014). Review.
- [Zür12] Zürn, Gerhard. *Few-fermion systems in one dimension*. PhD thesis. Heidelberg University, 2012.

Erklärung

Ich versichere, dass ich diese Arbeit selbstständig verfasst und keine anderen als die angegebenen Quellen und Hilfsmittel benutzt habe.

Heidelberg, den 21. September 2018

Acknowledgements

An dieser Stelle möchte ich meinen Dank all jene richten, die mich während meines Studiums unterstützt und motiviert haben und dadurch dazu beigetragen haben, dass diese Arbeit entstehen konnte.

Lieber Selim, ich bin froh, dass ich gerade in deiner Gruppe meine Masterarbeit schreiben konnte. Ich bin mir sicher, dass deine neugierige, vorurteilsfreie und offene Art allen Studenten in deiner Arbeitsgruppe zugute kommt! Ein großes Dankeschön geht an das gesamte Ultracold-Team für die gute Arbeitsatmosphäre und die große gegenseitige Hilfsbereitschaft.

Insbesondere geht mein Dank an das Team vom Neuen Experiment: Puneet, Luca, Marvin, Keerthan und Philipp. Ich habe enorm viel von euch gelernt. Danke für eure Geduld, immer all meine Fragen zu beantworten. Ins Besondere möchte ich an dieser Stelle meine Wertschätzung an Luca richten. Danke, dass du so viel Zeit in die Betreuung meiner Masterarbeit investiert hast und dass du mir von der Pike auf das Arbeiten Labor beigebracht hast.

Zuletzt möchte ich ein großes Dankeschön an meine Familie und Freunde richten, deren Unterstützung ich mir immer sicher sein kann.